

---

# **Stationary and slow-moving convection over Switzerland: A 14-year radar-based climatology**

---

**Master's Thesis**

Faculty of Sciences

University of Bern

presented by

MARTIN PIUS AREGGER

2021

Supervisor:

Prof. Dr. Olivia Romppainen-Martius

*Institute of Geography, Mobiliar Lab for Natural Risks and*

*Oeschger Centre for Climate Change Research*

*University of Bern*



## **Abstract**

Convective storms are often associated with high rainfall rates, and if a convective storm stays stationary or moves slowly, the area over which it occurs will experience high precipitation accumulations. High amounts of precipitation in a short period of time is an important ingredient for natural hazards such as flash floods, landslides and debris flows.

These Stationary Convective Storms (SCS) have been analyzed in a few studies, but never for Switzerland. Here Lagrangian thunderstorm track data combined with blended radar-rain gauge precipitation fields are used to compile a climatology of SCS for Switzerland for the period from 2005 to 2018. Three different definitions for stationarity based on cell location and size are introduced and compared using different thresholds. For the climatology, the definition of stationarity based on weighted storm cell centroids' location is used. The resulting climatology provides an overview of SCS regarding their spatio-temporal characteristics and their precipitation characteristics which are then compared to non-stationary convective systems. SCS frequency and precipitation properties depend on the prevailing weather types, on the season, and the geographic setting, and they exhibit a strong diurnal cycle. They occur most frequently in the northern and southern Prealps and are responsible for some of the highest precipitation accumulations caused by single cells. Depending on the region, SCS only make up 3.03-4.67% of all storms; however, locally they can produce up to 74% of the top 100 highest precipitation accumulations by convective storms. Hotspots can be found in the Jura mountains, eastern Grisons, and central Switzerland.

Furthermore, a high-resolution WRF model simulation was used to analyze the mechanics leading to the stationarity of convection in a case study of a storm which occurred over the Bernese Prealps. The model could not reproduce the stationary convection but produced mesoscale meteorological conditions that could be potentially conducive to stationarity following the mechanisms found in current literature.



# Contents

<b>1</b>	<b>Introduction</b>	<b>1</b>
<b>2</b>	<b>Literature Review</b>	<b>5</b>
2.1	Stationary Convective Storms . . . . .	5
2.2	Thunderstorm climatologies . . . . .	9
<b>3</b>	<b>Data</b>	<b>13</b>
3.1	Radar Data . . . . .	13
3.2	Thunderstorm Radar Tracking (TRT) . . . . .	14
3.3	Precipitation Data . . . . .	15
3.4	Weather Types . . . . .	16
3.5	ERA5 Data . . . . .	16
3.6	Weather Research and Forecasting (WRF) Data . . . . .	16
<b>4</b>	<b>Methods</b>	<b>17</b>
4.1	Stationarity . . . . .	17
4.2	Data Processing . . . . .	19
4.3	Statistical Methods . . . . .	21
4.3.1	Mann-Whitney-U Test . . . . .	23
4.3.2	Wheeler-Watson Test . . . . .	23

4.3.3	Fisher's Exact Test . . . . .	23
4.3.4	Anomaly . . . . .	24
4.4	Case Study . . . . .	24
4.4.1	Bumbach - 24.07.2014 . . . . .	24
4.4.2	Approach . . . . .	26
<b>5</b>	<b>Results</b>	<b>27</b>
5.1	Stationarity Definition Comparison . . . . .	27
5.1.1	Overlap Stationarity . . . . .	27
5.1.2	End-to-end Stationarity vs Path Stationarity . . . . .	28
5.1.3	Threshold Choice . . . . .	29
5.2	Climatology Results . . . . .	30
5.2.1	Annual Variability . . . . .	30
5.2.2	Weather Type and Circulation . . . . .	31
5.2.3	Monthly Distribution . . . . .	34
5.2.4	Diurnal Cycle . . . . .	35
5.2.5	Spatial Characteristics . . . . .	35
5.2.6	Precipitation Characteristics . . . . .	39
5.3	Case Study Results . . . . .	42
<b>6</b>	<b>Discussion</b>	<b>49</b>
6.1	Discussion Climatology . . . . .	49
6.2	Discussion Case Study . . . . .	54
<b>7</b>	<b>Conclusions and Outlook</b>	<b>57</b>

<b>Appendix</b>	<b>61</b>
<b>List of Figures</b>	<b>70</b>
<b>List of Tables</b>	<b>72</b>
<b>References</b>	<b>73</b>
<b>Acknowledgements</b>	<b>87</b>
<b>Declaration of Consent</b>	<b>88</b>





# 1 | Introduction

Precipitation is a function of the average rainfall rate multiplied by the duration of the rainfall event. Convective systems can cause high rainfall rates and if they stay stationary or move slowly, the area over which they occur will experience heavy precipitation (SODERHOLM et al. 2014). Convective precipitation occurs when moist air parcels are lifted vertically through the atmosphere due to buoyancy. While the parcels are lifted, they cool down to the point of saturation, leading to any excess moisture condensing and precipitating. The heat released in this process contributes further to the buoyancy of the air parcel (DOSWELL 2001).

A variety of triggers can initiate convective storms, and the precipitation they release can locally be of high intensity, which makes rainfall amounts challenging to forecast. While recent advancements in high-resolution numerical weather modelling have considerably improved the skill of forecasts regarding the timing and location of storms, there are still difficulties with predicting the precipitation amounts in complex topography (FLESCH and REUTER 2012, WAGNER et al. 2018). Convective precipitation may trigger natural hazards, such as flash floods, landslides, and debris flows (CANUTI et al. 1985, GUZZETTI et al. 2008). Those hazards frequently cause fatalities (BADOUX et al. 2016) and they are responsible for damages in Switzerland that averaged 141 million CHF annually between 1972 and 2017 (ANDRES and BADOUX 2019, HILKER et al. 2009). Due to these devastating consequences, the forecasting of flash floods, landslides, and debris flows is of substantial interest to the Swiss population and authorities.

There are efforts underway to provide early warning systems for flash floods, landslides, and debris flows. All these systems require an accurate forecast of (intense) precipitation (e.g. BAUM and GODT 2010, OSANAI et al. 2010, ROMANG et al. 2011, LIECHTI et al. 2013, PANZIERA et al. 2016). Current high-resolution convection models used for numerical weather prediction are generally able to represent the spatial structure and timing of the onset of convection; however, they are still struggling to forecast the intensity of precipitation (WAGNER et al. 2018). There are many potential causes for this, such

as sensitivity to uncertainties in the large-scale flow and the boundary layer structure (HANLEY et al. 2011) or model properties such as the effect of model terrain height and smoothing on the convective initiation (SCHNEIDER et al. 2018), or the time step size (BARRETT et al. 2019). Consequently, the early warning systems are still limited. To overcome these limitations, observation-based climatologies are needed for warnings, risk assessments in the insurance sector (BOTZEN et al. 2010), the verification of numerical weather prediction models (e.g. SPIRIDONOV et al. 2010, SCHWARTZ et al. 2018) and as training data for new approaches based on machine learning (FORESTI et al. 2019).

There are two different basic approaches for the creation of such climatologies: Eulerian and Lagrangian. The Eulerian approach analyses a measured field at fixed points over time. This approach has been used for many climatologies, focusing on the spatial and temporal distribution of extreme precipitation and hail. For example, LUKACH et al. (2017) produced a 10-year radar climatology of hail in Belgium. Similar work has been done by NISI et al. (2016) for Switzerland. Many examples more focused on the precipitation can be found for the US (e.g. CARBONE and TUTTLE 2008, CARBONE et al. 2002, LOMBARDO and COLLE 2010, SCHUMACHER and JOHNSON 2008) but also for other countries, e.g. Canada (BRIMELOW et al. 2004), China (HUANG et al. 2017), and the Netherlands (OVEREEM et al. 2009). Another example by WECKWERTH et al. (2011) looked explicitly at convective initiation. This type of climatology can provide information on a high temporal and spatial resolution. For example, BARTON et al. (2020) produced a 7-year precipitation assessment of Switzerland with 5 min temporal and 1  $km^2$  spatial resolution based on blended radar-rain-gauge data.

While the Eulerian approach is undoubtedly diverse, statistics concerning the track of a thunderstorm such as its length, duration, and speed require a different type of data which only a Lagrangian approach can provide. The Lagrangian approach is based on the identification of specific convective cells and the subsequent tracking of these cells. This is a complex task which requires data with high spatial and temporal resolution. The potential of such Lagrangian storm track data, however, is vast. Movement data can, for example, be used for machine learning-based nowcasting. FORESTI et al. (2019) used a 10-year archive of radar data to extract the motion of radar precipitation echoes. They then used this dataset to train an artificial neural network to nowcast the growth and decay of precipitation over the Swiss Alps.

In recent years, there have been efforts to create such Lagrangian storm track climatologies for many world regions. For example, in north-western Italy (DAVINI et al. 2012), Oklahoma in the United States (HOCKER and BASARA 2008) or Southeast Queensland in Australia (PETER et al. 2015). For Switzer-

land, there is a comprehensive 15-year climatology, with a particular focus on hailstorm tracks, by NISI et al. (2018). While their radar-based climatology was focused mainly on hail-producing convective storms, the cell track database they produced also offers a wealth of Lagrangian data which allows for the further study of the life cycles of different stormtypes. In this thesis, the focus is specifically on stationary or slow-moving convective storms. There is no clear definition of when a storm is considered stationary. Generally, for a storm to be recognized as stationary, it must stay over a region for a prolonged period of time; however, it can move slowly.

This specific type of convective storm, has only been analyzed in a few select studies. Early case studies by MADDOX et al. (1978) looked at two flash floods in the western US (Rapid City 1972, Big Thompson 1976). In both cases, they found that conditionally unstable and extremely moist air masses impinged perpendicularly onto mountainous terrain ("cross-barrier") forced by strong flow at low levels. This process led to convective storms, producing heavy precipitation, which moved slowly due to unusually weak upper-level winds. Similar results were found by more recent studies based on observational data and numerical modelling approaches (DUCROCQ et al. 2008, MIGLIETTA and ROTUNNO 2009, SODERHOLM et al. 2014). Though, these three studies also found other possible mechanisms which can cause this stationarity. What all the mechanisms have in common, is that stationary, long-lasting storms arise from the interaction of convective storms with orography.

Switzerland, with its complex orography, could potentially be well suited for stationary convective storms. However, there has not yet been any work done to investigate this type of storm's prevalence and mechanics. Thus, this master thesis aims to fill this knowledge gap by characterizing stationary storms over Switzerland. For this purpose, first, a climatology will be produced using cell track data for the convective season (April-September) of 2005-2018 to answer the following questions:

- (a) Where do stationary convective storms occur?
- (b) When do stationary convective storms occur?
- (c) How do the spatio-temporal characteristics of stationary storms differ from those of non-stationary storms?

In a second step, after characterizing stationary storms over Switzerland in this climatology, a case study will be performed to analyze the mechanics leading to these storms' stationarity. For this analysis, a high-resolution numerical weather prediction model will be used to reproduce a storm and get an

in-depth understanding of the local-scale processes leading to its stationarity. This approach has previously been used for example by TREFALT et al. (2018) to investigate the influence of mountain wind systems and cold-air outflows on the initiation and propagation of a severe hailstorm over the northern Swiss Prealps. Another example can be found in a Case Study by YANG et al. (2014) who investigated the influence of urban modification on a storm system's rainfall characteristics.

In this thesis, the Weather Research and Forecasting (WRF) model (POWERS et al. 2017) will be used to reproduce the storm in the case study with high spatial and temporal resolution. The study will help to answer the following two questions:

- (d) What are the mesoscale conditions under which stationary convective storms occur?
- (e) What are the mechanisms on the local scale that allow the storms to stay stationary?

Chapter 2 of this thesis provides an overview of the current state of research into stationary storms and the different theories on their formation. Following this, Chapter 3 provides an in-depth description of the data used to produce the climatology and the case study. Subsequently, Chapter 4 describes all the methods used in this master thesis. In Chapter 5, the results are presented and then discussed in Chapter 6. Finally, in Chapter 7, the conclusions are drawn.

## 2 | Literature Review

### 2.1 Stationary Convective Storms

For deep moist convection (DMC) to develop three necessary conditions must be present: First, there must be a conditionally unstable environmental lapse rate, which means that a rising air parcel could become buoyant if it becomes saturated at some point, depending on the surface temperature and humidity. In connection to this, the second requirement is sufficient moisture in lower levels. If these two conditions apply, a lifting mechanism may force an air parcel to its level of free convection (LFC) where it becomes more buoyant than the surrounding atmosphere and therefore initiates convection. This mechanism for lifting is consequently the third requirement for DMC to occur. DMC will continue as long as these three requirements are met (e.g. DOSWELL 2001).

A typical convective cell has a life cycle with three stages that can be seen schematically in Figure 1. The cumulus stage, where the convection initiates and the storm is characterized by strong updrafts, followed by the mature stage, which has both sustained updrafts and downdrafts, and is associated with heavy precipitation. Depending on the vertical wind shear, these downdrafts can either be located horizontally shifted from or coinciding with the updrafts. The drag of falling precipitation causes the downdrafts. They can further intensify due to melting, evaporation, and sublimation of precipitation in the falling air, which causes diabatic cooling. The cold downdrafts then reach the surface where they spread out horizontally in the form of a density current. This current can either cut off the supply of warm air, which is necessary for continued convection, or trigger new cells. Consequently, the storm enters its final stage, the dissipating stage, in which it only consists of downdrafts (e.g. LOHMANN et al. 2016).

The lifetime of such an isolated convective cell is approximately 40 minutes to one hour, depending on the depth of the convection, and the intensity of the updrafts (e.g. DOSWELL 2001). However, this thesis focuses on longer-lived storms. For longer-lived storms, the attention has to be on multicell and

supercell storms. These storm types have a key ingredient which leads to their longevity: vertical wind shear. The shear separates the updrafts and downdrafts of the storm horizontally. Consequently, the downdrafts cannot cut off the updrafts (e.g. LOHMANN et al. 2016).

In a multicell storm, the density current of one convective cell can cause the initiation of another one within the same storm system. This process allows the storm to continue for multiple hours. A supercell storm can occur if there is strong anticyclonically turning wind shear ( $20\text{ms}^{-1}$ ) in the lowest 6 km of the atmosphere. This storm type consists of only one convective cell with one large updraft and two downdrafts. A continuous source of hot and moist air allows the storm to sustain itself for a long time (e.g. LOHMANN et al. 2016).

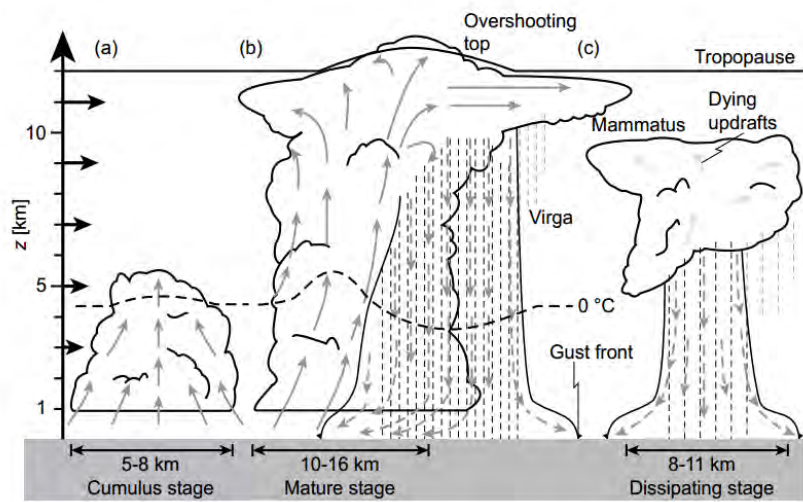


**Figure 1:** The three stages of a convective cell: (a) cumulus stage, (b) mature stage, and (c) dissipating stage. The grey arrows show the motion of air, the black arrows on the left axis the horizontal wind profile, and the dashed horizontal line the  $0^\circ\text{C}$  isotherm. (from LOHMANN et al. 2016)

As mentioned before, vertical wind shear is necessary for these long-lived storm types to occur. However, a sheared environment is not conducive to a storm staying stationary due to the winds required. For a storm to stay stationary and have a long lifetime, special conditions are required. Some possible mechanisms for this will now be presented in the rest of this chapter.

DUCROCQ et al. (2008) simulated three heavy precipitation events over southern France. In all three cases, a low-level jet (LLJ) of warm and moist air formed over the Mediterranean ocean and then impinged onto the Massif Central. In one case over the Cévennes region, orographic forcing by the Massif Central foothills was the primary mechanism that continually produced new convective cells. In another case over the Gard plain, a low-level cold pool generated by diabatic cooling through evaporation of precipitation caused blocking and forced the LLJ to ascend. This cold pool propagated downslope due to its high density. If the propagation speed downslope becomes balanced with the LLJ blowing

uphill, a stationary convective storm can form, as shown in Figure 2.

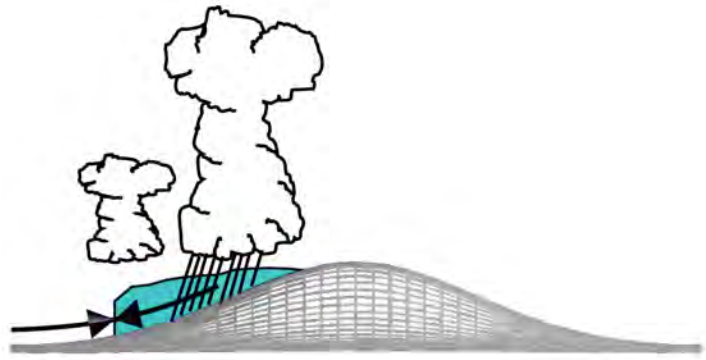


**Figure 2:** Schematic of a stationary cold pool on a mountain slope. The cold pool is shown in blue with the downslope arrow showing the winds it produces. The LLJ is shown by the arrow pointing upslope. The cold pool propagates downslope and is balanced by the LLJ blowing uphill.(adapted from KIRSHBAUM et al. 2018)

Similar results were found by MIGLIETTA and ROTUNNO (2009) when they performed idealised simulations of a conditionally unstable flow over a 2D ridge. They tested different ridge heights and widths, combined with varying wind speeds. For weak environmental wind speeds ( $= 2.5\text{ms}^{-1}$ ) they found a similar process as described in the Gard plain case study above (Figure 3a). If the environmental wind speed is of medium strength ( $= 10\text{ms}^{-1}$ ) they also found a stationary convective storm on the lee side of the mountain ridge. For this case, they discovered a "hydraulic jump" where convection downstream produces a stationary cold pool which triggers further convection. MIGLIETTA and ROTUNNO (2009) also found stationary convection when the environmental wind speed is high ( $= 20\text{ms}^{-1}$ ). In this case the air parcels do not have time to cool sufficiently to form a cold pool before reaching the mountain ridge and subsequently descending on the lee side. Consequently, a stationary convective system such as the one observed by DUCROCQ et al. (2008) the Cévennes case can form.

So far, only examples of stationary convection caused by cross-barrier wind flows have been discussed, but there is also the option for along-barrier flows to cause it. SODERHOLM et al. (2014) looked at short track long duration events (STLD) over the Black Hills in western South Dakota in the US. They found that weak winds aloft coupled with low-level winds along the mountain ridge provide an environment for stationary thunderstorms. The flow along the barrier is drawn upslope by heating on the crest, creating a convergence line along the ridgeline. Convective cells form downwind of the crest where they create cold pools that do not interfere with the upwind convergence line as can be seen in Figure 4.

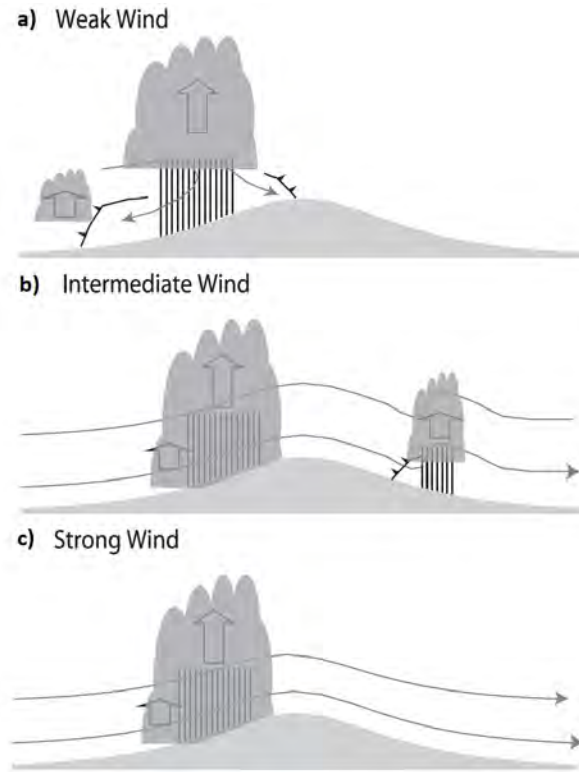


**Figure 3:** The effect of different wind speeds on convection caused by cross-barrier flow. For weak wind (a), rainfall and evaporation generate a cold pool on the slope which travels downslope and which can trigger further convection in the same location if the cold air outflow is balanced by the LLJ inflow. For intermediate wind (b), there is convection triggered on the mountain's lee side, and a hydraulic jump which can cause stationary convection. For intense winds (c), the evaporative cooling is too small for a cold pool to form on the ridge's windward side. The strong winds transport the cold air to the lee side. (adapted from MIGLIETTA and ROTUNNO 2009)

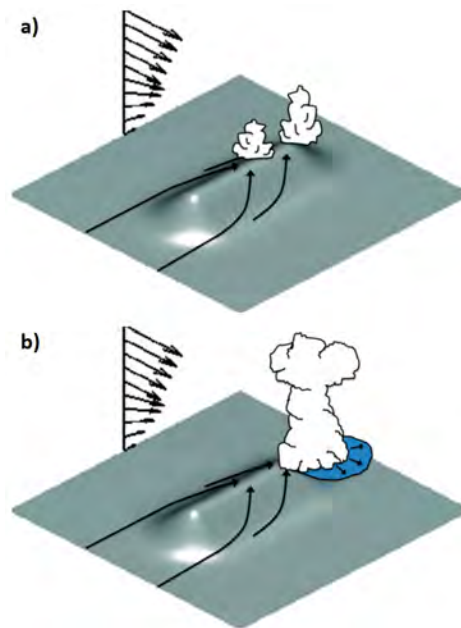


**Figure 4:** The effect of along-barrier low-level flow. The flow is drawn upslope as it travels along the ridge, creating a convergence line on the crest (a). The convective cells forming then produce a cold pool on the ridge's downwind side, which does not interfere with the up-slope convergence line (b). This process then allows for convective cells to continually be generated in the same location. (adapted from SODERHOLM et al. 2014)



Overall there seem to be four mechanisms which lead to stationary convection that can be found in literature:

- Strong cross-barrier flow causes convection at the mountain slope with no cold pool developing on the upwind mountain slope due to limited time for diabatic cooling (MIGLIETTA and ROTUNNO 2009).
- Intermediate cross-barrier flow allows for a “hydraulic jump” on the mountain’s lee side (MIGLIETTA and ROTUNNO 2009).
- Cross-barrier flow causing convection on the upwind slope, which produces a cold pool that is kept stationary by a LLJ. This allows for stationary convection at a distance from the mountain ridge (DUCROCQ et al. 2008, MIGLIETTA and ROTUNNO 2009).
- Along-barrier wind flow which causes convection on the ridge and separates cold pools such that they do not interfere with the upwind convergence line (SODERHOLM et al. 2014).

## 2.2 Thunderstorm climatologies

Early studies about the statistical characteristics of convective storms were based on weather station reports. For example, CHANGERY (1981) and CHANGNON (1988) both used data from weather stations of the National Weather Service (NWS) in the US to analyse spatio-temporal characteristics of thunderstorms. The quality of the data limits these early works. The NWS stations; for example, recorded thunderstorms only when the weather observer heard thunder.

More recent studies use data from lightning detection networks, satellite observations, and especially precipitation radars. These modern technologies provide much improved spatio-temporal resolution but also have their drawbacks; Lightning detection networks measure thunderstorms’ electrical activity, which can be used to determine their intensity, but they naturally miss convective storms when no lightning occurs (e.g. MÄKELÄ et al. 2010, POELMAN 2014, WAPLER 2013). Satellites allow for observations on a large scale, especially in areas where no ground stations are available. Infrared brightness temperatures are then used as a proxy to infer rainfall events. However, these inferences are subject to substantial errors (TUTTLE et al. 2008). Ground-based radars offer a high spatio-temporal resolution covering large areas, which allows for insights into the small-scale spatial structure of convective systems, which is important because of their high spatio-temporal variability. Due to these properties, radars have become an invaluable tool for many weather services to nowcast convective precipitation

(e.g. BECH and CHAU 2012, FORESTI et al. 2015). However, only in recent decades have "long-term" radar archives, which allow for the climatological study of convective storms, become available for many world regions.

As mentioned in the introduction, there is a need for Lagrangian storm track data to investigate stationary thunderstorms. The simplest way to produce such a Lagrangian dataset is manual tracking (e.g. HOUZE et al. 1993, NIYOGI et al. 2010). However, this approach is flawed because of the subjectivity, and it is very labor intensive and consequently not suitable for the production of long term climatologies.

Many meteorological services have therefore developed computational methodologies for automatic identifying and tracking of storm cells. For example, TITAN (DIXON and WIENER 1993) and SCIT (JOHNSON et al. 1998) in the US, SWIRLS (LI and LAI 2004) in Hong Kong, and TRACE3d in Germany (HANDWERKER 2002). For Switzerland, the Thunderstorms Radar Tracking (TRT) tool has been developed by MeteoSwiss and is now used operationally (HERING et al. 2004). These tools have been used to describe the characteristics of convective storms all over the globe. For example GOUDENHOOFDT and DELOBBE (2013) produced a 10-year climatology for Belgium, where they looked at storm frequency, spatial distribution, initiation location, storm track length, storm duration, and cell speed. Similar climatologies have been produced for north-western Italy (6-year; DAVINI et al. 2012), southern Quebec CA (9-year; BELLON and ZAWADZKI 2003), New Mexico US (9-year; SAXEN et al. 2008), North Dakota US (5-year; MOHEE and MILLER 2010), Oklahoma US (10-year; HOCKER and BASARA 2008), Prut River Basin RO (15-year; BURCEA et al. 2019), South Florida US (2-year; LÓPEZ et al. 1984), and Southeast Queensland AU (8-year; PETER et al. 2015). For Switzerland, there is the aforementioned 15-year climatology, with a particular focus on hail, by NISI et al. (2018).

Other than these multiyear climatologies there have also been several studies which looked at the characteristics of storms only in a single season, e.g. Sydney AU (POTTS et al. 2000), Darwin AU (MAY and BALLINGER 2007), Western Ghats IN (UTSAV et al. 2017), Cuba (NOVO et al. 2014), and Germany (WEUSTHOFF and HAUF 2008).

While the studies mentioned above describe the thunderstorms' movement, almost none pay specific attention to slow-moving or stationary ones. The one exception is the previously study by SODERHOLM et al. (2014). They looked at three different storm types; short track short duration (STSD), short track long duration (STLD), and long track long duration (*LTL*D) convective storms over a span of 10 years over the Black Hills in South Dakota. An STLD event was defined as a storm which moved less than 25

km in at least 90 minutes. For an *LTL*D Storm, a cell had to survive for at least 120 minutes and travel more than 100 km. The duration minimum of 90 minutes was chosen because it is sufficiently long for heavy precipitation to accumulate. The 25-km distance corresponds to the cross-barrier length scale of the Black Hills. They found that *STLD* and *LTL*D events each only make up about 20% of all storms. However, they only looked at 130 storms in total. Additionally, they looked at thermodynamic profiles to assess whether the thermodynamic conditions between the three groups differed. While there were many subtle differences observed only one was statistically significant at the 95% confidence level: The LCL height for *STSD* soundings was significantly higher at 2601 m compared to *STLD* (2118 m) and *LTL*D (2010 m) respectively. Furthermore, North American Mesoscale Forecast System (NAM) model analyses were used to compare the three groups' wind profiles. The low-level wind profiles of the *STLD* events predominantly aligned with the Black Mountains' ridge axis. This led the authors to hypothesize that low-level winds aligned with the long terrain axis are favorable for stationary convection, which was described in the previous chapter (SODERHOLM et al. 2014).



## 3 | Data

For this thesis, several different data types from different sources are used. For the climatology Lagrangian thunderstorm track data generated by the TRT algorithm (Chapter 3.2) from radar data (Chapter 3.1) is combined with precipitation data (Chapter 3.3) and information about the mesoscale weather conditions in the form of weather types (Chapter 3.4) and reanalysis data (Chapter 3.5). For the case study, a numerical weather simulation is performed (Chapter 3.6).

### 3.1 Radar Data

In this thesis, Lagrangian storm track data is required to analyse the movement of the storms. Radar is an observation system with the unique capability to observe convective storms at a high temporal and spatial resolution over a large domain, which is critical for the subsequent tracking of individual storms. The Lagrangian storm track data used in this thesis is based on observations by the MeteoSwiss radar network. Up to 2011, the network consisted of three C-band Doppler radars (JOSS et al. 1998), which were then replaced by dual polarisation radars (GERMANN et al. 2015) between 2011 and 2012. In 2014 and 2016, two additional radar sites were added (Figure 5) Detailed information on the radars can be found in JOSS et al. (1998) and GERMANN et al. (2006, 2016, 2017). The dataset used here covers the convective season (April-September) of 2005-2018 at a  $1 \text{ km}^2$  spatial and 5 min temporal resolution. It contains approximately 1.15 million individual storm tracks over Switzerland and surrounding areas.

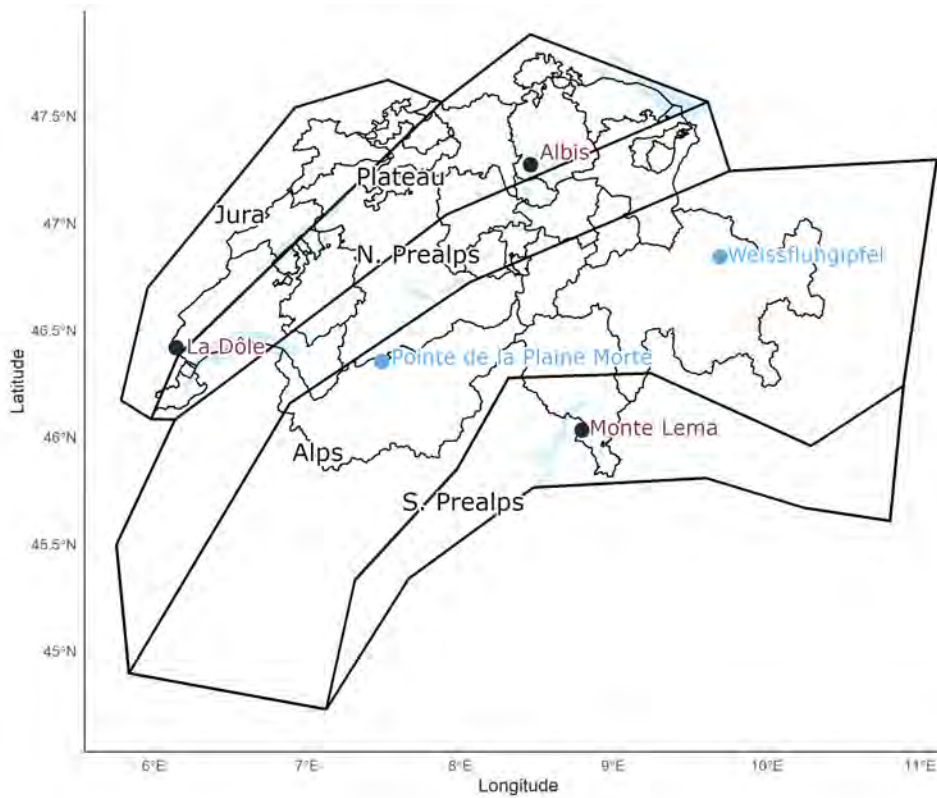


**Figure 5:** Study region and the five subregions (black, more details in chapter 4.2). The coloured dots mark the locations of the different radars of the MeteoSwiss radar network. Albis, La Dôle, and Monte Lema (red) were the original stations with the stations on the Plaine Morte and the Weissfluhgipfel being added later (blue).

## 3.2 Thunderstorm Radar Tracking (TRT)

For thunderstorm tracking, MeteoSwiss has developed TRT, a multi-radar tracking algorithm. It identifies and tracks thunderstorms, classifies their severity, and extrapolates their position for the next 60 minutes. TRT is based on an adaptive reflectivity thresholding scheme using radar images. This varying threshold (36-48 dBZ) is important because it allows the simultaneous tracking of cells at different stages of their life cycle. A fixed threshold would have the downside of clustering large areas of convection into a single object at a low threshold or if a high threshold is chosen it would only detect mature cells (HERING et al. 2004). Thanks to this, the algorithm is able to track individual cells instead of storm systems. The tracking of the cells is based on the geographical overlapping of cells in successive timesteps while considering their displacement velocity. For more details on the TRT, algorithm refer to MOREL et al. (2000, 2002), MOREL and SENESI (2002), HERING et al. (2004), HERING et al. (2008), and ROTACH et al. (2009). The TRT data used here was generated by applying the latest operational version of TRT on an archive of radar scans. Reprocessing all the data with the same algorithms increases the homogeneity of the final TRT dataset (NISI et al. 2018).

### 3.3 Precipitation Data

To analyse the precipitation produced by the convective storms, combined radar - rain gauge measurements by MeteoSwiss are used. The two measurement devices are combined in order to improve the accuracy of rainfall maps by using their complementing properties. As mentioned above, radars provide large scale coverage at a high temporal and spatial resolution. However, their rainfall intensity measurements are flawed due to variability in the relationship between reflectivity and rainfall intensity. On the other hand, rain gauges provide accurate measurements, but their coverage is limited to a sparse network. At MeteoSwiss, the two systems are combined using a geostatistical merging scheme named CombiPrecip (CPC) (SIDERIS et al. 2014).

CPC is aggregated on an hourly basis. It could technically work on shorter time scales; however, the hourly aggregation has advantages regarding the stability of the blending process and reduces discrepancies between radar and rain gauges due to various error sources (VILLARINI et al. 2008, SIDERIS et al. 2014). To be used with the TRT data, the CPC data therefore must first be disaggregated into shorter 5 minute rainfall maps. For this, the disaggregation method by BARTON et al. (2019) was used in this thesis.

The TRT data and the CPC data are combined to an initial dataset containing approximately 1.15 million cells between 2005 and 2018. For each cell, the variables in Table 1 are available at 1  $km^2$  spatial and 5 minute temporal resolution (others too, but they are not used here).

**Table 1:** Variables available in the thunderstorm dataset for each storm cell.

Parameter	Explanation	Units
Storm-ID	A unique ID for each storm	-
First Detection	Date and time of storm initiation	-
Last Detection	Date and time of storm decay	-
Centroid Coordinates	Coordinates of storm centroid for each 5 min step for the entire storm life cycle	[° N and E]
Contour Coordinates	Coordinates of the storm contours for each 5 min step for the entire storm life cycle	[° N and E]
Storm Area	Area of the storm	[ $km^2$ ]
Storm Velocity	Velocity of the storm in U and V components	[km/h]
Precipitation Data	Amount of Precipitation per pixel of the Storm	[mm]

### 3.4 Weather Types

To get a first overview of the synoptic weather conditions present with different convective storm types, a Weather Type Classification by MeteoSwiss is used. weather type classifications identify recurrent weather patterns for specific regions. Here, the GrossWetterType (GWT) classification method based on geopotential height with ten classes is used. The GWT is based on the wind speed and direction at 500 hPa height in central Europe and is calculated from European Center for Medium-Range Weather Forecasts (ECMWF) ERA-interim reanalysis data (01/09/2002-31/12/2010) and later from operational ECMWF Integrated Forecast System (IFS) data (from 01/01/2011) (WEUSTHOFF 2011). The GWT classifies the weather into eight wind directions, low pressure, and high-pressure weather situations.

### 3.5 ERA5 Data

For the analysis of the mid-tropospheric wind fields, ECMWF ERA5 reanalysis data at 750 hPa are used. ERA5 is a dataset produced by using the 4D-Var data assimilation integrated into the IFS. The dataset has a spatial resolution of  $31 \text{ km}^2$  and a six-hourly temporal resolution. (HERSBACH et al. 2020)

### 3.6 Weather Research and Forecasting (WRF) Data

For the case study in this master thesis, a simulation of the WRF model is used. WRF is a convection-permitting numerical weather prediction model developed by the National Center for Atmospheric Research (NCAR) and is one of the most widely used models (Powers et al. 2017). In this thesis, version 4.0.1 of the Advanced Research WRF (ARW) is used. The ARW is a particular configuration of the WRF which can be applied to "real-time NWP, weather events and atmospheric-process studies, data assimilation development, parameterised-physics development, regional climate simulation, air quality modelling, atmosphere-ocean coupling, and idealised- atmosphere studies." (SKAMAROCK et al. 2019).

Here the predicted particle properties (P3) scheme (MILBRANDT and MORRISON 2016) is used for the parametrisation of the cloud microphysics. The model is forced with external data from the ECMWF operational analysis and is run in two nested domains, of which the inner domain ( $3.70^\circ\text{E}$ - $13.81^\circ\text{E}$ ,  $43.85^\circ\text{N}$ - $49.49^\circ\text{N}$ ) is used for this thesis. The WRF model output consists of 191 different variables in a 4D grid (x,y,z,t). The model is run with a spatial resolution of  $1.5 \text{ km}^2$  on 50 vertical model levels and output at a 5-minute temporal resolution.



## 4 | Methods

The first part of this master thesis focuses on producing a climatology of Stationary Convective Storms (SCS) over Switzerland. For this, stationarity must first be defined (Chapter 4.1). After that, the Input data is prepared (Chapter 4.2), and then the final data is analysed (Chapter 4.3). In Chapter 4.4 the methods for the second part of the thesis, the case study, are described.

### 4.1 Stationarity

The first step towards the analysis of SCS is to find a definition of stationarity which can be operationalised on the available data for the climatology. There are several different ways that stationarity can be defined and initially, three of them are tested and compared in this thesis. The three tested methods are described here.

Definitions one and two are inspired by SODERHOLM et al. (2014), who defined STLD storm cells as cells that move less than 25 km over at least 90 minutes. Here we define the gravitational centre of a storm cell as its current position. Both definition one and two are based on a maximum distance that the cell can move in a specific time period.

#### 1. *End-to-end Stationarity (ETES)*

Here the distance a cell travelled is calculated by comparing the cell coordinates at two different times that are at least a certain number of minutes apart. This definition is applied in two different ways (Figure 6a):

- *End-to-End Stationarity Lifetime (ETESl)*

The whole lifetime of the cell is considered. The distance  $d_{lifetime}$  is calculated between the location of the first ( $P_{i_0}$ ) and the last observation ( $P_{i_{end}}$ ) of the cell and must be less than a given threshold for the cell to be considered stationary (Eq. 1).

$$d_{lifetime} = distance(P_{t_0}, P_{t_{end}}) \quad (1)$$

- *End-to-end Stationarity partial (ETESp)*

Only a time interval is considered and not the complete lifetime of the cell. The cell must not move more than a certain distance in a given time interval. However, it can move more outside of this interval. The distance  $d_{partial}$  is calculated following Equation 2 with  $P_{t_x}$  denoting the position of an arbitrary observation of the cell and  $P_{t_{x+T}}$  as the position of the same cell  $T$  timesteps later. For  $T$ , all values between the minimum threshold and the total lifetime of the cell are tested (Eq. 2).

$$d_{partial} = distance(P_{t_x}, P_{t_{x+T}}) \quad (2)$$

## 2. Path Stationarity (PS)

Here the distance a cell travelled is calculated by summing up the distances between each observational timestep over a given time interval. Again, this definition is applied in two different ways (Figure 6b):

- *Path Stationarity lifetime (PSl)*

The whole lifetime of the cell is considered. The distance  $d_{lifetime}$  is calculated for all cell positions between the first and the last observation of the cell (Eq. 3).

$$d_{lifetime} = distance(P_{t_0}, P_{t_1}) + distance(P_{t_1}, P_{t_2}) + \dots + distance(P_{t_{end-1}}, P_{t_{end}}) \quad (3)$$

- *Path Stationarity partial (PSp)*

Only a set time interval is considered. The cell must not move more than a certain distance in a given time interval. However, it can move more outside of this interval. The distance  $d_{partial}$  is calculated following Eq. 4.

$$d_{lifetime} = distance(P_{t_x}, P_{t_{x+1}}) + distance(P_{t_{x+1}}, P_{t_{x+2}}) + \dots + distance(P_{t_{x+T-1}}, P_{t_{x+T}}) \quad (4)$$

## 3. Overlap Stationarity (OS)

Here the area a storm cell covers and how it changes over time is analysed. Stationarity is defined

as a minimum overlap percentage ( $O$ ) of that area between different observation times of the cell (Figure 6c). The overlap percentage is calculated following Equation 5 with  $A_x$  denoting the area of a cell at timestep  $x$  (Eq. 5).

$$O = \frac{A_x \cap A_{x+T}}{A_x} \quad (5)$$

These three definitions are tested with different thresholds for the time/distance or time/overlap.

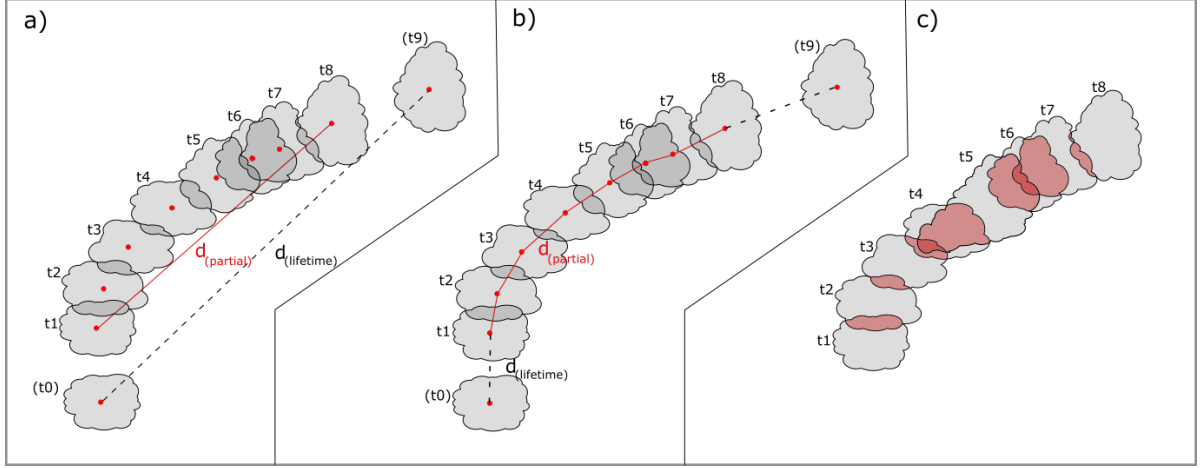


**Figure 6:** Schematic of the different stationarity definitions. The grey clouds mark the convective storm at different timesteps of its lifetime. The red dots mark the gravitational centre of the storm at each timestep. a) shows the ETES definition with the red line showing ETESp and the black dashed line showing the ETESl distance. The same in b) for PSI and PSp. C) shows the overlap definition with the overlaps marked in red.

Several different distance limits are tested for the PS and the ETES. Additionally, several different time limits are investigated. All definitions are tested for the time limits of 30, 60, 90, and 120 min. For the PS and ETES definitions, the distance limits from 5km to 45km are investigated at 5km intervals. For the OS definition, the overlaps from 10%, 20%, ..., 90% are tested at the same time limits as the previous definitions.

## 4.2 Data Processing

As a first step to producing the climatology, the initial dataset's size is reduced by removing all cells with a lifetime of fewer than 15 minutes. The resulting dataset contains around 470'000 cells which are of interest for the climatology of SCS. Of those cells, 218'650 lie within the study area (Figure 5). The study area is subdivided into five sub-regions which are roughly defined by their geographic and orographic properties. The five regions are the Jura Mountains, the Central Plateau, the northern and southern Prealps, and the Alps. The Jura Mountains are a sub-alpine mountain range on the north-western border of Switzerland separated from the Alps by the Central Plateau. The Plateau is a

relatively flat, densely populated area which spans from Lake Geneva up to Lake Constance and is bordered by the Jura in the north-west and the Prealps in the south. Here the hilly areas north and south of the Alps are considered separate areas from the central Alps due to their proximity to the flatter Plateau and Po-Valley, and their lower elevations. The fifth subregion are the Alps which are characterized by multiple mountain ranges and valleys. The borders between Prealps and Alps are not well-defined regions, so the lines drawn here are somewhat arbitrary.

In the next step, the different stationarity definitions are applied to each cell. For the ETES and PS stationarity definitions, distances need to be calculated. The dataset provides the storm cell weighted centroid coordinates with latitude/longitude values on the wgs84 (NGA 2014) coordinate system at each timestep. The distance method of the geopy python package (v. 2.0.0) (ESMUKOV 2020) is used to calculate distances. It calculates the geodesic distance using the method given by KARNEY (2013).

As a third step, the ERA5 wind fields and the GWT information is added to complete the dataset. The ERA5 wind fields have a different temporal and spatial resolution than the TRT data. To combine them, each storm cell's mean location is calculated and then matched to the closest pixel in ERA5 at the timestep closest to the initiation time of the cell. The GWT Information is daily and is simply added by date.

Finally, the precipitation information is processed to give information about the precipitation accumulation. All the calculated variables in the final dataset are shown in Table 2.

The final dataset is then analysed on a per-cell basis regarding the differences between the *SCS* and other cell storm types. To do this, the dataset is split into three different cell types:

- *SCS* – the stationary cells identified with the chosen stationarity definition
- *LTL**D* – (Long-Track-Long-Duration cells) – Inspired by SODERHOLM et al. (2014) the *SCS* are compared to cells which move far during their lifetime. Here, cells which moved at least 100 km in a lifetime of at least 90 minutes were defined as *LTL**D* cells.
- *OTHER* – All other cells

Together, these three classes contain 100% off the storms in the dataset.

**Table 2:** Variables which were added to the initial dataset either by calculation from existing variables (Table 1) or by combining the different datasets.

Parameter	Calculation	Units
Duration	Difference between the time of first detection and time of the last detection	[Minutes]
Distance Travelled	Depending on Stationarity definition either Formula 1, 2, 3 or 4 using the centroid coordinates	[Km]
Overlap	Formula 5	[%]
Mean Precipitation Rate	Precipitation Rate averaged over all timesteps and all pixels the storm impacted.	[mm/h]
Max Precipitation Rate	Single highest precipitation rate measured on a single 5-minute timestep at any of the pixels the storm impacted.	[mm/h]
Mean Precipitation Accumulation	Mean of all accumulated precipitation over all pixels a storm impacted over its lifetime	[mm]
Max Precipitation Accumulation	Maximum precipitation accumulation caused by the storm on a single Pixel.	[mm]
Weather Type	Classification added by Date	-
750 hPa Wind Speed	$\sqrt{U^2 + V^2}$	[m/s]
750 hPa Wind direction	Calculated from the U and V wind velocities provided by ERA5 using the 2-argument arctangent implementation of NumPy v1.19 (HARRIS et al. 2020)	[°]

### 4.3 Statistical Methods

In the result section, it is tested whether there are significant differences between the three different cell types defined above (*SCS*, *LTL*, *OTHER*) for each of the variables. Table 3 shows which test statistic is used for each variable. The test statistics are explained in Chapters 4.3.1 – 4.3.3.

**Table 3:** This table shows which test statistic was applied for each of the results of the climatology.

Parameter	Explanation
Annual Distribution	Mann-Whitney-U Test
Monthly Distribution	Wheeler-Watson Test
Daily Distribution	Wheeler-Watson Test
Weather Type	Fisher's Exact Test
Wind Direction	Wheeler-Watson Test
Wind Speed	Mann-Whitney-U Test
Max/Mean Precipitation rate	Mann-Whitney-U Test
Max/Mean Precipitation accumulation	Mann-Whitney-U Test

In this thesis, the sample sizes are relatively large, with approximately 220'000 cell tracks split into three different types. With the type of statistical techniques used here, two-sided hypothesis tests, this can lead to the well-known P-Value problem. In inferential statistics, the P-Value goes to zero if the

sample size goes to infinity, which means that if the sample size is larger than necessary for a test, its power increases. It will detect even minuscule effects as statistically significant even though they might be potentially meaningless (CALLEGARO et al. 2019).

The reason for this is a shrinking of the standard error as sample size increases. The standard error is typically used for measuring the P-Value, which is the distance between the sample data and the null-hypothesis using an estimated parameter of interest (LIN et al. 2013).

For increased transparency of the results, LIN et al. (2013)) suggest computing P-Values on subsets of the samples at different sizes, which is the approach that is used here. These multiple P-Values can then be plotted in a Monte-Carlo P-Value/sample size Chart (MPS-chart) (Figure 7). For each sample size, 100 random subsamples are drawn, which then are statistically compared. This process results in a range of P-Values, of which the median value is shown in the plot.

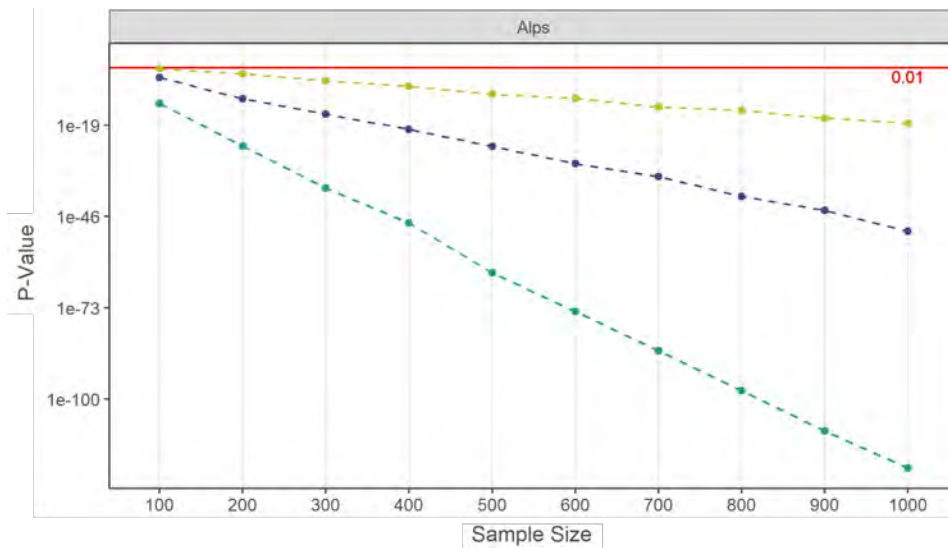


**Figure 7:** Example of an MPS-chart. Each of the lines shows the P-Values of one of the three comparisons; *SCS/OTHER* (green), *SCS/LTLD* (cyan), and *LTLD/OTHER* (dark blue) in relation to the sample size on a logarithmic scale. The shown P-Value is the median value of the 100 subsamples taken. The red line denotes the 0.01 significance level.

In the result section (Chapter 5.2) in the text the statistical significance is always given for the sample size 100 in the following form: (*SCS/OTHER* 85 %, *SCS/LTLD* 29%, *LTLD/OTHER* 20 %). The x/x signifies the two storm types which were compared. The percentage shown is the percentage of tests of sample size 100, which was significant at a 99% level. For each test, the complete MPS-chart is available in Appendix 1.

The one exception is the significance testing for the weather type classification. Here Fisher's Exact Test is used which can not be computed for sample sizes above 100 due to computational resource limitations. Therefore, the result for sample size 100 is shown, and there is no MPS-chart available.

### 4.3.1 Mann-Whitney-U Test

The Mann-Whitney-U test is a non-parametric test for independent samples that tests whether the samples' central tendencies differ. It is based on a ranking of the ordinal data. The test compares the sums of ranks of the different groups to calculate the test statistic  $U$  (Eq. 6):

$$U = n_1 n_2 + \frac{n_1(n_1 + 1)}{2} - R_1 \quad (6)$$

Where  $n_1$  and  $n_2$  are the sizes of the samples with the larger and the smaller sums of ranks, and  $R_1$  is the larger of the sums of ranks.  $U$  can then be standardised and compared to the standard normal distribution for significance testing. (MANN and WHITNEY 1947).

### 4.3.2 Wheeler-Watson Test

The Wheeler-Watson Test is a non-parametric test that compares two samples of cyclical data. It tests whether the samples come from the same population. The values of the samples are ordered and then replaced by coded values in degrees. First the  $R^2$  value is calculated (Eq. 7):

$$R^2 = \left( \sum_{j=1}^{n_1} \sin(\theta_j) \right)^2 + \left( \sum_{j=1}^{n_1} \cos(\theta_j) \right)^2 \quad (7)$$

Where  $n_1$  is the size of the first sample and  $\theta_1, \theta_2, \dots, \theta_{n_1}$  are the coded values for the first sample. The test statistic  $T$  can then be calculated with (Eq. 8):

$$T = \frac{2(n_1 + n_2 - 1)R^2}{n_1 n_2} \quad (8)$$

$T$  can then be compared to a chi-squared distribution for significance testing (WHEELER and WATSON 1964).

### 4.3.3 Fisher's Exact Test

Fisher's Exact Test is an exact test which examines the association between categorical samples in a contingency table. The test assumes a null hypothesis that states that both categorical samples have the same distribution. It can then be used to calculate the significance of the deviation from this null hypothesis, which is the P-Value (FISHER 1922).

#### 4.3.4 Anomaly

For the discussion of the annual variability of the different storm cell types, standardised anomalies  $N$  are calculated (WILKS 2006) (Eq. 9):

$$N = \frac{p_i - \mu}{\sigma} \quad (9)$$

Where  $p_i$  is the storm frequency of the year  $i$ ,  $\mu$  is the mean off all years, and  $\sigma$  is the standard deviation.

### 4.4 Case Study

The idea of the case study is that high-resolution WRF data is used to analyse the atmospheric conditions and mechanisms which lead to stationary convection over Switzerland in detail. Due to the time limitations of this thesis, only one case study is conducted. Chapter 4.4.1 introduces the chosen storm, and the following chapter explains the approach used to analyse it.

#### 4.4.1 Bumbach - 24.07.2014

For the case study, an event that happened on the 24.07.2014 in the region of Bumbach in the upper Emme Valley was selected. This event was selected because it is one of few, which was classified as a SCS by the definition used in the climatology for which there are also ground reports about its impacts (STURMARCHIV 2021).

In this event, a convective storm which initiated around 7.45 CEST stayed stationary for approximately 90 Minutes and led to locally more than 70 mm of accumulated precipitation to the north-west of Bumbach. This high precipitation accumulation combined with the topography and saturated soils due to previous storms led to floods in the region which damaged approximately 60 of the 90 local farms (NYDEGGER 2015, STURMARCHIV 2021). The nearby discharge measuring station "Emme – Eggiwil, Heidbüel" measured a peak flow of  $338 \text{ m}^3 \text{ s}^{-1}$  which corresponded to a return period of >150 years and was the highest ever measured flow at this station (BUNDESAMT FÜR UMWELT 2015).

The study area is shown in Figure 8. The Bumbach region is marked with red. It is in the valley of the Emme river with two mountain ridges, the Schratteflue and Hohgant on its southeastern border. For the SCS, the influence of these two ridges is of particular interest.



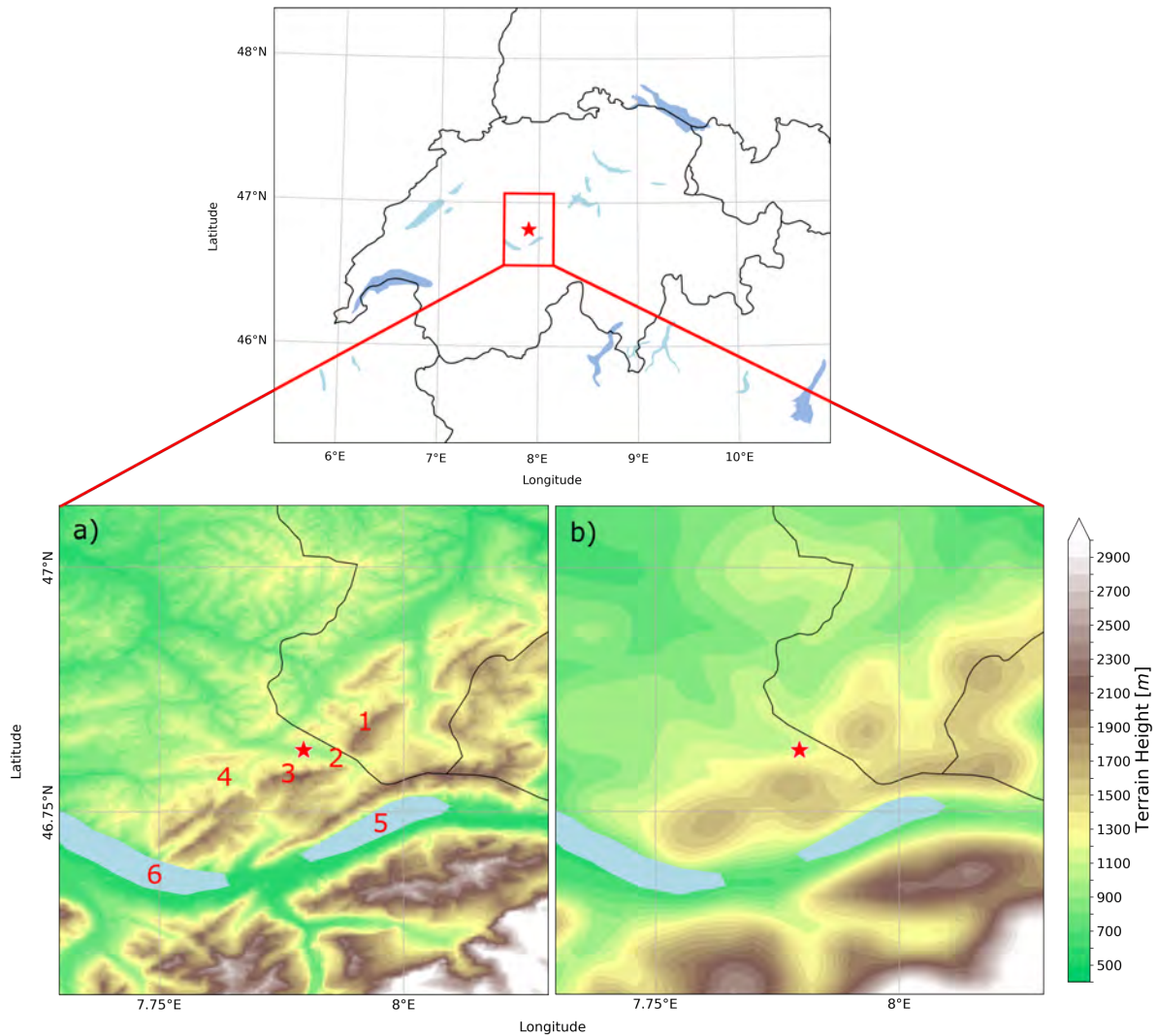


**Figure 8:** This figure shows the location of Bumbach (red star) in Switzerland (top) and then additionally the topography of the surrounding areas zoomed in to the red rectangle. The two topography plots on the bottom show the measured terrain heights (a) and the WRF model Terrain Heights (b). Some important topographical features are marked in the bottom left plot with red numbers: 1: Schratteflue mountain ridge, 2: Emme Valley, 3: Hohgant mountain ridge, 4: Zulg Valley, 5: Lake Brienz, 6: Lake Thun. All the horizontal maps in the case study result section (Chapter 5.3) have the same extent as the terrain maps.

#### 4.4.2 Approach

To analyze the *SCS*, in a first step, the factors leading to the convection are investigated following the ingredients-based method of DOSWELL et al. (1996). For this, the pre-storm environment is of interest. In the case study several variables relating to the environmental stability, moisture and lifting are extracted from the WRF model for analysis. The chosen variables are the convective available potential energy (CAPE), convective inhibition (CIN), Theta-E at 850 hPa, relative humidity (RH) and the horizontal windspeeds. The variables are analyzed qualitatively using horizontal maps, vertical cross-sections (VCS), and skew-T-log-p diagrams of model generated pseudo soundings.

After characterizing the environment leading to convection and its temporal evolution, the focus lies on the stationarity in a second step. Following the theory presented in Chapter 2.1, the main interest here lies with the influence of the topography on the downdrafts as well as the windspeeds and the low-level moisture transport.

## 5 | Results

This section is split into three subchapters. First, the analysis of the different stationarity definitions is presented (Chapter 5.1). Then, the climatology produced with the chosen definition is described (Chapter 5.2). Finally, the results of the Bumbach case study are shown and analysed (Chapter 5.3).

### 5.1 Stationarity Definition Comparison

As the first step of this thesis, five different indices for the definition of a *SCS* are tested. They are each tested for different multiple time/distance/overlap thresholds, and in the end, the *ETESp* definition is chosen with a distance threshold of 25 km and a time threshold of 90 minutes ( $ETESp_{t90,d25}$ ).

#### 5.1.1 Overlap Stationarity

*OS*, by definition, has the advantage that these cells have precipitated over the same area for a prolonged amount of time. However, the *OS* criteria captures not only stationary cells but also large cells moving over an area, especially when the overlap threshold is set relatively low. Figure 9 shows the case of a cell which is classified as stationary with  $OS_{t90,o50}$ . The cell has an overlap area of 51.3% at a time threshold of 90 minutes. While the cell has this relatively large overlap area, the centroids of the two timesteps shown are approximately 40 km apart, which is relatively far. For this thesis, we are interested in slow-moving cells which makes this an inadequate classification. A way to have fewer of these misclassified convective storms is to have a higher overlap percentage. However, increasing the percentage leads to a smaller number of classified cells. At a 50% overlap, 0.85% of all cells are classified as stationary. At 60% this drops to 0.7% and at 70% to 0.55% or 1848 cells.

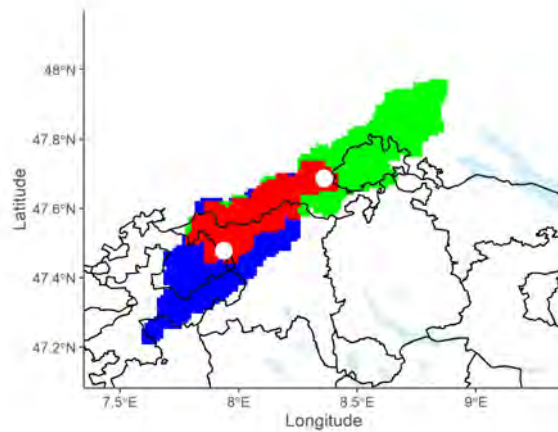


**Figure 9:** Example of  $OS_{t90,d50}$  applied to a large storm cell over northern Switzerland on the 10.04.2006 at 4:30 MESZ. The blue area marks the cell footprint at the initial timestep, the green area marks the footprint of the same cell 90 minutes later. The red area marks the overlap between the two cell footprints which is 51.3%. The white dots denote the cell centroids for the two timesteps.

### 5.1.2 End-to-end Stationarity vs Path Stationarity

The different distance-based definitions lead to similar results. Generally, all cells classified by the *PS* definition are also found in the *ETES* definition for the same time and distance thresholds. The *ETES* definitions classify more cells as stationary, which is expected due to the difference in definition. For both definitions, the partial version (p) allows for substantially more stationary cells than the lifetime version (l). With a time-threshold of 90 minutes and a distance threshold of 25 km the  $ETESp_{t90,d25}$  definition classifies 7622 *SCS*,  $ETESl_{t90,d25}$  4506 *SCS*,  $PSp_{t90,d25}$  2088 *SCS*, and  $PSl_{t90,d25}$  737 *SCS*.

The large difference between the  $ETESp$  and  $PSp$  definitions stems from the fact that the centroid of the storm cells is used to calculate the distances. This turns out to be problematic because the centroid not only moves due to the movement of the cell but also due to a change in the size of a cell. Rapid changes in cell size, as well as splitting of cells, can lead to a "jumping" centroid which drastically affects the  $PSp$  distance. An example of this behaviour can be seen in Figure 10. The plot shows part of a path of the cell centroid of a storm moving along the Jura in a north-easterly direction. This storm moved at a relatively constant speed and direction, but its size varied greatly over time jumping from 110 km<sup>2</sup> up to 400 km<sup>2</sup>, back to 63 km<sup>2</sup> and again up to 2090 km<sup>2</sup> leading to a zig-zagged path. This path's end-to-end distance is 55 km while the whole path has more than triple that length at 186 km.

The caveats of the definitions *OS* and *PS* lead to the choice of the *ETES* definition for this thesis. Specifically, the  $ETESp$  definition is used because it allows for more cells to be classified as stationary. It was decided that stationarity over part of the *SCS* lifetime was sufficient. Additionally, the  $ETESp$

definition is similar to the definition of stationary cells used in SODERHOLM et al. (2014), which allows some comparability.

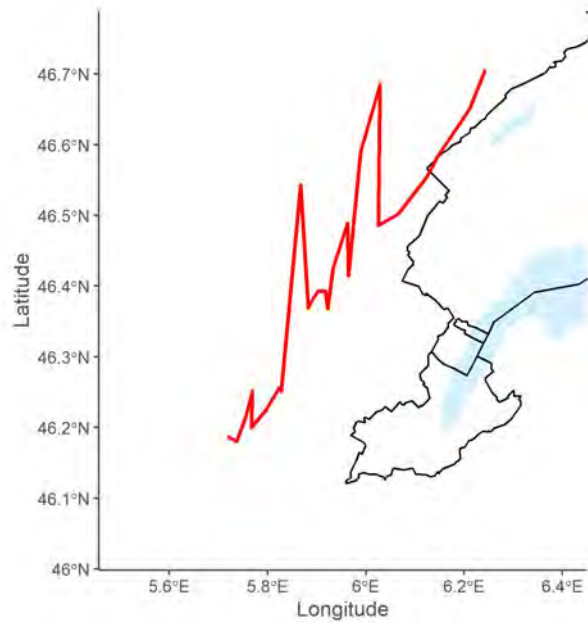


**Figure 10:** Example of a 90-minute path of a storm cell centroid (4.7.2008 13:55 MESZ) in red with a 5 minute temporal resolution.

### 5.1.3 Threshold Choice

It is observed that the convective events are spread over a continuum of track lengths as can be seen in Figure 11. Similar results are described by SODERHOLM et al. (2014). Due to this, the choice of the distance threshold is arbitrary. As previously mentioned, SODERHOLM et al. (2014) choose 25 km because it is the cross-ridge length of the Black Hills, where they conducted their observations. This thesis's study region is orographically much more complicated, which is why there is no simple choice for the threshold with the same rationale. However, 25 km also relates approximately to the length of catchments which typically react to convective storms. For example, the Zulg River in the Bernese Prealps, known for being prone to flash floods, has a drainage area about 23 km in length (RUIZ-VILLANUEVA et al. 2017). For this reason, and for comparability's sake, the same threshold of 25 km is chosen.

For the time threshold, 90 minutes are selected similar to SODERHOLM et al. (2014) because it is sufficiently long for heavy precipitation to accumulate, and because it is a characteristic lifetime of longer-lived multicell and supercell storms (e.g. DOSWELL 2001). A 120-minute threshold was tested but resulted in too few categorised SCS for the climatology.

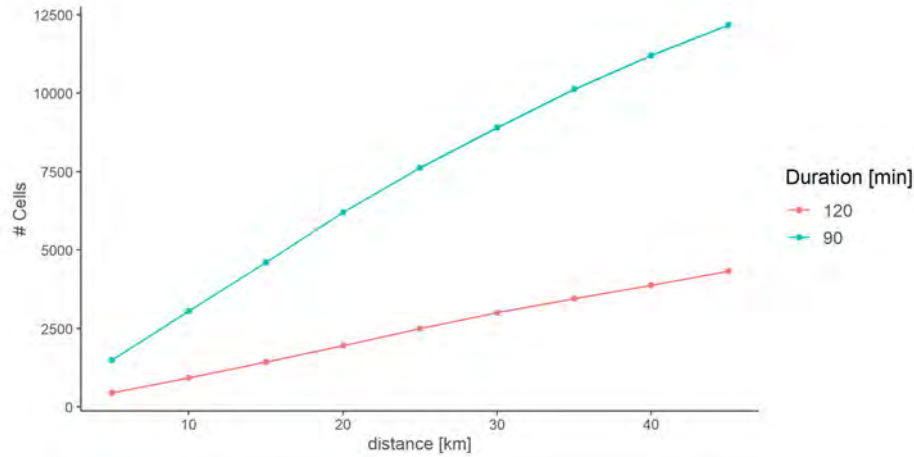


**Figure 11:** Number of SCS cells at different distance thresholds [km] based on the  $ETESp$  definition of stationarity. The plot shows a curve for a 90 (blue) and a 120 (red) minute temporal threshold.

## 5.2 Climatology Results

The SCS described in the climatology are based on the  $ETESp_{t90,d25}$  definition. In total 218'650 storms are analysed over the 14-year timeframe. Of these 7622 (3.49%) are classified as SCS, 2554 (1.12%) as *LTL*D, and 208474 (95.35%) as *OTHER*. Note that the SCS and *LTL*D classifications are not mutually exclusive. However, only 70 Storms fall into both categories.

### 5.2.1 Annual Variability

Over the 14-year study period, the number of storms overall increases slightly by, on average, 5.2% per year. The number of SCS also increases (14.8%), while the *LTL*D storm frequency decreases (-5.0%) (Figure 12 top row). However, there is high year-to-year variability. In Figure 12 (bottom row), the standardised storm count anomalies for all storm types are shown. The anomalies of SCS overall follow the *OTHER* anomalies at lower magnitudes except 2018, where they reach almost 2.9 Standard deviations. The anomalies of the *LTL*D storms differ from the other two groups and are often of opposite sign. Especially in years with large deviations (2005, 2012, 2014, 2016, 2018) although not always (2009, 2015).

Generally, a convective season with a large number of storms coincides with frequent SCS. In most years, the fraction of SCS is between 2.8% and 3.8% of all cells. The exceptions are 2008 (1.9%) and 2018 (5.4%). The *LTL*D cells vary between 0.3% (2018) and 2.1% (2008) with 2008 being the only year where there are more *LTL*D than SCS cells.

The statistical comparison of the distributions for all areas combined (*SCS/OTHER* 25%, *LTL*D/

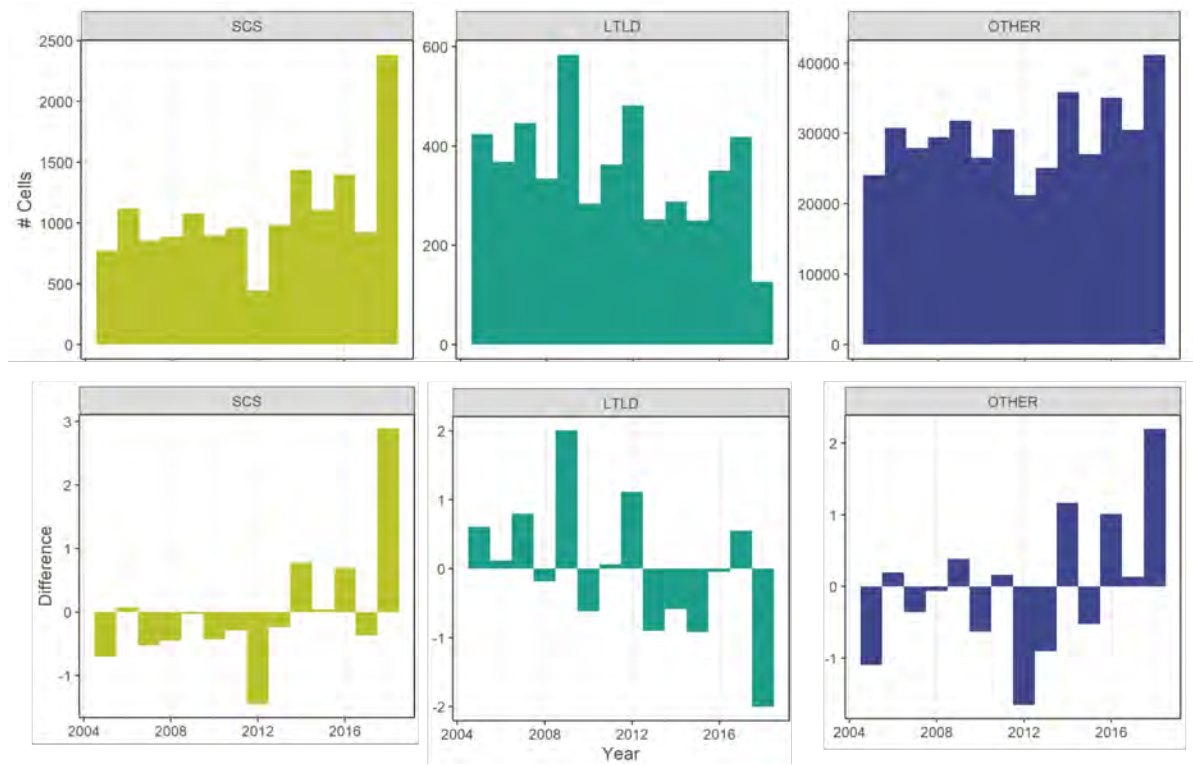


**Figure 12:** Annual number of detected convective storms (top row) and annual standardised storm number anomalies (bottom row) separated by storm type.

*OTHER* 70%, *SCS/LTLD* 100%) shows that the *SCS* differ significantly from the *LTLD* storms but not from the *OTHER* storms. However, when the sub-regions are considered separately, the results vary. While the distributions of *SCS/LTLD* differ significantly in all subregions those of *LTLD/OTHER* do not. In fact, there is no subregion where this comparison reaches above 41%. *SCS/OTHER* do not differ significantly in any sub-region.

## 5.2.2 Weather Type and Circulation

Figure 13 shows the distribution of the three storm types in different weather situations. Generally, thunderstorms over Switzerland are most frequent in westerly (36.0%) to south-westerly (33.7%) GWT. This distribution applies to all sub-regions of the study area. The same is true for *SCS* (W 28.7%, SW, 25.0%). However, they occur more often in all other GWTs, especially in northerly (12.2% vs 8.8% for *OTHER*) and southerly (7.8% vs 5.9% for *OTHER*) weather. In contrast, *LTLD* cells occur almost exclusively in westerly to south-westerly (combined 94.9%) flow. Overall, the *LTLD* storms differ significantly from the *SCS* (100%) and the *OTHER* storms (97.4%). However, between *OTHER* and *SCS* the difference in related weather types is less significant (33.7%).



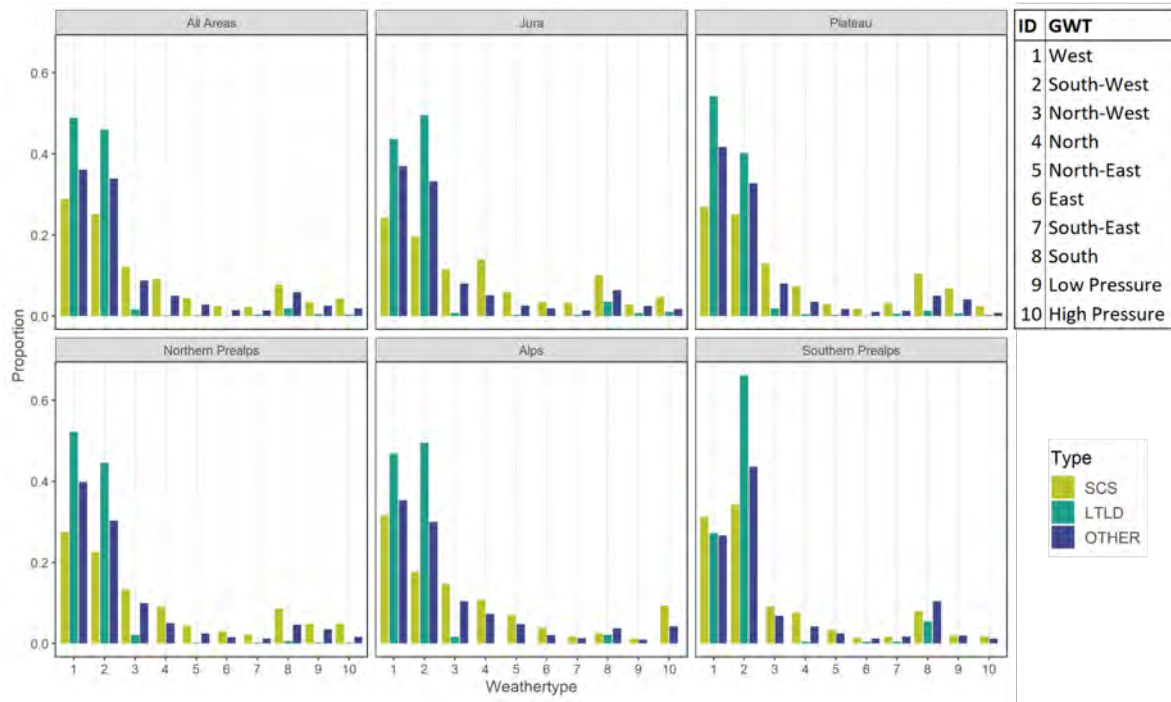


**Figure 13:** Distribution of the different storm types by GWT. The table on the top right shows the meaning of the numbers on the x-axis in the plot on the left. The six subplots show the distribution for the whole study region (top left) and for each sub-region.

For a more detailed view, Figure 14 shows the mid-tropospheric wind direction at 750 hPa. These winds are at lower elevations than those used in the GWT definition, based on 500 hPa wind speeds and direction. At these lower heights, the wind direction distribution is similar to the GWT's when looking at *OTHER* cells with 51.3% of them happening during SW-NW Winds. The *LTLD* cells have 88.8% of all cells happening with S-NW Winds. While 40.2% of the *SCS* cells also happen with SW-NW Winds, the image becomes a bit more varied when looking at the sub-regions. North of the Alps the *SCS* also happen frequently with northerly winds, especially in the Jura (NW-NE: 33%). Here the three storm types differ significantly overall (*OTHER/SCS* 98%, *OTHER/LTLD* 100%, *SCS/LTLD* 100%) and in all subregions with one exception; in the southern Prealps *OTHER/SCS* do not differ significantly (37%).

Looking at the wind speed data (Figure 15), we can see that the *SCS* cells in Switzerland are related to locally slower wind speeds than both other storm classes. The wind speeds are on average  $7.2\text{ms}^{-1}$  for *OTHER* cells while the *SCS* windspeeds are lower at  $5.5\text{ms}^{-1}$  and the *LTLD* ones higher at  $9.3\text{ms}^{-1}$ . For *SCS*, 89.4% of the storms happen at wind speeds below  $10\text{ms}^{-1}$ . These differences are significant overall (*OTHER/SCS* 100%, *OTHER/LTLD* 100%, *SCS/LTLD* 100%) and in all sub-regions.



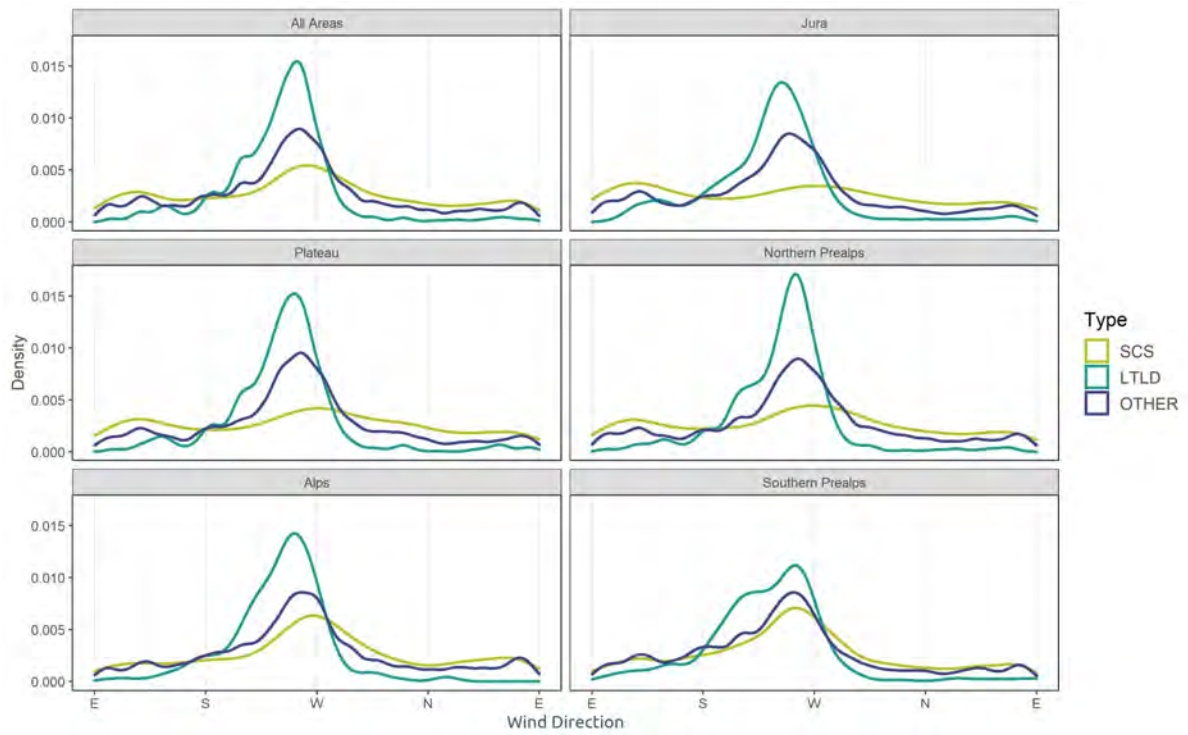


**Figure 14:** This Figure shows the distribution by ERA-5 wind direction at 750 hPa for each storm type. The six subplots show the distribution for the whole study region (top left) and for each sub region.

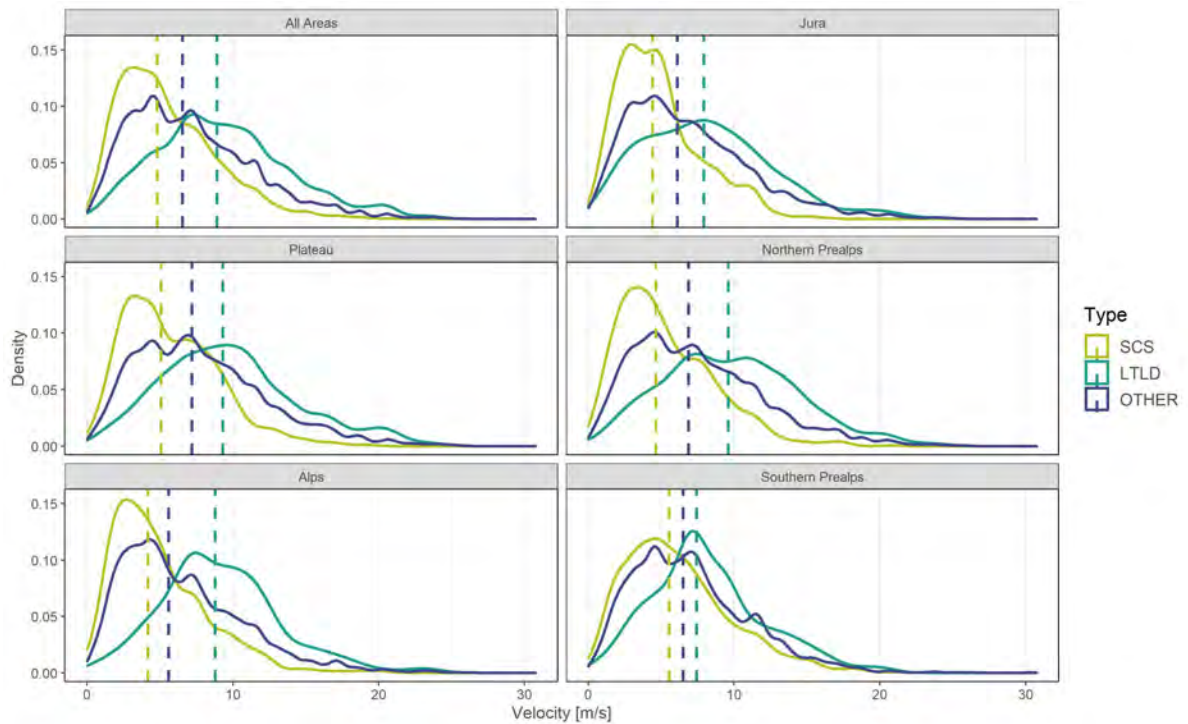


**Figure 15:** Same as Figure 14 but for the wind speed. The dashed lines additionally show the median values for each storm type.

### 5.2.3 Monthly Distribution

The monthly distribution (Figure 16) shows a significant seasonal cycle of the *SCS*, similar to the general distribution of *OTHER* cells with a peak in June/July. For the *LTL*D storms, the peak is later in July/August. These distributions are similar for all investigated subregions although the *SCS* show a more pronounced peak in the June in Jura and July in the Alps.

Looking at the monthly frequency of the different GWTs over Switzerland we can see that the types 1 (West) and 2 (South-West) are most frequent in July and August and least frequent in April (in the convective season). This explains the distribution of the *LTL*D cells, which almost exclusively occur in these weather types. *SCS* cells also occur most frequently with the GWT 1 and 2 but are also frequent in GWT 3 (North-West) and 8 (South). These two weather types are most common in May and June respectively, which also reflects in the *SCS* distribution.

Overall, the monthly distribution of *SCS/LTL*D differs significantly in all areas, but the Alps (56%). *OTHER/SCS* do not differ significantly in the northern Prealps (5%), Alps (1%) and the southern Prealps (1%). However, there is some significance in the differences in the Jura (47%) and the Plateau (45%). In contrast, *OTHER/LTL*D differ significantly in the three alpine sub-regions, but there is almost no significant difference in the Jura (27%) and the Plateau (28%).

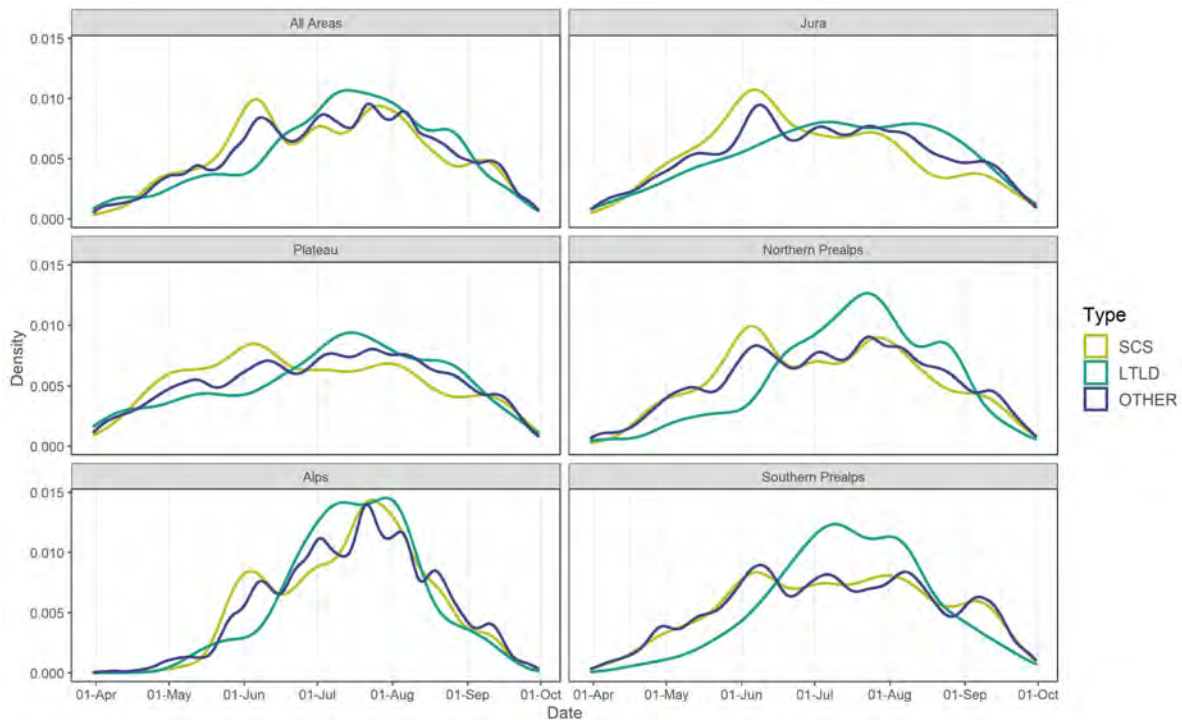


**Figure 16:** Same as Figure 14 but for the monthly distribution of the storms.

### 5.2.4 Diurnal Cycle

Figure 17 shows the initiation times of the convective storms. The convection over Switzerland shows a distinct diurnal cycle. For the *SCS* this cycle is even more pronounced with most of the storms initiating in the late afternoon. There are regional differences with Jura and the Alps showing the most distinctive diurnal cycle, especially for the *SCS*.

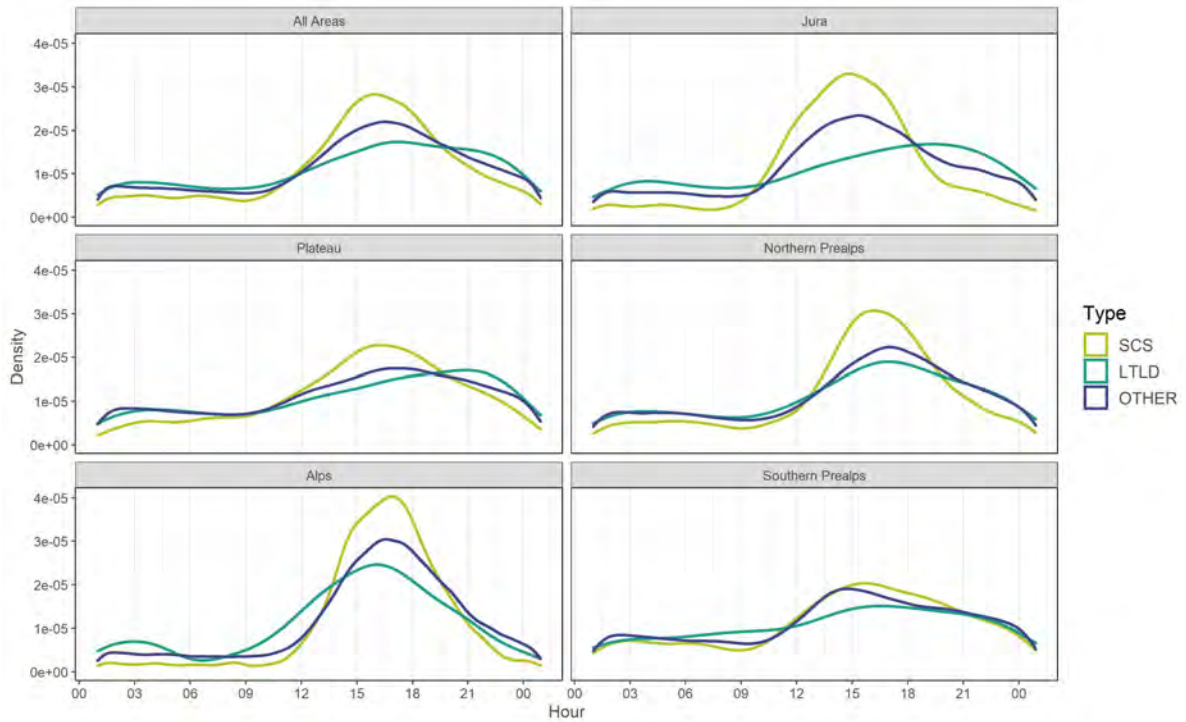


**Figure 17:** Same as Figure 14 but for the hourly distribution of the storms.

The initiation times of the *LTLD* storms are more spread out, with many initiating in the late evening or early morning. Statistically, the *SCS* and *LTLD* differ significantly (100%) in all regions except for the southern Prealps where the difference is less significant (56%). Furthermore, *SCS/OTHER* differ significantly (74%-100%) everywhere except the southern Prealps (5%). However, the comparison of the *OTHER* storms with the *LTLD* storms is more varied. They differ significantly in the Jura (97%), less significantly in the Alps (53%) and the Plateau (29%) and barely in the southern (14%) and northern (5%) Prealps.

### 5.2.5 Spatial Characteristics

The *SCS* and *LTLD* frequencies are different for each subregion. Though, the differences are relatively small. *SCS* are most frequent in the southern Prealps, followed by Jura and the northern Prealps. In contrast, the *LTLD* storms were most frequent in the Plateau region. All the frequencies can be seen in

Table 4. *SCS* were most prevalent in mountainous regions.**Table 4:** Number of cells, density (cells per  $km^2$ ), and percentage of each storm type for all subregions of the study area.

Area	Jura	Plateau	N. Prealps	Alps	S. Prealps
<b># Cells</b>	23294	44057	58101	46183	47085
<b>Density [cells pro <math>km^2</math>]</b>	2.76	3.35	3.84	1.10	3.47
<b>% <i>SCS</i></b>	3.29%	3.07%	3.28%	3.03%	4.67%
<b>% <i>LTL</i></b>	1.64%	2.27%	1.25%	0.41%	0.55%
<b>% <i>OTHER</i></b>	95.07%	94.66%	95.48%	96.56%	94.78%

Figure 18 shows the initiation location for the *SCS* and *LTL* storms. Storms are grouped into a region using their average location, which means that their initiation location can be outside of this region. This distribution is especially apparent with the *LTL* cells which often initiate west of the Jura and in western Switzerland. This result fits with the previous results regarding the movement and weather types correlating with that cell type.

For *SCS* the distribution looks a bit different. The highest densities of initiation locations can be found in the western Jura and close to the northern and southern Prealps. These initiation locations correlate with the orography of the study region. For both cell types, most of the storms initiate along the Alps' foothills and the Jura.

Figure 19a shows for each pixel the number of *SCS* cells during the 14-year period. Maximum counts (2800-2843) are located in the southern and northern Prealps, and the Jura especially close to the three Radar stations of Monte Lema, La Dôle and Albis. However, this distribution mirrors the general distribution of convective storms over Switzerland (not shown).

In Figure 19b, the fraction of *SCS* out of all storms is shown. This reveals that there are large areas of Switzerland where *SCS* only make up less than 10 % of all storm cells. Nevertheless, there are some hot spots, namely in the southwestern Jura, the lower Valais, the Tessin and in Eastern Grisons where the fraction reaches up to 38%



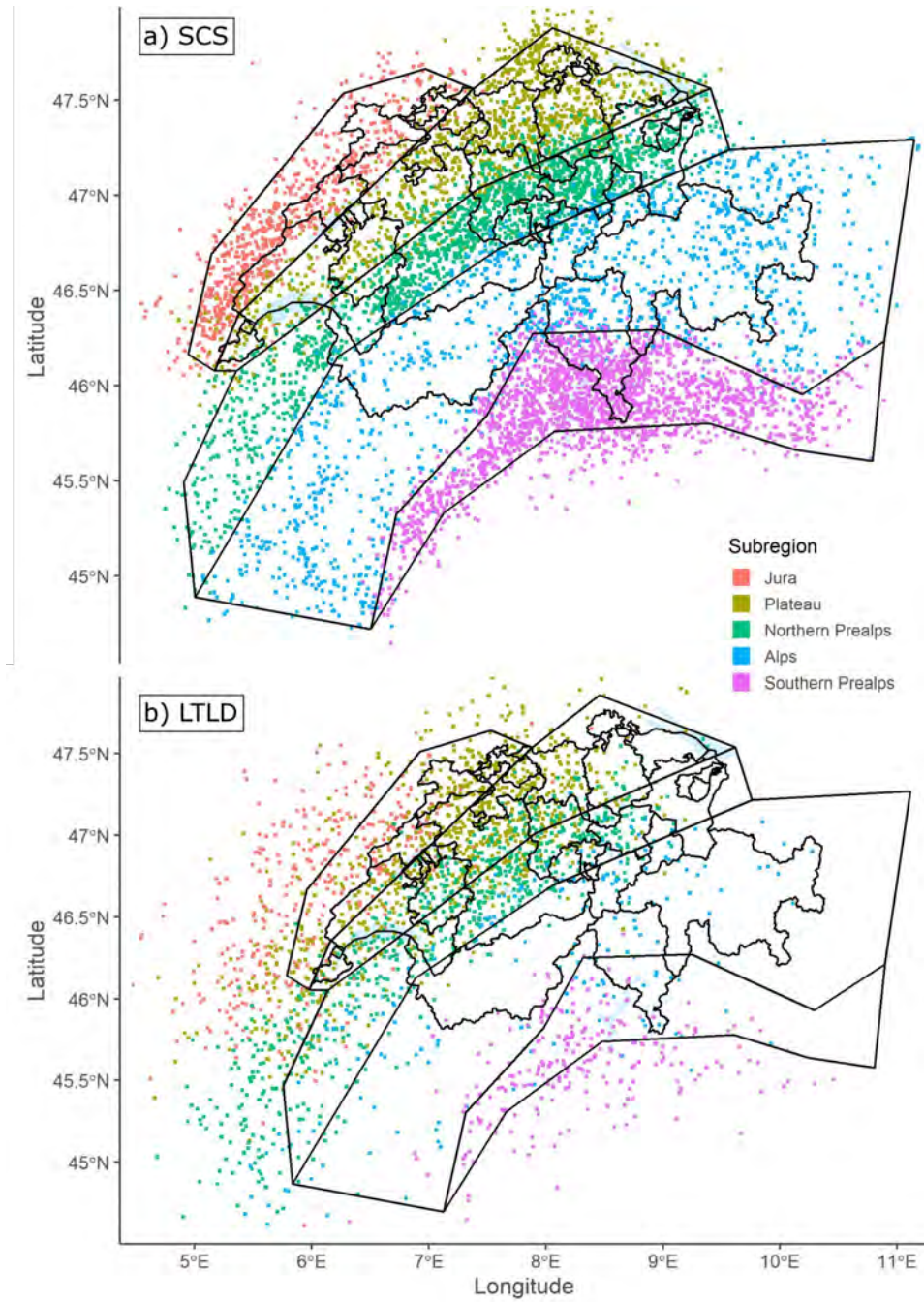


**Figure 18:** Initiation locations of *SCS* (a) and *LTLD* (b) cells. The colours signify the subregion into which the cell was categorised. The categorisation is based on the average location of the storm cell during its lifetime.

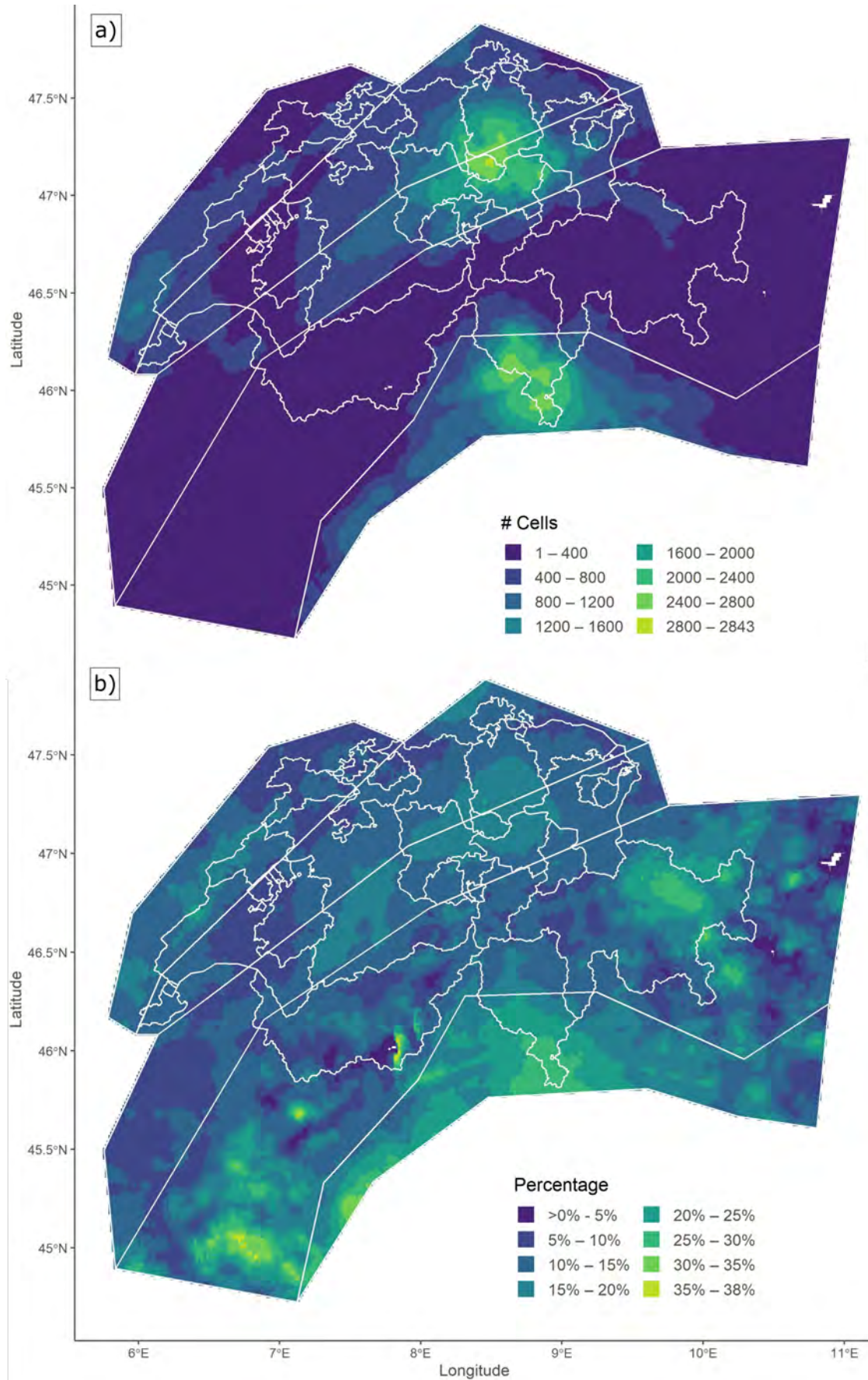


**Figure 19:** a) Number of SCS cells which hit each point during the 14 years. b): Fraction of the total number of storm cells which hit each point, which were classified as SCS.

### 5.2.6 Precipitation Characteristics

The mean rainfall rate from *SCS* on average is 10.8 mm/h which is slightly lower than that of *LTLD* cells (11.0 mm/h) and higher than the average of all cells (8.3 mm/h) (Figure 20). Looking at the maximum 5-minute rainfall rates, the difference between the long-lived and short lift storms is even more pronounced. Here the mean of *SCS* is 74.8 mm/h, and the one of *LTLD* is 81.6, both of which are far higher than the average of all cells at 35.1 mm/h (Appendix 2).

Another noteworthy difference is that the Jura as the only region exhibits stronger rainfall rates for *SCS* than for the *LTLD*. The mean/max precipitation rates of the three storm types differ significantly in all subregions (*OTHER/SCS* 100%, *OTHER/LTLD* 100%, *SCS/LTLD* 94%) However, if all areas combined are considered, the *SCS/LTLD* distributions do not differ significantly (3%) which indicates that it is critical to look at the different subregions independently.

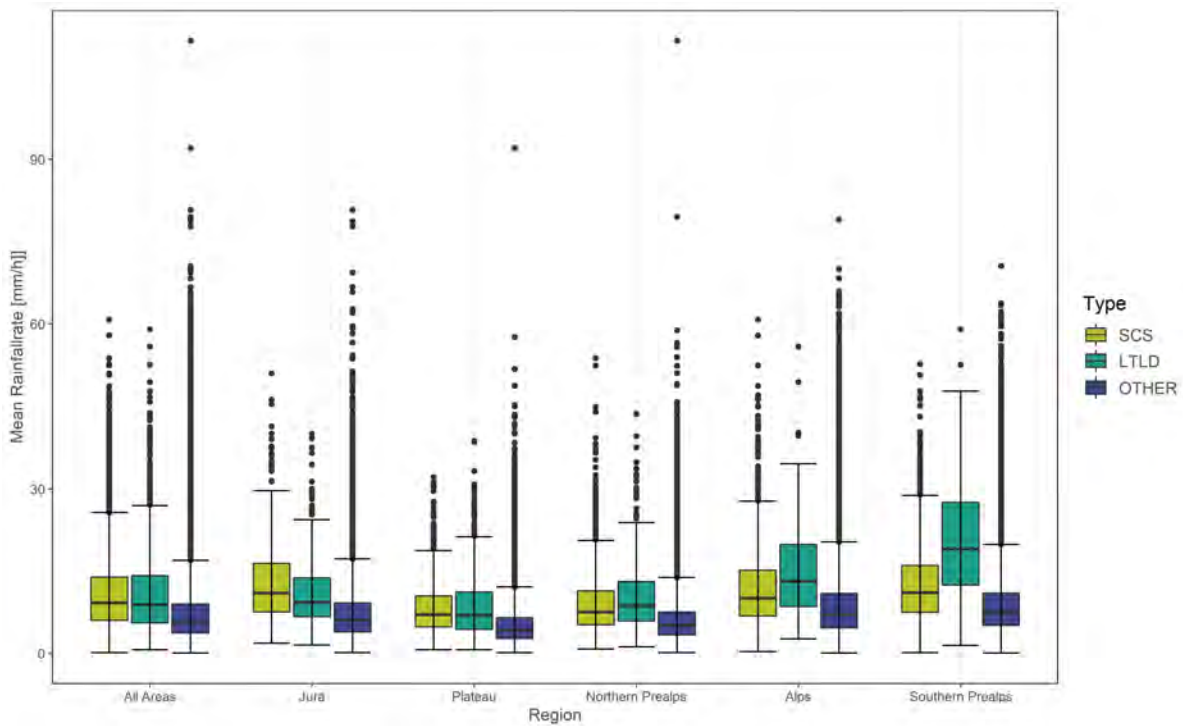


**Figure 20:** Mean rainfall rate per storm cell averaged over all storm cells for each type and split by subregion.

While the *SCS* cells seem to be less intense than *LTLD* cell, they are still capable of high rainfall rates. The effects of these rates, combined with the stationarity, can be seen in Figure 21, which shows the mean precipitation per pixel caused by a single convective cell. On average, an *SCS* causes 5.7 mm of precipitation for the area it passes over. *LTLD* cells produce less than half at 2.6 mm, and *OTHER* cells only produce 1.9 mm.



When looking at the maximum rainfall accumulations caused by single cells, the *SCS* are also on top with on average 33.4 mm compared to the 14.7 mm for *STLD* and the 8.2 mm for all cells. Here the effect of the stationarity becomes visible (Appendix 2).

These differences are significant (*OTHER/SCS* 100%, *OTHER/LTLD* 100%, *SCS/LTLD* 100%) in all areas except for the southern Prealps. There the difference in rainfall rates between *SCS* and *LTLD* compensates for the stationarity such that the difference between those two storm types for precipitation accumulation is less significant (37%).

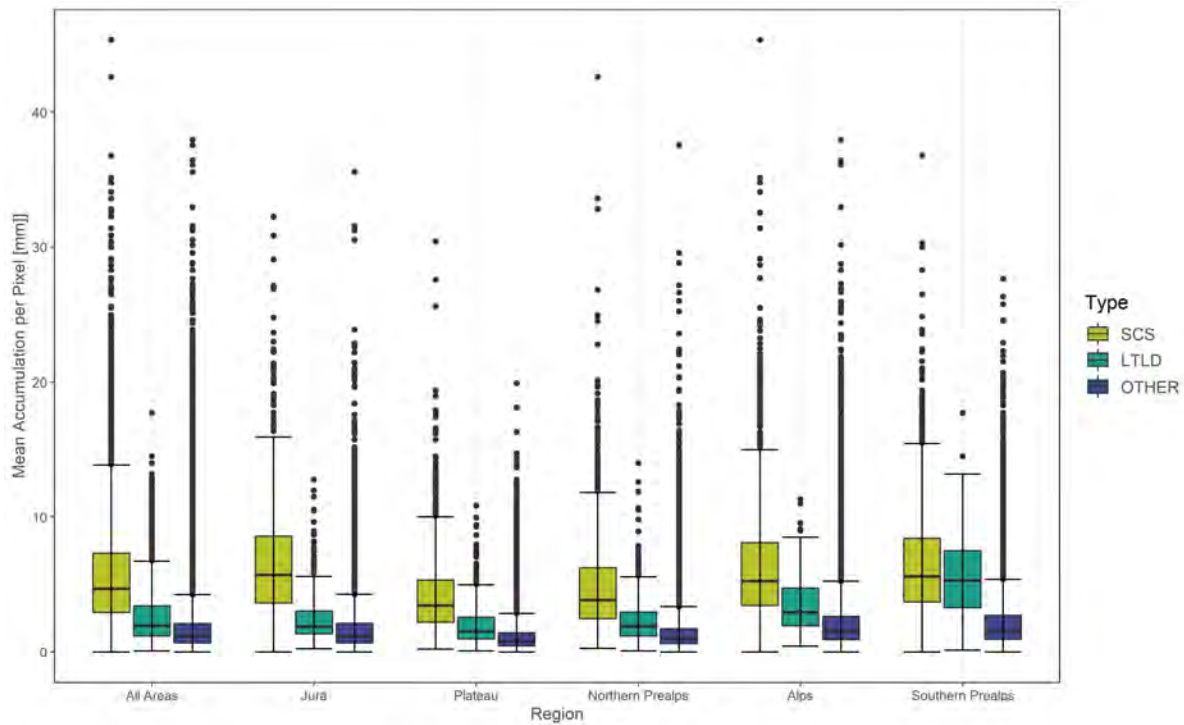


**Figure 21:** Like Figure 20 but for the mean accumulated precipitation per pixel caused by a single storm.

Due to the high rainfall accumulations, *SCS* could be important for extreme precipitation events over Switzerland. It is of interest to look at the top precipitating storms and determine the fraction of *SCS* to see whether they are disproportionally common considering their low overall frequency. Figure 22 shows the fraction of the top 100 highest precipitation storms, which are *SCS* for each pixel. This Figure reveals that *SCS* are a crucial contributor to the events with the highest precipitation values, in some areas. For example, in parts of the Bernese Prealps, the *SCS* make up only 10-15% of the total cells (Figure 19b) but are responsible for up to 60% of the highest convective precipitation events (Figure 22). Similarly, there are widespread regions where *SCS* are responsible for more than 50% of the most precipitating storms in the western Jura.



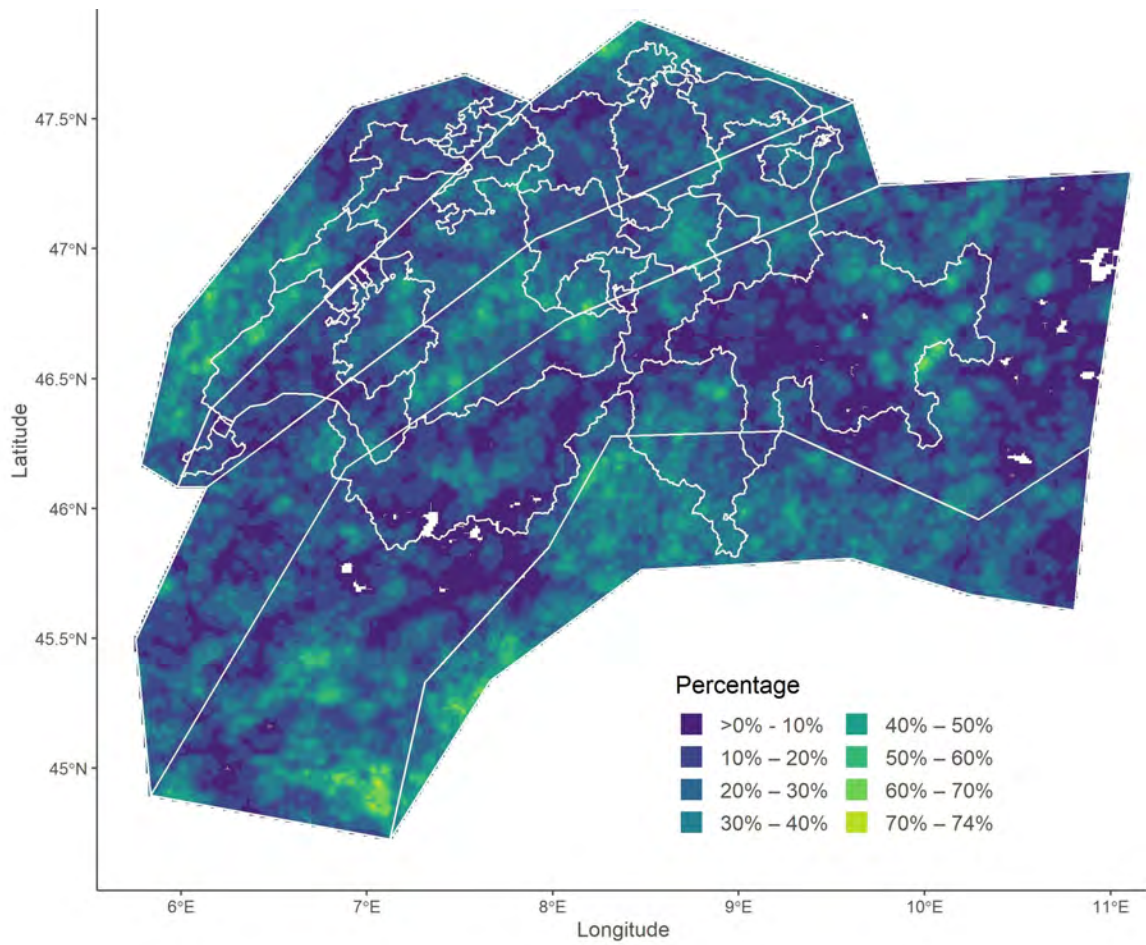


**Figure 22:** Percentage of the top 100 convective precipitation events classified as stationary, for each pixel.

### 5.3 Case Study Results

The early morning of the 24.07.2014 was convectively very active in the northern Prealps and Alps in general and in the study area. The WRF model shows the first convective cells close to the study region initiating at 05:10 CEST with two more following around 05:45 CEST. These first cells moved relatively slowly to the south and dissipated around 07:15 CEST. A second set of cells initiated at 09:10 CEST and moved out of the study region towards the south-west. Shortly after, two cells from the north-east moved into the study region and merged with an intensive cell which initiated around 10:20 CEST and then dissipated around noon. Finally, a third set of cells with eight small cells initiating and dissipating between 12:45 and 17:00 CEST moved over the area.

The model produces convection close to the Bumbach area roughly at the right time. However, the model precipitation maxima are located further south and show lower accumulated rain sums compared to the observations (Figure 23). In Figure 23a the WRF model's accumulations are shown. When accumulating all cells' precipitation over the whole morning, the highest values reach 93 mm. In comparison, the accumulated CombiPrecip measurements for the stationary cell, which initiated at 7.30 CEST, are much higher (Figure 23b). This is the cell which was classified as stationary by the definition in the first part of this thesis. In this data, the single-cell led to accumulations of up to 166.8 mm north-west of Bumbach.

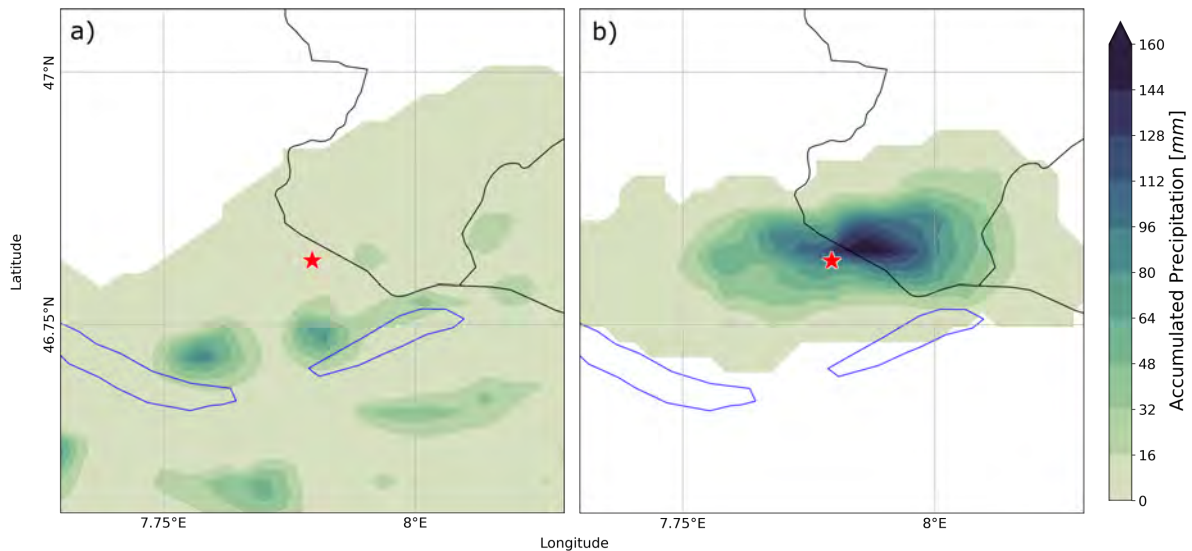


**Figure 23:** These two figures show the precipitation accumulations near Bumbach on the morning of the 24.07.2014. The total accumulated precipitation until noon on the 24. from the WRF model is shown in Figure a. In Figure b, the CombiPrecip values for the stationary cell, detected in the climatology, are shown. The Location of Bumbach is marked with the red star. The blue lines mark the locations of lake Thun and lake Brienz. The black lines demarcate the cantonal borders.

The model is not able to simulate the intense stationary cell which hit Bumbach. For this reason, the following results will focus on the general weather conditions in the area over the whole morning of the

24.07.2014. The aim is to characterise the mesoscale conditions necessary for stationary convection under the assumption that the model was able to reproduce these.

As a first ingredient of the convection Figure 24a shows a south-north cross-section of RH over the Bumbach region at 05:00 CEST before the first cells initiate. There is a layer of high RH (70-100%) up to approximately 5 km altitude over the whole region with the highest values (90-100%) concentrated over the Hohgant mountain ridge. Above of this moist layer, there is a mid-tropospheric (5-6.5 km) dry air layer (20-40%) which is then followed by another moist (70-100%) layer (6.5-9 km). Finally, there exists another, drier, layer up to the tropopause (30-50%). Figure 24b shows the temporal evolution of the moisture at the Bumbach location. Between 03:00 CEST and 11:00 CEST, there is a slight increase in moisture close to the ground; however, the change is small.

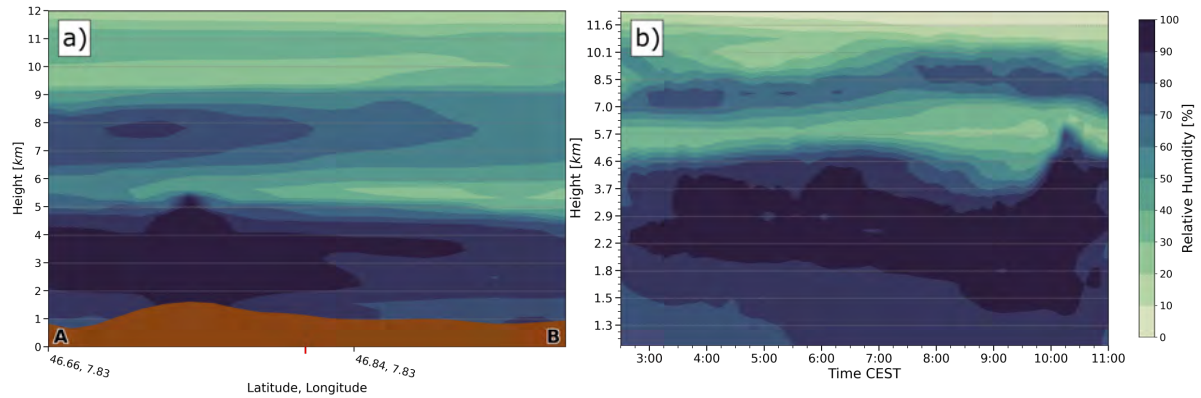


**Figure 24:** a): Vertical north-south cross-section of the RH [%] over Bumbach on the 24.07.2014 at 5:00. Bumbach is marked with the red tick on the x-axis. B): Temporal evolution of RH over Bumbach starting at 3:00 and ending on 11:00.

The first convective cell initiates to the south-west of Bumbach, which is also the location at which the potential for convection was the highest shortly before initiation. However, this convective cell initiated south of the Hohgant mountain ridge and not on the north side where Bumbach lies. Figure 25a shows CAPE and CIN just before the initiation. There is relatively high CAPE available ( $500-600 \text{ Jkg}^{-1}$ ) with low values of CIN ( $<5 \text{ Jkg}^{-1}$ ) at the location of initiation. In contrast, CIN is more than  $10 \text{ Jkg}^{-1}$  in surrounding areas. After the storm initiation, the CAPE decreases to below  $300 \text{ Jkg}^{-1}$  (Figure 25b) and remains low until 9:00 CEST when it starts to increase again. At first only north of the Hohgant at the same longitude in which CAPE was previously high (Figure 25c) but later also in a more widespread region north of the Hohgant and Schrattefluh close to Bumbach (Figure 25d). In the same timeframe, CIN decreases over the whole Bumbach region.

A different tool for assessing the stability of the atmospheric layers is the skew T-log p diagram. Here the CAPE at the location of the pseudo sounding is shown with a red shaded area. Figure 26 shows two of those diagrams generated from pseudo soundings at the Bumbach location. As mentioned above,

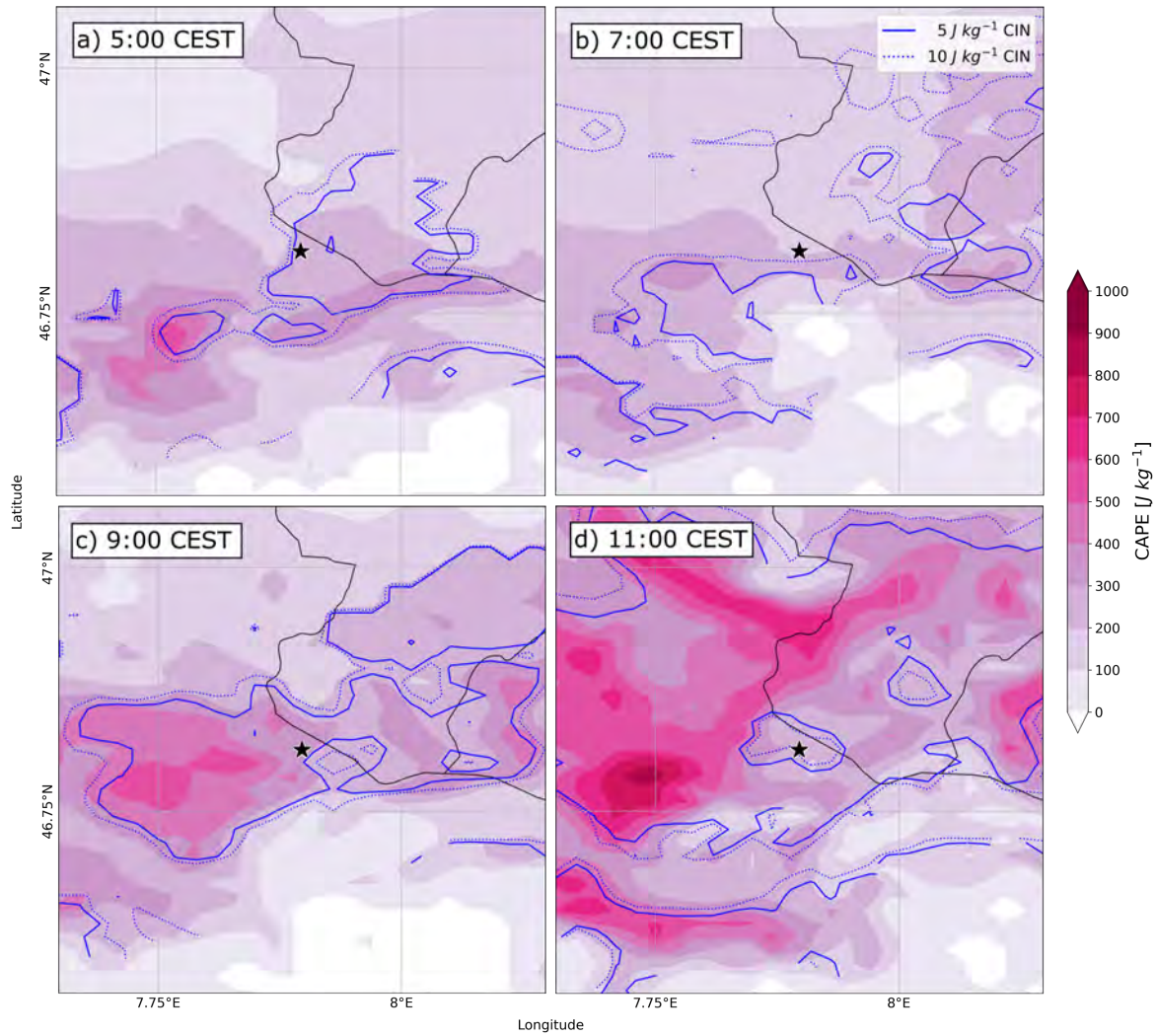


**Figure 25:** These plots show a horizontal map of CAPE [ $J kg^{-1}$ ] and 5 and  $10 J kg^{-1}$  contour lines (blue) of CIN. On the 24.07.2014 at 5:00 CEST (a), 7:00 CEST (b), 9:00 CEST (v), and 11:00 CEST (d). The Location of Bumbach is marked with the black star. The blue lines mark the locations of lake Thun and lake Brienz. The black lines demark the cantonal borders.



there is no CAPE visible until about 9:30 CEST. Then a conditionally unstable layer from about 700 hPa to 400 hPa starts to build up. The diagram further shows the dry layer from 850 to 400 hPa, which is later found at lower levels from the surface up to approximately 550 hPa. The skew T-log p diagramm provides additional information about the horizontal wind speed and direction throughout the air column. At 5:00 CEST there is directional wind shear above Bumbach with weak (5-10 kt) easterly wind at low levels but slightly more substantial (15-20 kn) westerly wind above 500 hPa height. At 9:30 CEST the situation is similar in regard to the wind field.

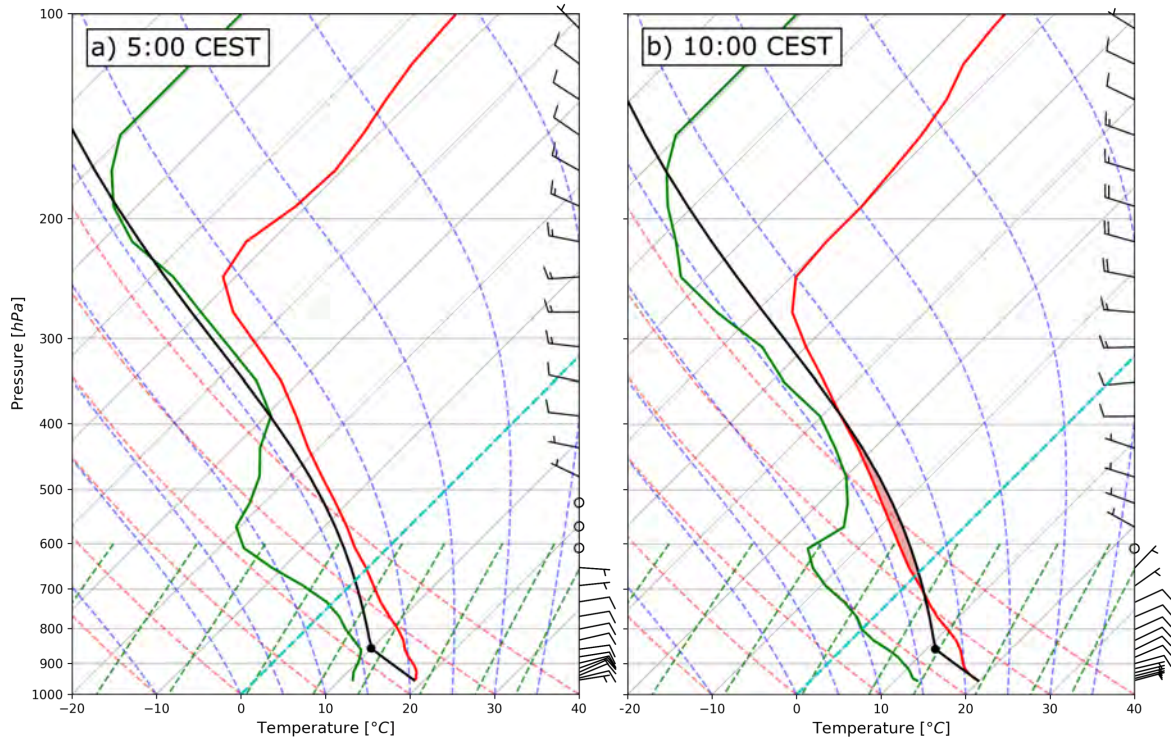


**Figure 26:** Skew T-log p diagrams for two model generated pseudo-soundings at the location of Bumbach at 5:00 CEST (a) and 10:00 CEST (b). The figure shows isobars (horizontal grey gridlines) and isotherms (skewed grey gridlines and marked zero degrees line in turquoise), as well as isohumes (green dashed line), pseudo-equivalent potential temperature (moist adiabats, blue dashed line), and potential temperature (dry adiabats, red dashed line) and. The red line shows the simulated absolute temperature, and the green line the dewpoint temperature (green line). The calculated path of a vertically rising air parcel from the surface is marked with a black line on which the black dot signifies the lifted condensation level. The wind speed [kn] and direction are also presented with the wind barbs along the right y-axis.

In Figure 27a, a vertical cross-section of the Theta-E values over Bumbach before the initiation of the first convective cell is shown. There are lower Theta-E values (318-322K) in the mid-troposphere over the higher surface levels (326-330), indicating potential instability in the air column. This vertical gradient is similar over the whole VCS; however, there are overall slightly higher values of Theta-E towards the south. Over Bumbach, the vertical gradient increased over time (Figure 27b) with the highest gradients between 8:00-11:00 CEST.

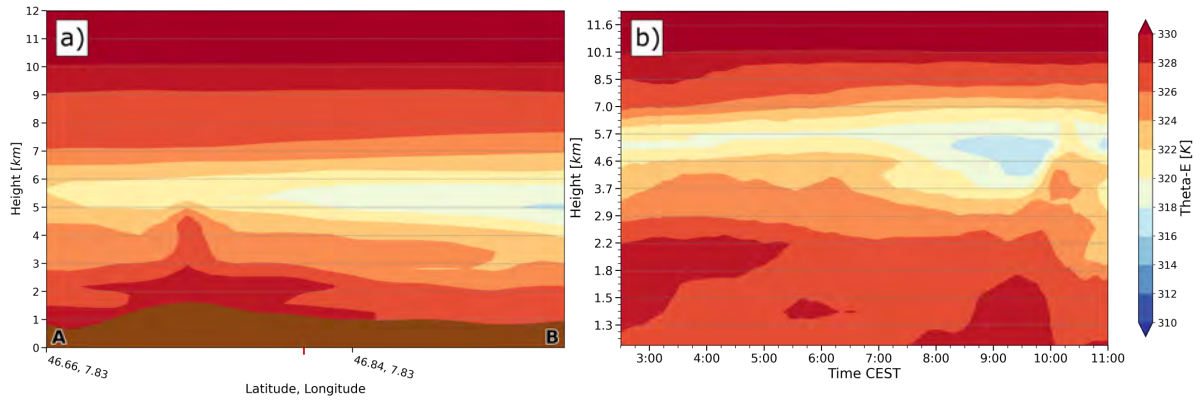


**Figure 27:** a): Vertical north-south cross-section of equivalent potential temperature (Theta-E) [K] over Bumbach on the 24.07.2014 at 5:00 CEST. Bumbach is marked with the red tick on the x-axis. b): Temporal evolution of Theta-E over Bumbach starting at 3:00 and ending on 11:00 CEST.

For stationary convection, the horizontal winds are a key factor. On the 24.07. in the early morning, they were relatively weak throughout the air column. At 5:00 CEST, the winds were near  $0 \text{ ms}^{-1}$  at 800 hPa (Figure 28a). Throughout the morning, they slowly changed to  $1.5\text{--}2 \text{ ms}^{-1}$  northerly winds at 09:00 CEST (28b, c). Later, until 10:00 CEST, they rapidly increased to  $6 \text{ ms}^{-1}$  north-easterly winds (Figure 28d). At intermediate altitudes of 650 hPa, the wind speeds stayed low ( $<2.5 \text{ ms}^{-1}$ ) throughout the morning. Further up, at 500 hPa, a similar strengthening of the winds from  $1.5\text{--}2 \text{ ms}^{-1}$  to about  $6 \text{ ms}^{-1}$  is observed over the same timeframe. However, here the winds come from a westerly direction (not shown). This vertical wind profile leads to a directional wind shear which increases throughout the morning.

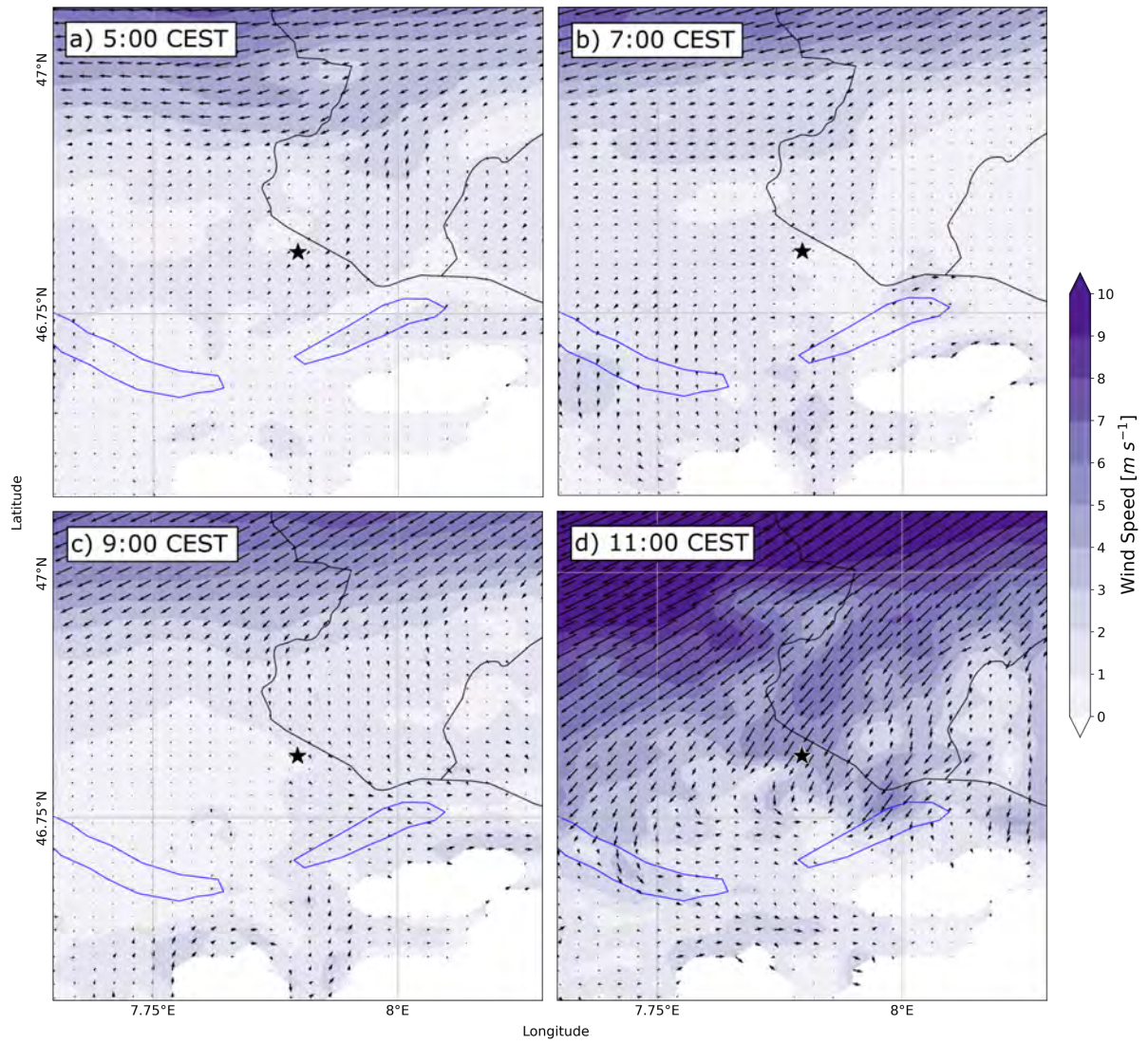


**Figure 28:** Horizontal maps of wind speed [ $ms^{-1}$ ] and direction at 800 hPa. The maps show the winds at 5:00 CEST (a), 7:00 CEST (b), 9:00 CEST (c), and 10:00 CEST (d). The Location of Bumbach is marked with the black star. The blue lines mark the locations of lake Thun and lake Brienz. The black lines demark the cantonal borders.





## 6 | Discussion

This chapter discusses the results of the thesis in relation to the initial research questions. Chapter 6.1 discusses the spatial, temporal, meteorological, and precipitation characteristics of *SCS* over Switzerland and possible explanations for the found distributions. In Chapter 6.2, the case study results are discussed which aimed to answer two research questions. First, about the mesoscale conditions under which stationary thunderstorms occur and second, about the storms' mechanisms to stay stationary.

### 6.1 Discussion Climatology

The overall fraction of *SCS* over Switzerland is low, with only 3.49 % of all cells, the *LTL D* cells are even rarer, with only 1.15 % of all cells. These values are especially low compared to the results found by SODERHOLM et al. (2014) in their case study. With similar definitions of *SCS* and *LTL D*, they found frequencies of 21.5% and 19.2% respectively. However, these fractions result from a study of a single mountain ridge with only 130 analysed storms in total. In this thesis, a larger area with a much more varied topography is analysed, so the difference in results is not too surprising. If the thesis was focused on a smaller region of Switzerland, e.g. the "Engadin" in northeaster Grisons similar frequencies of *SCS* could have been found. The more varied topography leads to a more heterogeneous distribution of *SCS* over Switzerland, which this climatology describes.

#### *Spatial Characteristics*

The *SCS* and *LTL D* frequencies differ for all the investigated subregions. In general, the *SCS* appear most often in mountainous regions while the *LTL D* initiate most frequently west of the Jura and in western Switzerland overall. There are few initiations in the Alps; however, this could also potentially be influenced by issues of the radar measurements in this region (NISI et al. 2016).

The proximity of *SCS* to orography is not surprising since stationary storms depend on it according to the theories by MIGLIETTA and ROTUNNO (2009) and SODERHOLM et al. (2014). The relatively high

number of initiations in the northern part of the Plateau is possibly an effect of the “partial” stationarity definition used, allowing cells to travel, before being stationary. The northerly wind could bring cells initiated in this region to the foothills of the alps relatively quickly. The hotspot west of the Tessin at the border to Switzerland is at the Weissgrat and the Liskamm. This area has very steep altitude gradients with elevation changes from around 1000m up to over 4000m. This gradient, combined with the relatively flat area south-east toward the PO-valley makes it a prime location for SCS. The hotspots at the eastern Grisons border lie at the edges of valleys with a southwestern direction (Engadin, Valtellina). Through these valleys, hot and moist air from the low-lying areas around the Lago die Como could move up until they hit the alpine peaks with over 3000 m of height.

Similar situations present themselves in the regions with high SCS fractions in the south of the alps. Combined with the humidity due to the proximity to the Mediterranean, these regions have similar dispositions to the ones described in the case studies by DUCROCQ et al. (2008). However, an in-depth study of the individual cases would be necessary to describe the phenomena in detail.

The Initiation locations of the *LTLD* cells fit results regarding the wind speed, directions and weather types correlating with that cell type. For a cell to have a long track over Switzerland with westerly to the south-westerly wind, we would expect this distribution. The Alps’ orography influences the cells’ movement, making long tracks less likely and explaining the minimum of *LTLD*. NISI et al. (2018) find similar results for the length of hail streaks.

### ***Temporal Characteristics***

The SCS exhibit a similar interannual distribution as the *OTHER* storms, which means that they on average become more frequent over the 14-year study period. The *LTLD* storm frequency in contrast decreases. However, this is not a trend but merely a tendency. Furthermore, the data shows a rather extreme outlier for the SCS frequency in 2018, which influences this tendency. It is open whether these patterns are due to changes in data quality or meteorological trends. As described in this thesis’s data section, the radar network changed significantly over the study period.

From a meteorological perspective, there is some evidence that interannual synoptic phenomena can influence thunderstorms’ variability. Especially teleconnection patterns and their influence on the convective activity have been analysed in several studies for Europe based on different datasets:

PIPER and KUNZ (2017) use lightning data to investigate the relation to the North Atlantic Oscillation teleconnection pattern (NAO). They find it to have a strong influence on convective activity across

Europe. Over large parts of Europe, a negative NAO phase leads to an increase in thunderstorm activity while a positive NAO leads to a decrease. However, their results are only statistically significant for the south of Switzerland (Valais, Ticino) and the positive NAO phase.

In a later study, PIPER et al. (2019) develop a weather type classification which estimates the thunderstorm probability based on several mesoscale meteorological variables. They apply this classification to high-resolution global reanalysis data between 1958 and 2014. Their results show a strong link between thunderstorm activity, the large-scale flow and properties of the air mass such as stability, moisture and vertical lifting. They investigate the influence of the large-scale flow further by looking at different teleconnection patterns. For northern Switzerland, they find a significant influence of the East Atlantic Pattern (EA). Phases of negative EA ( $<0.5$ ) are related to reduced thunderstorm frequencies while during positive EA ( $>0.5$ ) their frequency increases. The positive EA anomaly is connected to a positive temperature anomaly and a wind anomaly with stronger south-westerly winds over Switzerland. In contrast to the Study by PIPER and KUNZ (2017), they do not find any significant influence of the different NAO phases.

The correlation of *SCS* interannual variability with the *OTHER* storm interannual variability suggests that *SCS* are also favoured by the same large-scale weather patterns. The *LTL*D storms, on the other hand, may be influenced by other factors or weather patterns. A complete analysis of the influence of the mesoscale weather and the teleconnections on the different storm types is out of this thesis's scope, but in a later section of this chapter, I will look at the relations to the GWT and the mid-tropospheric circulation to get a first idea.

The annual distribution of *SCS* differs significantly from the one of *STLD* storms but is similar to the one of the *OTHER* storms. The main difference is an earlier peak in June/July compared to July/August for *STLD*. An explanation of these differences could be the difference in the mesoscale weather situations related to the different storm types.

*SCS* require strong convection and lower wind speeds than *LTL*D storms which influences their monthly distribution due to the changing mesoscale weather situation over Switzerland. Both *SCS* and *LTL*D storms are storms with a longer lifetime than a simple single-cell storm. As explained in the introduction, vertical wind shear can be a key ingredient for these longer-lived storms. While this process is relevant for the *LTL*D storms, it might not be as important in *SCS*. According to the theories for *SCS*, a key factor for the stationarity is the orographic influence on the cold air outflow of storms. Here the orography causes a separation of the inflow and the storm's outflow, which influences

its lifetime. Consequently, wind shear could be less critical for the longevity of *SCS* than for *LTL*D storms.

SCHEMM et al. (2016) find that increased wind shear typically occurs with an approaching cold front. This sheared environment could potentially be conducive to the long-lived *LTL*D cells. During the convective season over Switzerland, cold fronts are most frequent in August and September (JENKNER et al. 2010), explaining the peak *LTL*D storm occurrence in these Months.

The diurnal cycle of *SCS* also differs significantly from other storms. *SCS* initiate more frequently in the late afternoon, especially compared to *LTL*D storms which can also initiate during the night and early morning.

A possible explanation for the differences between *SCS* and *LTL*D storms are the possibly differing triggering mechanisms. The high fraction of *SCS* initiation in the afternoon can indicate triggering through differential heating and local convergence during the time of highest solar radiation (e.g. MARKOWSKI and RICHARDSON 2010). The possible connection of *LTL*D cells to fronts discussed in the previous chapter also could explain the triggering of those cells in the early morning when fronts can pass through.

### ***Mesoscale Characteristics***

To get an idea about the mesoscale weather situation related to the different storm types, the weather types and mid-tropospheric windspeeds are analysed in this thesis. The weather types for *SCS* are significantly different from the other storm types. The same also applies to the wind speed and direction in the mid-troposphere. *STL*D storms are strongly favoured in an environment with westerly to south-westerly winds with higher average velocities than the other cell types. *SCS* storms are most frequent with lower average wind speeds but also with westerly to south-westerly winds. However, especially north of the Alps they also frequently happen in north-western to north-eastern winds.

These regional differences are a possible indication for the mechanisms leading to the stationarity of the *SCS*. The northerly winds for the *SCS* north of the alps are at a more perpendicular angle to the Jura and the Alps' mountain ridges. This fits the cross-barrier theory for *SCS* described by DUCROCQ et al. (2008) and by MIGLIETTA and ROTUNNO (2009). They find that *SCS* are caused by moist winds at lower levels impinging perpendicularly on mountain ridges.

MIGLIETTA and ROTUNNO (2009) also specifically look at the effects of different wind speeds in their model on the cell's stationarity. They find that an *SCS* can form on a simple mountain ridge at different

wind strengths. This thesis found that *SCS* are most frequent at environmental wind speeds of  $5.5 \text{ ms}^{-1}$ . Following Miglietta and Rotunno's results that would indicate that the *SCS* over Switzerland stay stationary due to the cold outflows from the storms that flow downslope of the mountain ridges and trigger continuous convection when clashing with the impinging winds. However, the study by MIGLIETTA and ROTUNNO (2009) is based on a simple model topography compared to the complex topography in the study area. A more in-depth look at the mechanisms leading to the storms in the different subregions is required to see whether the model suits the cases in the study region.

### ***Precipitation Characteristics***

Finally, the precipitation characteristics of the storms are investigated. The *SCS* and *LTL**D* exhibit similar precipitation rates which are significantly higher than those of the *OTHER* storms. This is the case in all subregions with the exception of the southern Prealps where the *LTL**D* are significantly more intense than both other storm types. These results are an indication that for most of Switzerland, the precipitation intensity is not related to the movement of a cell but to its longevity since both *SCS* and *LTL**D* are long-lived thunderstorms.

A possible explanation for the higher intensity of fast-moving storms south of the alps can be found in a study by PANZIERA and GERMANN (2010). They investigate the influence of the mesoscale flow on rainfall intensity and frequency over the Lago Maggiore region. They find that the upstream wind velocity has a large impact on the intensity and frequency of precipitation in this area. Stronger winds lead to higher precipitation rates which fit with the observations regarding *SCS* and *LTL**D* in this thesis.

Further, these high rainfall rates were previously described by BARTON et al. (2020) who find that the summertime 5-min precipitation extremes are on average the strongest and most frequent south of the alps.

Other than the rainfall rates the, rainfall accumulation caused by single cells is of particular interest. Here the effect of the stationarity of the *SCS* becomes visible. In almost all areas of Switzerland *SCS* are responsible for the highest rainfall accumulations by a significant margin. The only exception is again found in the southern Prealps. Here the previously mentioned significantly higher rainfall rates compensate for the lack of stationarity such that there is no significant difference between the accumulation caused by *SCS* and *LTL**D* storm cells.

## 6.2 Discussion Case Study

The WRF model was not able to reproduce the selected stationary thunderstorm in the region of Bumbach, which makes it impossible to investigate the small-scale mechanisms which led to the stationarity of said storm in detail.

It is difficult to ascertain the cause for the model's shortcoming; however, there are some possibilities. The known mechanisms for stationarity introduced in Chapter 2.1 of this thesis depend on the interaction of orography with a low-level flow of moist air. The orography which underlies the WRF model is of a relatively coarse resolution which has the effect that mountain ridges are smoothed, and certain structures such as small valleys disappear. This is the case in the Bumbach case study; the Emme and the Zulg valleys do not appear in the model. Additionally, the Hohgant and the Schratteflue mountain ridges are lower, and their slopes are gentler. SCHNEIDER et al. (2018) specifically test the model terrain's influence on convection in their high-resolution numerical model. They find that modifying the terrain by either flattening or smoothing mountain ridges significantly impacted the initiation of convection as well as on the amount and location of generated precipitation.

Specifically regarding SCS, these differences in the topography can potentially influence the low-level airflows, which affect the stationarity. Additionally, the slope of the mountain ridge influences where the convection's cold air outflow is directed, which is important in some known stationarity mechanisms.

Another possibility for the lack of stationarity could be a possible sensitivity to wind direction in relation to the terrain. The known mechanisms are based on either perpendicular (MIGLIETTA and ROTTUNNO 2009) or parallel wind (SODERHOLM et al. 2014) flows. If the low-level wind direction or the terrain orientation differs from the real situation, the model might not show stationary convection, even if the model's resolution was not a problem.

An indicator that the model resolution might be sufficient are the case studies done by DUCROCQ et al. (2008). They used the French Meso-NH non-hydrostatic mesoscale numerical model at a resolution of 2.5 km, which is coarser than the model resolution used in this thesis, and were able to reproduce the three events they were interested in. However, they did look at three mesoscale convective systems and not individual storm cells.

The lack of stationary convection in the model of the case study makes it impossible to describe the detailed processes which led to the stationarity. Nevertheless, under the assumption that the model

is realistic on larger scales, I can give some insights about the mesoscale environment conducive to stationarity. However, the results do not show any apparent differences to an environment favourable to convection in general.

Of the ingredients necessary for thunderstorm initiation DOSWELL et al. (1996) the availability of low-level moisture is the first which is satisfied on the morning of the 24.07.2014. In Bumbach and the surrounding regions, there is a layer of 80-100% relative humidity up to 5 km height.

However, the second key ingredient, a conditional instability in the atmosphere, is not. Even though there is an inversion of the Theta-E gradient due to a dry-air layer in the mid-troposphere (potential instability), there is barely any CAPE present in the Emme Valley. It only starts to build up later in the morning (ca. 9:00 CEST) due to low-level heating. There is more CAPE available to the south-west of Bumbach where there were also the first storms initiating in the early morning hours. Over Bumbach, the first storm only initiates after the CAPE starts to build up at 9:10 CEST.

These storms all initiate on the slopes of the Hohgant mountain ridge, which is an indication that the triggering mechanism was orographic lifting, especially in combination with the low-level winds. There are weak north-easterly winds near the surface, which increase in strength and turn to a more northerly direction throughout the morning. In the mid-troposphere and further up, westerly winds start out weak and increase until noon. Therefore, the vertical wind profile leads to a directional wind shear that can impact the convective storms' lifetime and help the formation of stationary storms.

The turning and strengthening of the surface wind could potentially be a consequence of alpine pumping (e.g. LUGAUER and WINKLER 2005), a thermally induced wind circulation caused by differential heating over mountainous terrain. This diurnal circulation is caused by a temperature difference between the air in a mountain valley and an adjacent plain (WHITEMAN 1990) In the case study, the north-easterly surface winds are roughly parallel to the Emme valley in the model topography which fits with the alpine pumping theory. The overall low wind velocities ( $<6 \text{ ms}^{-1}$ ) also fit with the climatology results, as stationary thunderstorms on average occur during relatively low mid-tropospheric wind velocities.





## 7 | Conclusions and Outlook

The goal of this master thesis was to study stationary convective storms (*SCS*) over Switzerland. Since there is little research about this type of storms in general and no pre-existing literature about *SCS*, specifically over Switzerland, the first step of the thesis was to identify and characterise stationary storms and determine their relevance for high precipitation accumulations.

From observational data, a 14-year climatology of *SCS* over Switzerland was compiled. From this climatology, the spatial and temporal characteristics of *SCS* were extracted, and the weather situations related to their occurrence were determined.

The first step towards the climatology was to find a definition of stationarity that could be applied to the available data. For this, three different definitions were compared and tested with different thresholds for the used variables. The chosen definition classifies a storm as *SCS* if during its lifetime it exhibits a period of at least 90 minutes where the storms weighted cell centroid moves less than 25 km.

With this definition, overall *SCS* are relatively rare over Switzerland with only 3.49% of all cells fulfilling the *SCS* criteria. However, there are several hotspots, particularly along the pre-alps and the Jura, where up to 38% of all cells were classified as *SCS*.

Temporally, *SCS* differ significantly from long track long duration (*LTLTD*) storms in their diurnal, monthly and interannual behaviour. In comparison to the *OTHER* storms, there are only significant differences regarding the diurnal cycle.

Over the 14-year study period, there was an overall increase of observed *SCS*. However, it is unclear whether this tendency is due to meteorological influences or due to inhomogeneities in the data. *SCS* are the most frequent in the months with the highest solar radiation (June/July); however, there is some regional variation to this with a later peak frequency in the Alps. Furthermore, the *SCS* have a pronounced diurnal cycle with the most frequent occurrences between noon and early evening, which differs significantly from other storm types.

*SCS* are most likely to occur in weather situations with westerly – to southwesterly flow like all other convective storms over Switzerland. However, they can also initiate in weather situations with mid-tropospheric winds with almost any flow direction, which differentiates the *SCS* from *LTL**D* storms. A further aspect that separates the *SCS* is the related mid-tropospheric wind speeds. They are on average, significantly lower than for other storms at  $5.5 \text{ ms}^{-1}$ .

The final characteristic of interest was the precipitation intensity. Both *SCS* and *LTL**D* storms exhibit significantly higher rainfall rates than other storms. However, their rates do not differ from each other in a significant fashion (10.8 vs 11 mm). Where they do differ significantly, however, is the rainfall accumulation. The climatology has shown that the stationarity of the *SCS*, in general, leads to significantly higher rainfall accumulations compared to all other storms.

The observations made during the climatology part allowed for a first characterization of the *SCS* over Switzerland. There remain some uncertainties that are due to the only 14 years of data, and the inhomogeneity of the data due to the changes in the MeteoSwiss radar network.

To further characterise the mechanisms leading to the stationarity of *SCS* in Switzerland and the mesoscale meteorological properties related to them, a case study was conducted. The case study was based on a high-resolution simulation using the WRF numerical model.

Unfortunately, the model could not reproduce the selected early morning storm in the valley near Bumbach, which made the analysis of the mechanisms impossible. Under the assumption that the reason for this failure was not connected to the simulated mesoscale weather situation, the meteorological variables were analysed following the ingredients based approach for convection. It was found that there was a high amount of moisture present in the boundary layer over the study area. There was only little CAPE available near Bumbach, though, there was more in the surrounding areas. There was some convection roughly in the correct location; however, it was relatively weak and short-lived.

Early in the morning, there were weak winds from the surface up to the mid-troposphere, which intensified later. They had a north-easterly direction on the surface and a westerly one in the mid-troposphere, which led to increasing vertical wind shear during the morning. Following the results from the climatology, these weak winds were what would be expected for a *SCS*.

This final section presents some possible further research opportunities opened by this master's thesis. Furthermore, it addresses the limitations that were encountered.

The key limitation of the climatology produced in this thesis is that it is based on a relatively short

time period and inhomogeneous data. Since the required Lagrangian storm track data for earlier times simply does not exist, there is no other solution than to wait until a longer time-series is available. For this reason, the knowledge about *SCS* over Switzerland would benefit from a repetition of the thesis in a couple of years. However, there are also several potential research avenues which are possible on the currently available data:

- *Repetition with the Overlap Stationarity definition*

While comparing the different stationarity definitions, the OS definition was rejected due to the possibility of misclassification of large-fast moving cells as stationary. While this is a misclassification when the focus lies explicitly on slow or stationary storms, it could potentially have a value from an impact perspective. For the impact, it is not the cell's movement that matters specifically, but the precipitation duration and intensity. For this reason, a climatology of storms based on the OS definition could be of interest.

- *Investigation of the connection to Large-Scale Weather Patterns*

In the discussion on the climatology possible links of the convection to large-scale weather patterns such as for example the NAO were mentioned. It would be interesting to investigate whether these patterns could be a potential driver for the differences between *SCS*, *OTHER* and *LTL*D cells in terms of their temporal and spatial characteristics.

- *Investigation of Mountain Ridge Orientation*

The known mechanisms for *SCS* in the literature are based on the interaction between the wind direction, the convection, and mountain ridges. Specifically, situations where the wind impinges perpendicularly on mountain ridges or flows parallel to them lead to stationarity. It should be investigated with the data from this climatology whether the *SCS* only appears when one of these two situations is present. That way, the mechanisms could be verified, or alternative possibilities for stationarity could be found.

- *Small Scale investigations*

The climatology has shown that there are several small regions where *SCS* are particularly frequent. These regions should be investigated in more detail to determine the causes leading to these higher frequencies. Case studies lead to in-depth knowledge which possibly could help with forecasting such events in these locations.

The WRF model was not able to reproduce the *SCS* of interest over Bumbach. From this follow two possible continuations of this thesis; The first option would be to change the numerical model or adapt it in a way such that it can reproduce the *SCS*. The process of adapting the model could lead to detailed knowledge about the processes needed for this *SCS*. However, it is also possible that current numerical models cannot reproduce this specific storm, for example, due to unresolved processes, which makes this approach impractical.

The second option would be to carry out several case studies in other regions to investigate other stationary cells. The regions with high *SCS* frequency identified by the climatology mentioned above would be a great starting point for this process since they seem to be specifically suitable for stationary convection.

# Appendix

## Appendix 1

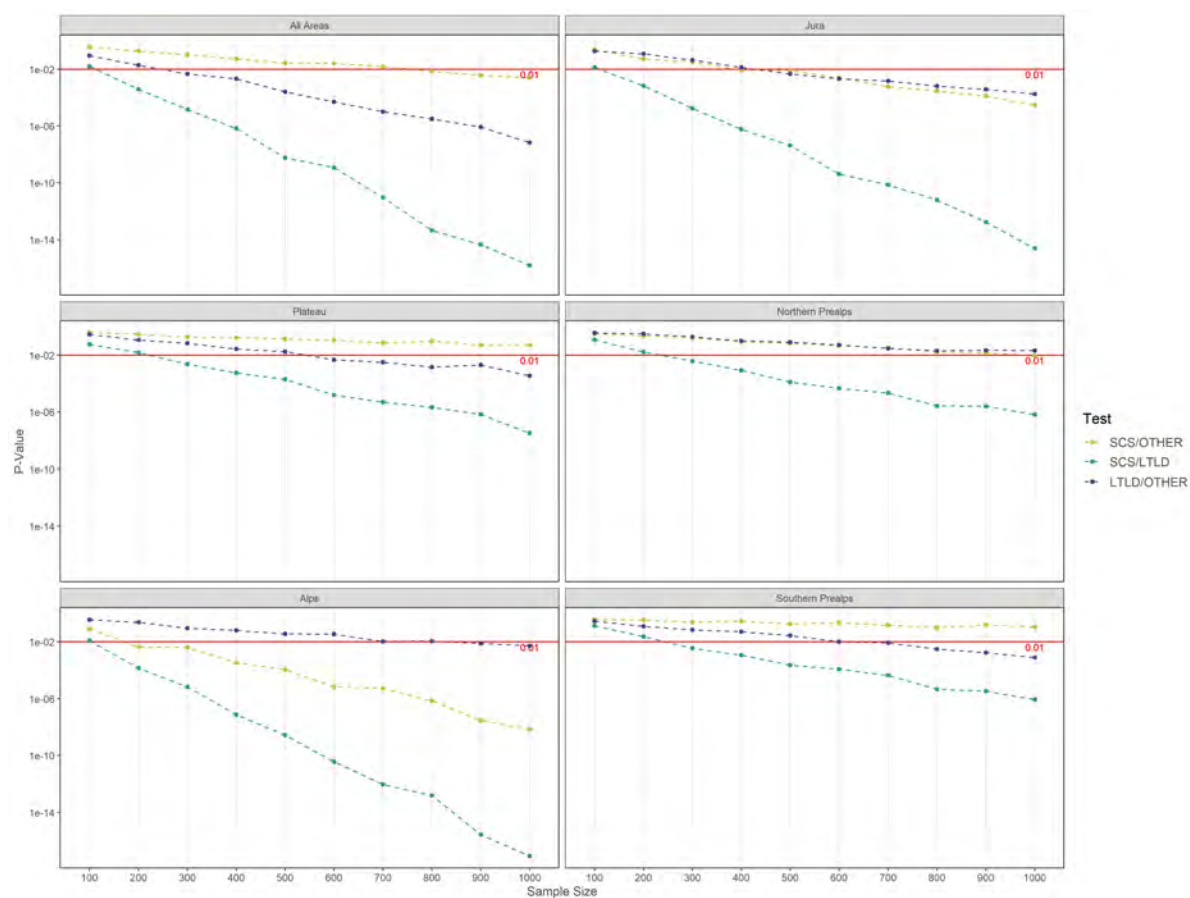


**Figure A.1:** MPS-charts for comparisons of the Interannual distributions of *SCS*, *LTLD* and *OTHER* for all sub-regions. Each of the lines shows the P-Values of one of the three comparisons in relation to sample size on a logarithmic scale. The shown P-Value is the median value of the 100 subsamples taken. The red line denotes the 0.01 significance level.

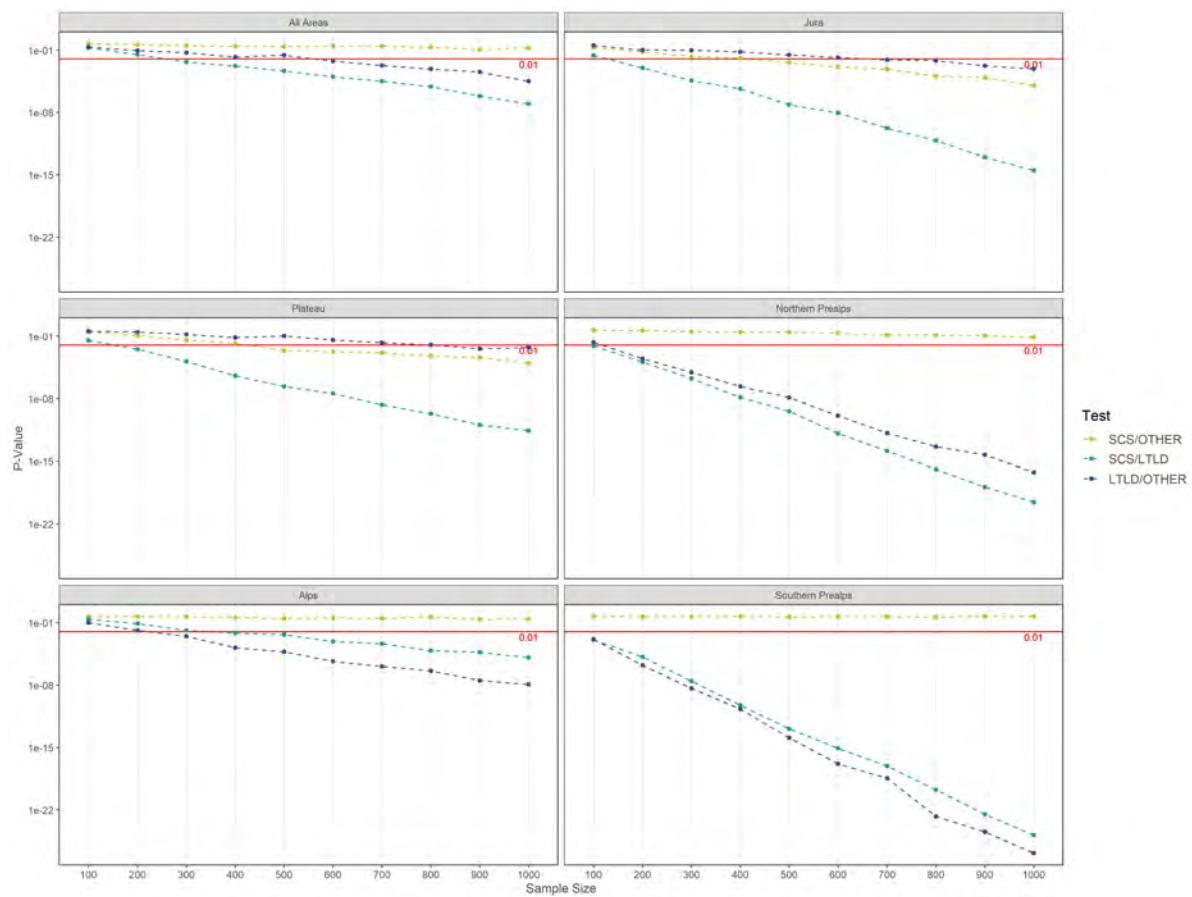


**Figure A.2:** Same as A.1 but for the annual distributions.

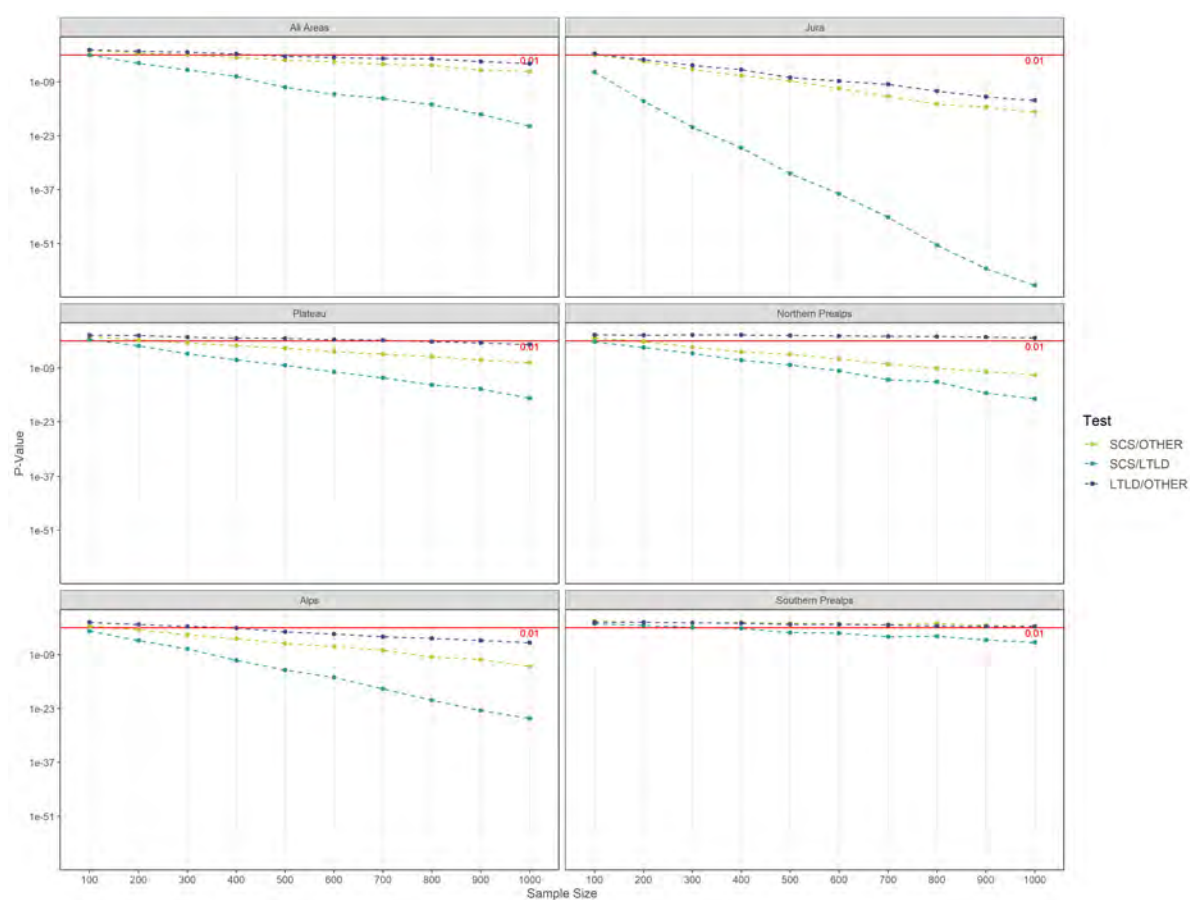


**Figure A.3:** Same as A.1 but for the diurnal distributions.

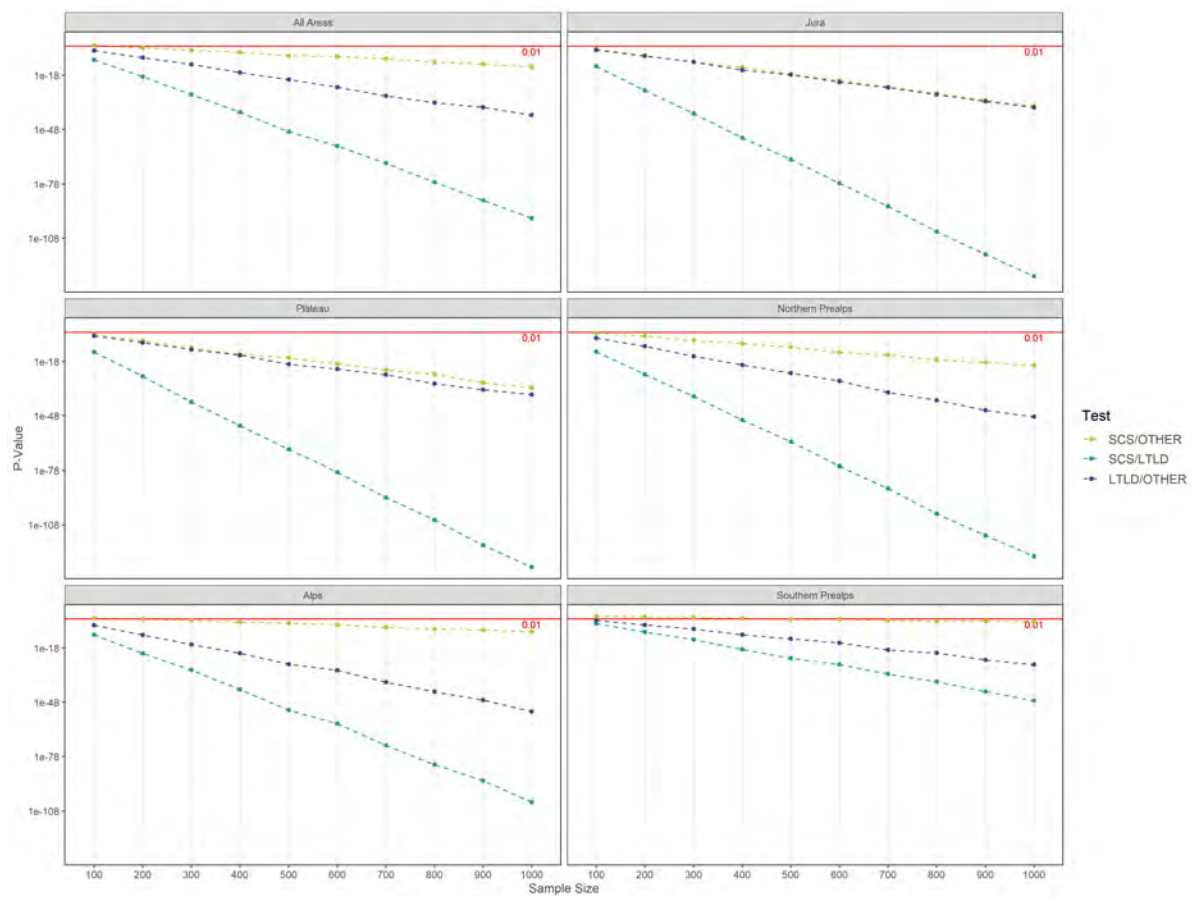


**Figure A.4:** Same as A.1 but for the distributions of the wind direction at 750 hPa.



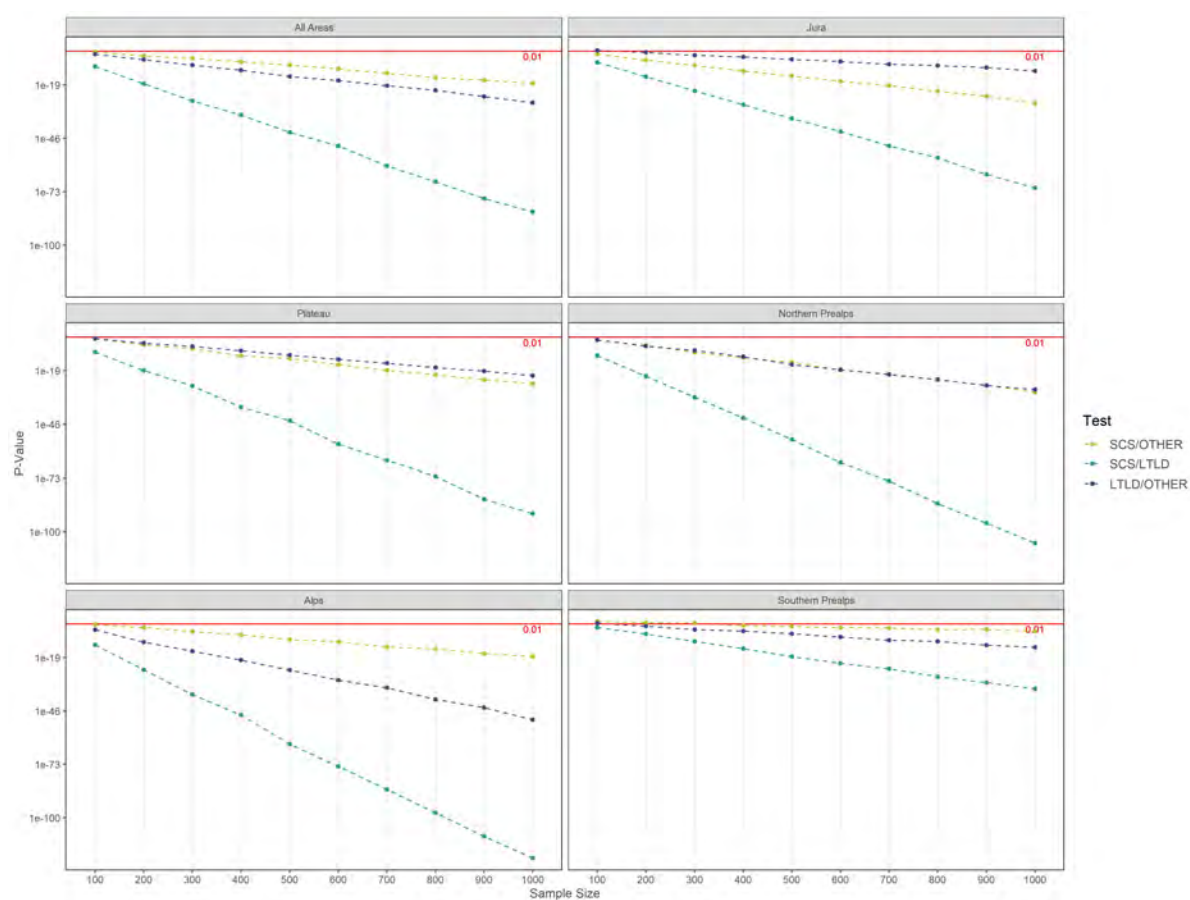


**Figure A.5:** Same as A.1 but for the distributions of the wind speeds at 750 hPa.

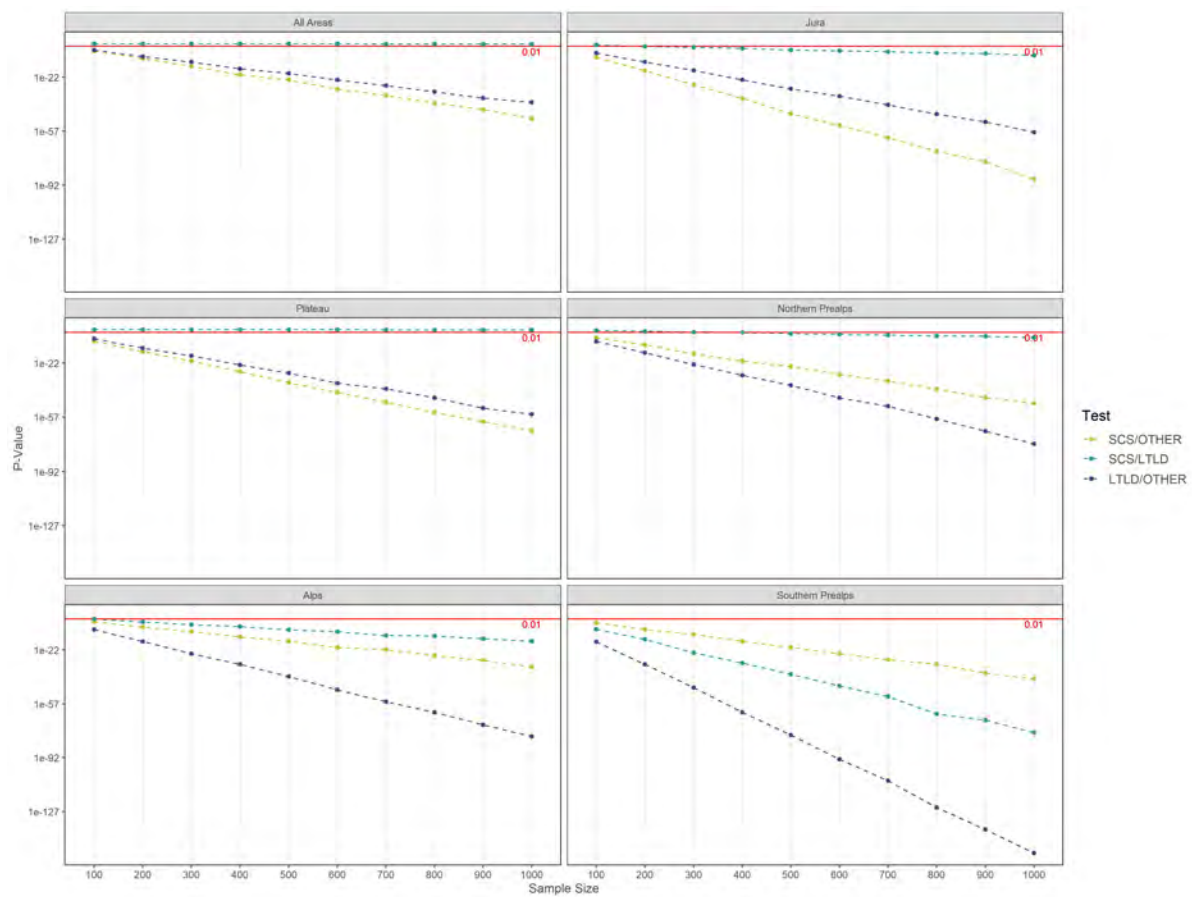


**Figure A.6:** Same as A.1 but for the distributions of the mean rainfall rates.

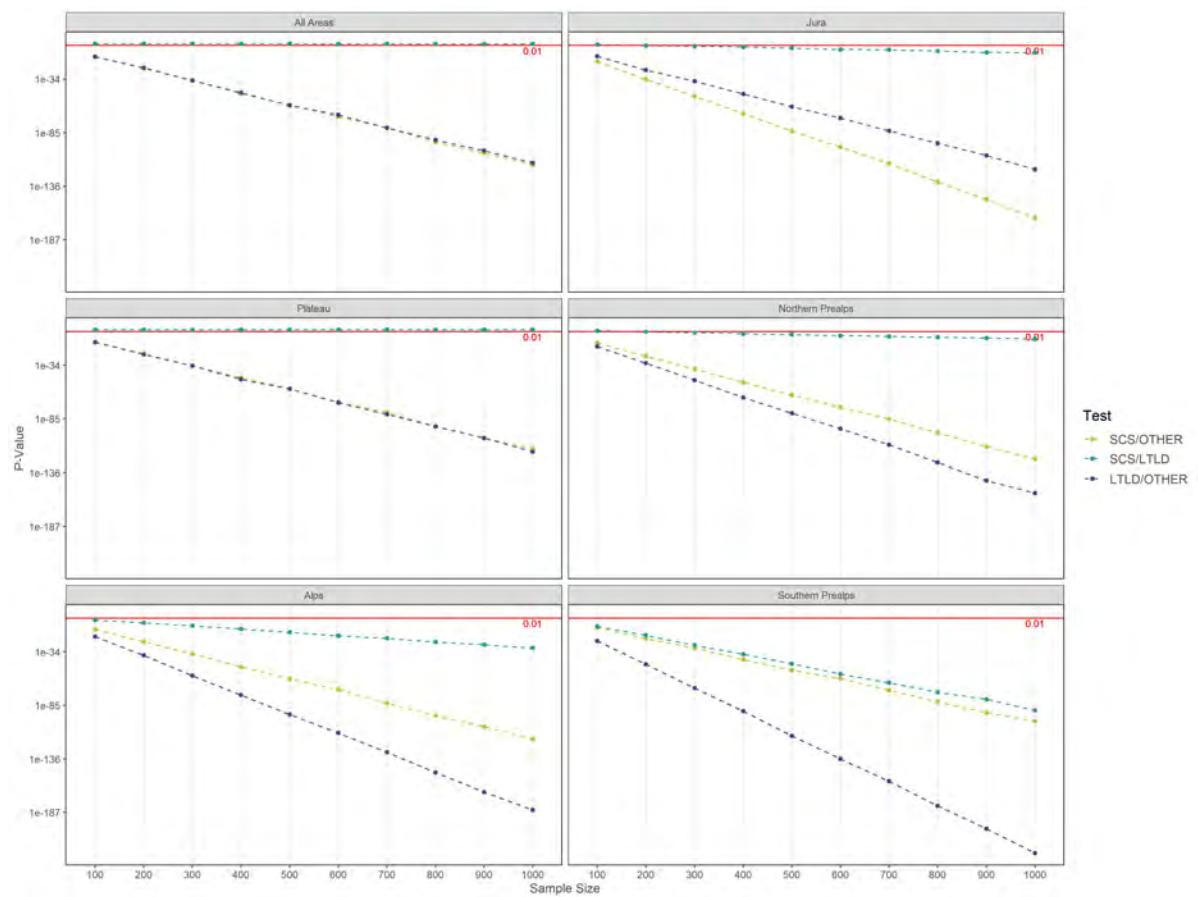


**Figure A.7:** Same as A.1 but for the distributions of the max rainfall rates.

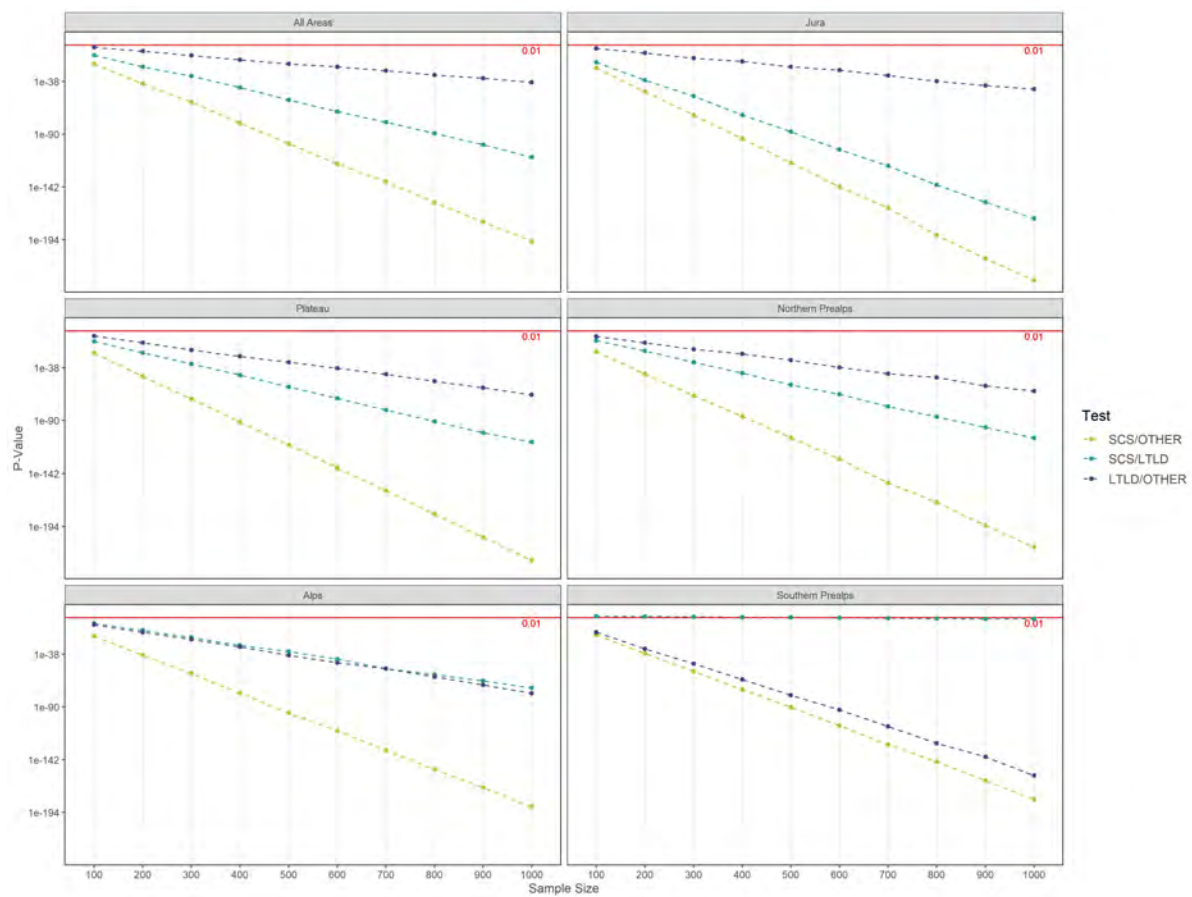


**Figure A.8:** Same as A.1 but for the distributions of the mean precipitation accumulations.

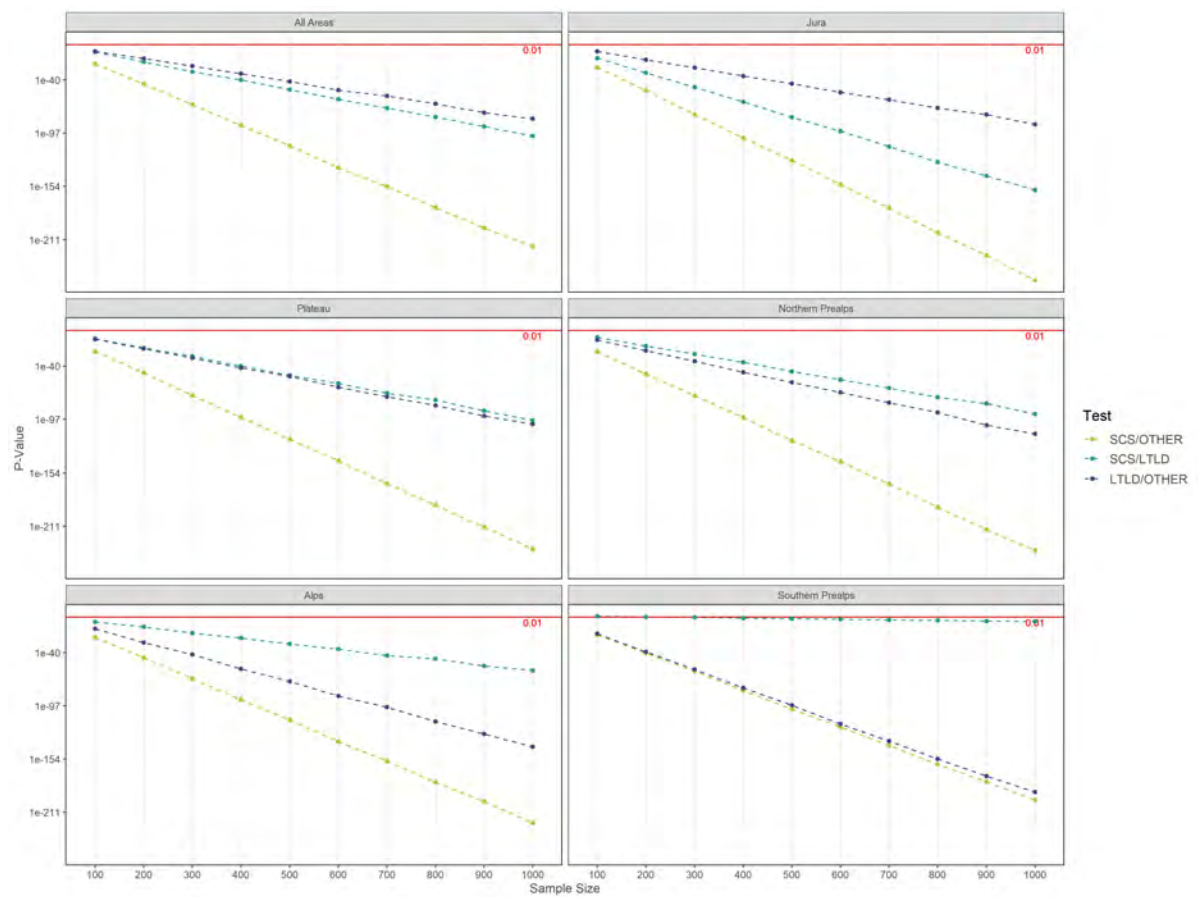


**Figure A.9:** Same as A.1 but for the distributions of the max precipitation accumulations.

Appendix 2

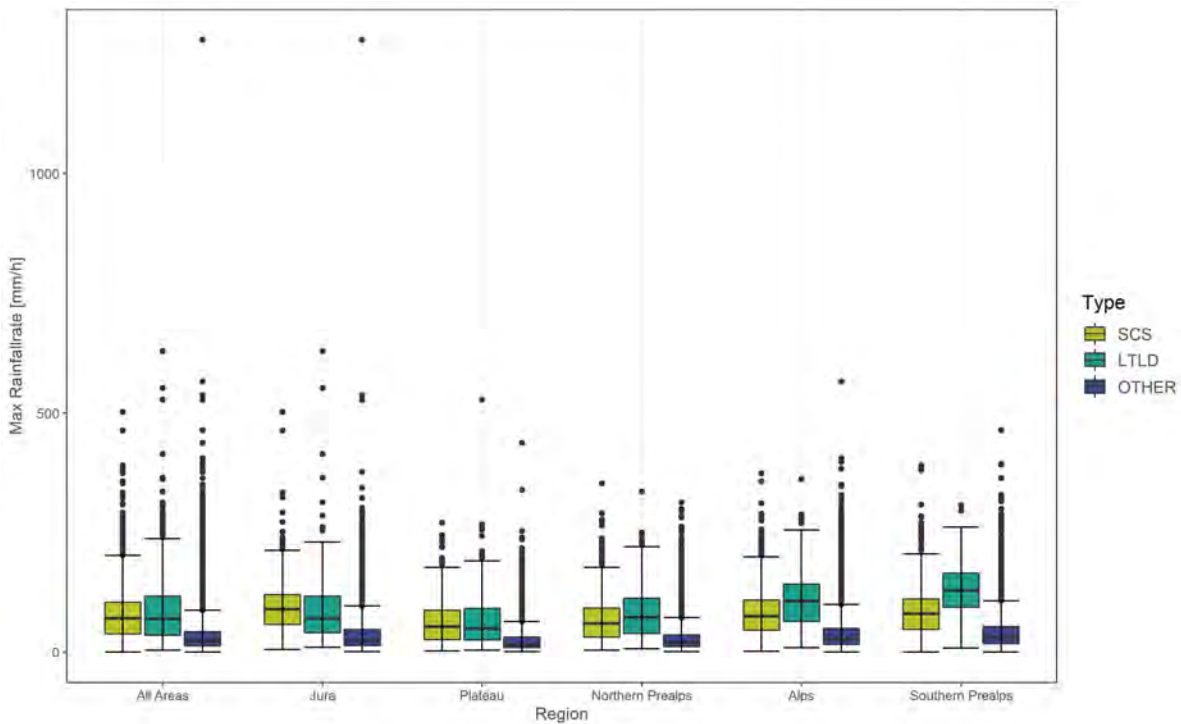


Figure A.10: Max rainfall rate per storm cell for each type and split by subregion.

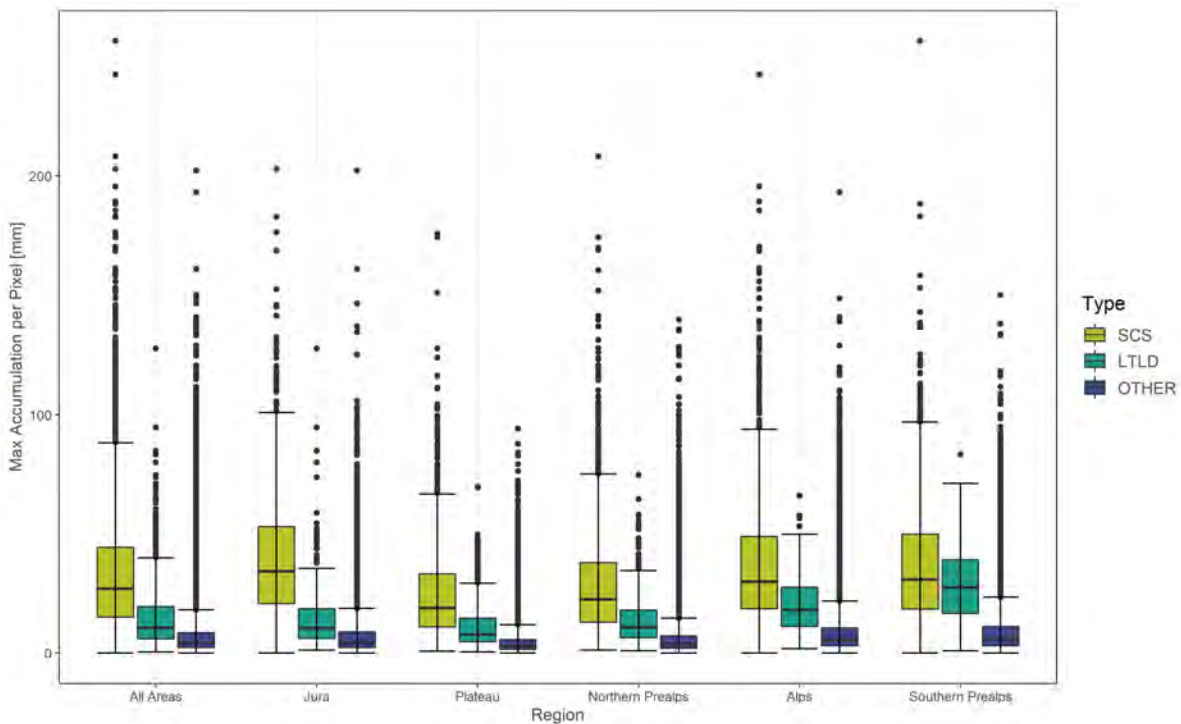


Figure A.11: Max precipitation accumulation per storm cell for each type and split by subregion.

# List of Figures

1	Life cycle of thunderstorms . . . . .	6
2	SCS due to coldpool . . . . .	7
3	Stationarity depending on wind speeds . . . . .	8
4	SCS due to along barrier flow . . . . .	8
5	Study Region . . . . .	14
6	Stationarity Definitions . . . . .	19
7	Example MPS-chart . . . . .	22
8	Location of case study with terrain height . . . . .	25
9	Overlap stationarity example . . . . .	28
10	End-to-End stationarity example . . . . .	29
11	Distance threshold to frequency relation . . . . .	30
12	Annual storm frequency . . . . .	31
13	Stormtype in relation to GWT . . . . .	32
14	Stormtype in relation to 750hPa wind direction . . . . .	33
15	Stormtype in relation to wind speed . . . . .	33
16	Monthly storm frequency . . . . .	34
17	Hourly storm frequency . . . . .	35
18	SCS and <i>LTL</i> D storm initiation locations . . . . .	37

---

19	SCS counts and frequency . . . . .	38
20	Mean rainfall rate by storm type . . . . .	39
21	Mean rainfall accumulation by storm type . . . . .	40
22	SCS frequency in top 100 events . . . . .	41
23	WRF and CPC precipitation accumulations . . . . .	42
24	VCS and temporal evolution of RH . . . . .	43
25	Horizontal maps of CAPE and CIN . . . . .	44
26	Skew T-log p diagrams . . . . .	45
27	VCS and temporal evolution of Theta-E . . . . .	46
28	Horizontal maps of wind speed and direction . . . . .	47



## List of Tables

1	Available Variables . . . . .	15
2	Calculated and added variables . . . . .	21
3	Test Statistics . . . . .	21
4	Storm frequencies by area . . . . .	36



## References

- ANDRES, N. and A. BADOUX (2019). Unwetterschäden in der Schweiz im Jahre 2018. Rutschungen, Murgänge, Hochwasser und Sturzereignisse. *Wasser, Energie, Luft* **111**: 29–38.
- BADOUX, A., N. ANDRES, F. TECHEL, and C. HEGG (2016). Natural hazard fatalities in Switzerland from 1946 to 2015. *Natural Hazards and Earth System Science* **16**: 2747–2768. DOI: 10.5194/nhess-16-2747-2016.
- BARRETT, A. I., C. WELLMANN, A. SEIFERT, C. HOOSE, B. VOGEL, and M. KUNZ (2019). One Step at a Time: How Model Time Step Significantly Affects Convection-Permitting Simulations. *Journal of Advances in Modeling Earth Systems* **11**: 641–658. DOI: 10.1029/2018MS001418.
- BARTON, Y., I. V. SIDERIS, U. GERMANN, and O. MARTIUS (2019). A method for real-time temporal disaggregation of blended radar–rain gauge precipitation fields. *Meteorological Applications*, met.1843. DOI: 10.1002/met.1843.
- BARTON, Y., I. V. SIDERIS, T. H. RAUPACH, M. GABELLA, U. GERMANN, and O. MARTIUS (2020). A multi-year assessment of sub-hourly gridded precipitation for Switzerland based on a blended radar—Rain-gauge dataset. *International Journal of Climatology* **40**: 5208–5222. DOI: <https://doi.org/10.1002/joc.6514>.
- BAUM, R. L. and J. W. GODT (2010). Early warning of rainfall-induced shallow landslides and debris flows in the USA. *Landslides* **7**: 259–272. DOI: 10.1007/s10346-009-0177-0.
- BECH, J. and J. L. CHAU (2012). *Doppler Radar Observations: Weather Radar, Wind Profiler, Ionospheric Radar, and Other Advanced Applications*. Google-Books-ID: 3MWPdWAAQBAJ. BoD – Books on Demand. 486 pages. ISBN: 978-953-51-0496-4.
- BELLON, A. and I. ZAWADZKI (2003). A 9-year summary of radar characteristics of mesocyclonic storms and of deep convection in southern Québec. *Atmosphere-Ocean* **41**: 99–120. DOI: 10.3137/ao.410201.

- BOTZEN, W. J. W., J. C. J. M. VAN DEN BERGH, and L. M. BOUWER (2010). Climate change and increased risk for the insurance sector: a global perspective and an assessment for the Netherlands. *Natural Hazards* **52**: 577–598. DOI: 10.1007/s11069-009-9404-1.
- BRIMELOW, J. C., G. W. REUTER, A. BELLON, and D. HUDAK (2004). A radar-based methodology for preparing a severe thunderstorm climatology in central Alberta. *Atmosphere-Ocean* **42**: 13–22. DOI: 10.3137/ao.420102.
- BUNDESAMT FÜR UMWELT, B. (2015). *Hydrologische Jahrbuch der Schweiz 2014*. UZ-1511-D. Bundesamt für Umwelt, Bern, 36pp.
- BURCEA, S., R. CICA, and R. BOJARIU (2019). Radar-derived convective storms' climatology for the Prut River basin: 2003–2017. *Natural Hazards and Earth System Sciences* **19**: 1305–1318. DOI: <https://doi.org/10.5194/nhess-19-1305-2019>.
- CALLEGARO, A., C. NDOUR, E. ARIS, and C. LEGRAND (2019). A note on tests for relevant differences with extremely large sample sizes. *Biometrical Journal* **61**: 162–165. DOI: <https://doi.org/10.1002/bimj.201800195>.
- CANUTI, P., P. FOCARDI, and C. A. GARZONIO (1985). Correlation between rainfall and landslides. *Bulletin of the International Association of Engineering Geology - Bulletin de l'Association Internationale de Géologie de l'Ingénieur* **32**: 49–54. DOI: 10.1007/BF02594765.
- CARBONE, R. E. and J. D. TUTTLE (2008). Rainfall Occurrence in the U.S. Warm Season: The Diurnal Cycle. *Journal of Climate* **21**: 4132–4146. DOI: 10.1175/2008JCLI2275.1.
- CARBONE, R. E., J. D. TUTTLE, D. A. AHIJEVYCH, and S. B. TRIER (2002). Inferences of Predictability Associated with Warm Season Precipitation Episodes. *Journal of the Atmospheric Sciences* **59**: 2033–2056. DOI: 10.1175/1520-0469(2002)059<2033:IOPAWW>2.0.CO;2.
- CHANGERY, M. J. (1981). *National thunderstorm frequencies for the contiguous United States*. NUREG/CR-2252. National Climatic Center, Asheville, NC (USA); Nuclear Regulatory Commission, Washington, DC (USA). Office of Nuclear Regulatory Research.
- CHANGNON, S. A. (1988). Climatology of Thunder Events in the Conterminous United States. Part I: Temporal Aspects. *Journal of Climate* **1**: 389–398. DOI: 10.1175/1520-0442(1988)001<0389:COTEIT>2.0.CO;2.
- DAVINI, P., R. BECHINI, R. CREMONINI, and C. CASSARDO (2012). Radar-Based Analysis of Convective Storms over Northwestern Italy. *Atmosphere* **3**: 33–58. DOI: 10.3390/atmos3010033.
- DIXON, M. and G. WIENER (1993). TITAN: Thunderstorm Identification, Tracking, Analysis, and Nowcasting—A Radar-based Methodology. *Journal of Atmospheric and Oceanic Technology* **10**: 785–797. DOI: 10.1175/1520-0426(1993)010<0785:TTITAA>2.0.CO;2.

- DOSWELL, C. A. (2001). "Severe Convective Storms—An Overview". *Severe Convective Storms*. Edited by C. A. DOSWELL. Meteorological Monographs. Boston, MA: American Meteorological Society, pages 1–26. ISBN: 978-1-935704-06-5. DOI: 10.1007/978-1-935704-06-5\_1. URL: [https://doi.org/10.1007/978-1-935704-06-5\\_1](https://doi.org/10.1007/978-1-935704-06-5_1).
- DOSWELL, C. A., H. E. BROOKS, and R. A. MADDOX (1996). Flash Flood Forecasting: An Ingredients-Based Methodology. *Weather and Forecasting* **11**: 560–581. DOI: 10.1175/1520-0434(1996)011<0560:FFFAIB>2.0.CO;2.
- DUCROCQ, V., O. NUISSIER, D. RICARD, C. LEBEAUPIN, and T. THOUVENIN (2008). A numerical study of three catastrophic precipitating events over southern France. II: Mesoscale triggering and stationarity factors. *Quarterly Journal of the Royal Meteorological Society* **134**: 131–145. DOI: 10.1002/qj.199.
- ESMUKOV, K. (2020). *GeoPy*, v.2.0.0. URL: <https://geopy.readthedocs.io/en/stable/index.html#> (visited on 01/29/2021).
- FISHER, R. A. (1922). On the Interpretation of  $\chi^2$  from Contingency Tables, and the Calculation of P. *Journal of the Royal Statistical Society* **85**: 87. DOI: 10.2307/2340521.
- FLESCHE, T. K. and G. W. REUTER (2012). WRF Model Simulation of Two Alberta Flooding Events and the Impact of Topography. *Journal of Hydrometeorology* **13**: Publisher: American Meteorological Society Section: Journal of Hydrometeorology, 695–708. DOI: 10.1175/JHM-D-11-035.1.
- FORESTI, L., L. PANZIERA, P. V. MANDAPAKA, U. GERMANN, and A. SEED (2015). Retrieval of analogue radar images for ensemble nowcasting of orographic rainfall. *Meteorological Applications* **22**: 141–155. DOI: <https://doi.org/10.1002/met.1416>.
- FORESTI, L., I. V. SIDERIS, D. NERINI, L. BEUSCH, and U. GERMANN (2019). Using a 10-Year Radar Archive for Nowcasting Precipitation Growth and Decay: A Probabilistic Machine Learning Approach. *Weather and Forecasting* **34**: Publisher: American Meteorological Society Section: Weather and Forecasting, 1547–1569. DOI: 10.1175/WAF-D-18-0206.1.
- GERMANN, U., M. BOSCACCI, M. GABELLA, and M. SARTORI (2015). Peak Performance: Radar design for prediction in the Swiss Alps. *Meteorological Technology International* **April 2015**: 42–45.
- GERMANN, U., J. FIGUERAS, M. GABELLA, A. HERING, I. SIDERIS, and B. CALPINI (2016). Triggering Innovation: The latest MeteoSwiss Alpine weather radar network, Rad4Alp, has already shown a wealth of research and innovation improvements. *Meteorological Technology International* **April 2016**: 62–65.

- GERMANN, U., G. GALLI, M. BOSCACCI, and M. BOLLIGER (2006). Radar precipitation measurement in a mountainous region. *Quarterly Journal of the Royal Meteorological Society* **132**: 1669–1692. DOI: 10.1256/qj.05.190.
- GERMANN, U., D. NERINI, I. SIDERIS, L. FORESTI, A. HERING, and B. CALPINI (2017). Real-Time radar: A new Alpine radar network is having ramifications beyond meteorology, demonstrating the importance and versatility of real-time data. *Meteorological Technology International* **April 2017**: 88–92.
- GOUDENHOOFDT, E. and L. DELOBBE (2013). Statistical Characteristics of Convective Storms in Belgium Derived from Volumetric Weather Radar Observations. *Journal of Applied Meteorology and Climatology* **52**: 918–934. DOI: 10.1175/JAMC-D-12-079.1.
- GUZZETTI, F., S. PERUCCACCI, M. ROSSI, and C. P. STARK (2008). The rainfall intensity–duration control of shallow landslides and debris flows: an update. *Landslides* **5**: 3–17. DOI: 10.1007/s10346-007-0112-1.
- HANDWERKER, J. (2002). Cell tracking with TRACE3D—a new algorithm. *Atmospheric Research* **61**: 15–34. DOI: 10.1016/S0169-8095(01)00100-4.
- HANLEY, K. E., D. J. KIRSHBAUM, S. E. BELCHER, N. M. ROBERTS, and G. LEONCINI (2011). Ensemble predictability of an isolated mountain thunderstorm in a high-resolution model. *Quarterly Journal of the Royal Meteorological Society* **137**: 2124–2137. DOI: 10.1002/qj.877.
- HARRIS, C. R., K. J. MILLMAN, S. J. VAN DER WALT, R. GOMMERS, P. VIRTANEN, D. COURNAPEAU, E. WIESER, J. TAYLOR, S. BERG, N. J. SMITH, R. KERN, M. PICUS, S. HOYER, M. H. VAN KERKWIJK, M. BRETT, A. HALDANE, J. F. DEL R'IO, M. WIEBE, P. PETERSON, P. G'ERARD-MARCHANT, K. SHEPPARD, T. REDDY, W. WECKESSER, H. ABBASI, C. GOHLKE, and T. E. OLIPHANT (2020). Array programming with NumPy. *Nature* **585**: 357–362. DOI: 10.1038/s41586-020-2649-2.
- HERING, A., C. MOREL, G. GALLI, S. SENESI, P. AMBROSETTI, and M. BOSCACCI (2004). Nowcasting thunderstorms in the Alpine region using a radar based adaptive thresholding scheme.
- HERING, A. M., U. GERMANN, M. BOSCACCI, and S. SÉNÉSI (2008). Operational nowcasting of thunderstorms in the Alps during MAP D-PHASE, 6.
- HERSBACH, H., B. BELL, P. BERRISFORD, S. HIRAHARA, A. HORÁNYI, J. MUÑOZ-SABATER, J. NICOLAS, C. PEUBEY, R. RADU, D. SCHEPERS, A. SIMMONS, C. SOCI, S. ABDALLA, X. ABELLAN, G. BALSAMO, P. BECHTOLD, G. BIAVATI, J. BIDLOT, M. BONAVITA, G. DE CHIARA, P. DAHLGREN, D. DEE, M. DIAMANTAKIS, R. DRAGANI, J. FLEMMING, R. FORBES, M. FUENTES, A. GEER, L. HAIMBERGER, S. HEALY, R. J. HOGAN, E. HÓLM, M. JANISKOVÁ, S. KEELEY, P.

- LALOYAUX, P. LOPEZ, C. LUPU, G. RADNOTI, P. DE ROSNAY, I. ROZUM, F. VAMBORG, S. VILLAUME, and J. N. THÉPAUT (2020). The ERA5 global reanalysis. *Quarterly Journal of the Royal Meteorological Society*, 1–51. DOI: 10.1002/qj.3803.
- HILKER, N., A. BADOUX, and C. HEGG (2009). The Swiss flood and landslide damage database 1972–2007. *Natural Hazards and Earth System Sciences* **9**: 913–925. DOI: <https://doi.org/10.5194/nhess-9-913-2009>.
- HOCKER, J. E. and J. B. BASARA (2008). A 10-year spatial climatology of squall line storms across Oklahoma. *International Journal of Climatology* **28**: 765–775. DOI: 10.1002/joc.1579.
- HOUZE, R. A., W. SCHMID, R. G. FOVELL, and H.-H. SCHIESSER (1993). Hailstorms in Switzerland: Left Movers, Right Movers, and False Hooks. *Monthly Weather Review* **121**: 3345–3370. DOI: 10.1175/1520-0493(1993)121<3345:HISLMR>2.0.CO;2.
- HUANG, Y., Z. MENG, J. LI, W. LI, L. BAI, M. ZHANG, and X. WANG (2017). Distribution and Variability of Satellite-Derived Signals of Isolated Convection Initiation Events Over Central Eastern China: Geo-Based CI Distribution and Variation. *Journal of Geophysical Research: Atmospheres* **122**: 11, 357–11, 373. DOI: 10.1002/2017JD026946.
- JENKNER, J., M. SPRENGER, I. SCHWENK, C. SCHWIERZ, S. DIERER, and D. LEUENBERGER (2010). Detection and climatology of fronts in a high-resolution model reanalysis over the Alps. *Meteorological Applications* **17**: 1–18. DOI: <https://doi.org/10.1002/met.142>.
- JOHNSON, J. T., P. L. MACKEEN, A. WITT, E. D. W. MITCHELL, G. J. STUMPF, M. D. EILTS, and K. W. THOMAS (1998). The Storm Cell Identification and Tracking Algorithm: An Enhanced WSR-88D Algorithm. *Weather and Forecasting* **13**: 263–276. DOI: 10.1175/1520-0434(1998)013<0263:TSCIAT>2.0.CO;2.
- JOSS, J., B. SCHÄDLER, G. GALLI, R. CAVALLI, M. BOSCACCI, E. HELD, G. D. BRUNA, G. KAPPENBERGER, V. NESPOR, and R. SPIESS (1998). Operational Use of Radar for Precipitation. Publisher: MeteoSwiss, 122.
- KARNEY, C. F. F. (2013). Algorithms for geodesics. *Journal of Geodesy* **87**: 43–55. DOI: 10.1007/s00190-012-0578-z.
- KIRSHBAUM, D., B. ADLER, N. KALTHOFF, C. BARTHLOTT, and S. SERAFIN (2018). Moist Orographic Convection: Physical Mechanisms and Links to Surface-Exchange Processes. *Atmosphere* **9**: 80. DOI: 10.3390/atmos9030080.
- LI, P. W. and E. S. T. LAI (2004). Short-range quantitative precipitation forecasting in Hong Kong. *Journal of Hydrology. Quantitative Precipitation Forecasting II* **288**: 189–209. DOI: 10.1016/j.jhydrol.2003.11.034.

- LIECHTI, K., L. PANZIERA, U. GERMANN, and M. ZAPPA (2013). The potential of radar-based ensemble forecasts for flash-flood early warning in the southern Swiss Alps. *Hydrology and Earth System Sciences* **17**: 3853–3869. DOI: 10.5194/hess-17-3853-2013.
- LIN, M., H. LUCAS, and G. SHMUELI (2013). Too Big to Fail: Large Samples and the p-Value Problem. *Information Systems Research* **24**: 906–917. DOI: 10.1287/isre.2013.0480.
- LOHMANN, U., F. LÜÖND, and F. MAHRT (2016). *An Introduction to Clouds: From the Microscale to Climate*. Google-Books-ID: KR1CDAAAQBAJ. Cambridge University Press. 419 pages. ISBN: 978-1-107-01822-8.
- LOMBARDO, K. A. and B. A. COLLE (2010). The Spatial and Temporal Distribution of Organized Convective Structures over the Northeast and Their Ambient Conditions. *Monthly Weather Review* **138**: 4456–4474. DOI: 10.1175/2010MWR3463.1.
- LÓPEZ, R. E., D. O. BLANCHARD, D. ROSENFELD, W. L. HISCOX, and M. J. CASEY (1984). Population Characteristics, Development Processes and Structure of Radar Echoes in South Florida. *Monthly Weather Review* **112**: 56–75. DOI: 10.1175/1520-0493(1984)112<0056:PCDPAS>2.0.CO;2.
- LUGAUER, M. and P. WINKLER (2005). Thermal circulation in South Bavaria climatology and synoptic aspects. *Meteorologische Zeitschrift*. Publisher: Schweizerbart'sche Verlagsbuchhandlung, 15–30. DOI: 10.1127/0941-2948/2005/0014-0015.
- LUKACH, M., L. FORESTI, O. GIOT, and L. DELOBBE (2017). Estimating the occurrence and severity of hail based on 10 years of observations from weather radar in Belgium: Estimating radar-based occurrence and severity of hail in Belgium. *Meteorological Applications* **24**: 250–259. DOI: 10.1002/met.1623.
- MADDOX, R. A., L. R. HOXIT, C. F. CHAPPELL, and F. CARACENA (1978). Comparison of Meteorological Aspects of the Big Thompson and Rapid City Flash Floods. *Monthly Weather Review* **106**: 375–389. DOI: 10.1175/1520-0493(1978)106<0375:COMAOT>2.0.CO;2.
- MÄKELÄ, A., P. ROSSI, and D. M. SCHULTZ (2010). The Daily Cloud-to-Ground Lightning Flash Density in the Contiguous United States and Finland. *Monthly Weather Review* **139**: 1323–1337. DOI: 10.1175/2010MWR3517.1.
- MANN, H. B. and D. R. WHITNEY (1947). On a Test of Whether one of Two Random Variables is Stochastically Larger than the Other. *Annals of Mathematical Statistics* **18**: Publisher: Institute of Mathematical Statistics, 50–60. DOI: 10.1214/aoms/1177730491.



- MARKOWSKI, P. and Y. RICHARDSON (2010). *Mesoscale Meteorology in Midlatitudes*. John Wiley and Sons. ISBN: 978-0-470-74213-6. DOI: 10.1002/9780470682104. URL: <https://pennstate.pure.elsevier.com/en/publications/mesoscale-meteorology-in-midlatitudes>.
- MAY, P. T. and A. BALLINGER (2007). The Statistical Characteristics of Convective Cells in a Monsoon Regime (Darwin, Northern Australia). *Monthly Weather Review* **135**: 82–92. DOI: 10.1175/MWR3273.1.
- MIGLIETTA, M. M. and R. ROTUNNO (2009). Numerical Simulations of Conditionally Unstable Flows over a Mountain Ridge. *Journal of the Atmospheric Sciences* **66**: 1865–1885. DOI: 10.1175/2009JAS2902.1.
- MILBRANDT, J. A. and H. MORRISON (2016). Parameterization of Cloud Microphysics Based on the Prediction of Bulk Ice Particle Properties. Part III: Introduction of Multiple Free Categories. *Journal of the Atmospheric Sciences* **73**: Publisher: American Meteorological Society Section: Journal of the Atmospheric Sciences, 975–995. DOI: 10.1175/JAS-D-15-0204.1.
- MOHEE, F. M. and C. MILLER (2010). Climatology of Thunderstorms for North Dakota, 2002–06. *Journal of Applied Meteorology and Climatology* **49**: 1881–1890. DOI: 10.1175/2010JAMC2400.1.
- MOREL, C. and S. SENESI (2002). A climatology of mesoscale convective systems over Europe using satellite infrared imagery. I: Methodology. *Quarterly Journal of the Royal Meteorological Society* **128**: 1953–1971. DOI: 10.1256/003590002320603485.
- MOREL, C., S. SÉNÉSI, and F. AUTONES (2002). Building upon SAF-NWC products: Use of the Rapid Developing Thunderstorms (RDT) product in Météo-France nowcasting tools. *The 2002 Meteorological Satellite Data Users' Conference*, 248–255.
- MOREL, C., S. SÉNÉSI, F. AUTONES, and L. LABATUT (2000). The Rapid Developing Thunderstorms (RDT) product of the nowcasting SAF. Prototyping activities and quality assessment using GOES images. *The 2000 Meteorological Satellite Data Users' Conference*, 698–705.
- NGA, N. G.-I. A. (2014). *Department of Defense World Geodetic System 1984, Its Definition and Relationships with Local Geodetic Systems*, 207pp.
- NISI, L., A. HERING, U. GERMANN, and O. MARTIUS (2018). A 15-year hail streak climatology for the Alpine region. *Quarterly Journal of the Royal Meteorological Society* **144**: 1429–1449. DOI: 10.1002/qj.3286.
- NISI, L., O. MARTIUS, A. HERING, M. KUNZ, and U. GERMANN (2016). Spatial and temporal distribution of hailstorms in the Alpine region: a long-term, high resolution, radar-based analysis: Spatial and Temporal Distribution of Hailstorms in the Alpine Region. *Quarterly Journal of the Royal Meteorological Society* **142**: 1590–1604. DOI: 10.1002/qj.2771.

- NIYOGI, D., P. PYLE, M. LEI, S. P. ARYA, C. M. KISHTAWAL, M. SHEPHERD, F. CHEN, and B. WOLFE (2010). Urban Modification of Thunderstorms: An Observational Storm Climatology and Model Case Study for the Indianapolis Urban Region. *Journal of Applied Meteorology and Climatology* **50**: 1129–1144. DOI: 10.1175/2010JAMC1836.1.
- NOVO, S., D. MARTÍNEZ, and O. PUENTES (2014). Tracking, analysis, and nowcasting of Cuban convective cells as seen by radar: Cuban convective cells as seen by radar. *Meteorological Applications* **21**: 585–595. DOI: 10.1002/met.1380.
- NYDEGGER, E. (2015). Sechs Monate Danach - Schangnau. *Coopzeitung*, 10.
- OSANAI, N., T. SHIMIZU, K. KURAMOTO, S. KOJIMA, and T. NORO (2010). Japanese early-warning for debris flows and slope failures using rainfall indices with Radial Basis Function Network. *Landslides* **7**: 325–338. DOI: 10.1007/s10346-010-0229-5.
- OVEREEM, A., I. HOLLEMAN, and A. BUISHAND (2009). Derivation of a 10-Year Radar-Based Climatology of Rainfall. *Journal of Applied Meteorology and Climatology* **48**: 1448–1463. DOI: 10.1175/2009JAMC1954.1.
- PANZIERA, L. and U. GERMANN (2010). The relation between airflow and orographic precipitation on the southern side of the Alps as revealed by weather radar. *Quarterly Journal of the Royal Meteorological Society* **136**: 222–238. DOI: <https://doi.org/10.1002/qj.544>.
- PANZIERA, L., M. GABELLA, S. ZANINI, A. HERING, U. GERMANN, A. BERNE, and L. MONTI (2016). A radar-based regional extreme rainfall analysis to derive the thresholds for a novel automatic alert system in Switzerland. *Hydrol. Earth Syst. Sci.*, 16.
- PETER, J. R., M. J. MANTON, R. J. POTTS, P. T. MAY, S. M. COLLIS, and L. WILSON (2015). Radar-Derived Statistics of Convective Storms in Southeast Queensland. *Journal of Applied Meteorology and Climatology* **54**: 1985–2008. DOI: 10.1175/JAMC-D-13-0347.1.
- PIPER, D. A., M. KUNZ, J. T. ALLEN, and S. MOHR (2019). Investigation of the temporal variability of thunderstorms in central and western Europe and the relation to large-scale flow and teleconnection patterns. *Quarterly Journal of the Royal Meteorological Society* **145**: 3644–3666. DOI: 10.1002/qj.3647.
- PIPER, D. and M. KUNZ (2017). Spatiotemporal variability of lightning activity in Europe and the relation to the North Atlantic Oscillation teleconnection pattern. *Natural Hazards and Earth System Sciences* **17**: Publisher: Copernicus GmbH, 1319–1336. DOI: <https://doi.org/10.5194/nhess-17-1319-2017>. (Visited on 02/02/2021).

- POELMAN, D. R. (2014). A 10-Year Study on the Characteristics of Thunderstorms in Belgium Based on Cloud-to-Ground Lightning Data. *Monthly Weather Review* **142**: 4839–4849. DOI: 10.1175/MWR-D-14-00202.1.
- POTTS, R. J., T. D. KEENAN, and P. T. MAY (2000). Radar Characteristics of Storms in the Sydney Area. *Monthly Weather Review* **128**: 3308–3319. DOI: 10.1175/1520-0493(2000)128<3308:RCOSIT>2.0.CO;2.
- POWERS, J. G., J. B. KLEMP, W. C. SKAMAROCK, C. A. DAVIS, J. DUDHIA, D. O. GILL, J. L. COEN, D. J. GOCHIS, R. AHMADOV, S. E. PECKHAM, G. A. GRELL, J. MICHALAKES, S. TRAHAN, S. G. BENJAMIN, C. R. ALEXANDER, G. J. DIMEGO, W. WANG, C. S. SCHWARTZ, G. S. ROMINE, Z. LIU, C. SNYDER, F. CHEN, M. J. BARLAGE, W. YU, and M. G. DUDA (2017). The Weather Research and Forecasting Model: Overview, System Efforts, and Future Directions. *Bulletin of the American Meteorological Society* **98**: Publisher: American Meteorological Society Section: Bulletin of the American Meteorological Society, 1717–1737. DOI: 10.1175/BAMS-D-15-00308.1.
- ROMANG, H., M. ZAPPA, N. HILKER, M. GERBER, F. DUFOUR, V. FREDE, D. BÉROD, M. OPLATKA, C. HEGG, and J. RHYNER (2011). IFKIS-Hydro: an early warning and information system for floods and debris flows. *Natural Hazards* **56**: 509–527. DOI: 10.1007/s11069-010-9507-8.
- ROTACH, M. W., P. AMBROSETTI, F. AMENT, C. APPENZELLER, M. ARPAGAU, H.-S. BAUER, A. BEHRENDT, F. BOUTTIER, A. BUZZI, M. CORAZZA, S. DAVOLIO, M. DENHARD, M. DORNINGER, L. FONTANNAZ, J. FRICK, F. FUNDEL, U. GERMANN, T. GORGAS, C. HEGG, A. HERING, C. KEIL, M. A. LINIGER, C. MARSIGLI, R. MCTAGGART-COWAN, A. MONTAINI, K. MYLNE, R. RANZI, E. RICHARD, A. ROSSA, D. SANTOS-MUÑOZ, C. SCHÄR, Y. SEITY, M. STAUDINGER, M. STOLL, H. VOLKERT, A. WALSER, Y. WANG, J. WERHAHN, V. WULFMAYER, and M. ZAPPA (2009). MAP D-PHASE: Real-Time Demonstration of Weather Forecast Quality in the Alpine Region. *Bulletin of the American Meteorological Society* **90**: 1321–1336. DOI: 10.1175/2009BAMS2776.1.
- RUIZ-VILLANUEVA, V., N. GALATIOTTO, L. BÜRKLI, and M. STOFFEL (2017). Understanding triggers and dynamics of wood-laden flash floods in mountain catchments: examples from the Zulg River (Switzerland). *19th EGU General Assembly, EGU2017, proceedings from the conference held 23-28 April 2017*, 16792.
- SAXEN, T. R., C. K. MUELLER, T. T. WARNER, M. STEINER, E. E. ELLISON, E. W. HATFIELD, T. L. BETANCOURT, S. M. DETTLING, and N. A. OIEN (2008). The Operational Mesogamma-Scale Analysis and Forecast System of the U.S. Army Test and Evaluation Command. Part IV: The

- White Sands Missile Range Auto-Nowcast System. *Journal of Applied Meteorology and Climatology* **47**: 1123–1139. DOI: 10.1175/2007JAMC1656.1.
- SCHEMM, S., L. NISI, A. MARTINOV, D. LEUENBERGER, and O. MARTIUS (2016). On the link between cold fronts and hail in Switzerland. *Atmospheric Science Letters* **17**: 315–325. DOI: 10.1002/asl.660.
- SCHNEIDER, L., C. BARTHLOTT, A. I. BARRETT, and C. HOOSE (2018). The precipitation response to variable terrain forcing over low mountain ranges in different weather regimes. *Quarterly Journal of the Royal Meteorological Society* **144**: 970–989. DOI: 10.1002/qj.3250.
- SCHUMACHER, R. S. and R. H. JOHNSON (2008). Mesoscale Processes Contributing to Extreme Rainfall in a Midlatitude Warm-Season Flash Flood. *Monthly Weather Review* **136**: 3964–3986. DOI: 10.1175/2008MWR2471.1.
- SCHWARTZ, C. S., G. S. ROMINE, R. A. SOBASH, K. R. FOSSELL, and M. L. WEISMAN (2018). NCAR's Real-Time Convection-Allowing Ensemble Project. *Bulletin of the American Meteorological Society* **100**: 321–343. DOI: 10.1175/BAMS-D-17-0297.1.
- SIDERIS, I. V., M. GABELLA, R. ERDIN, and U. GERMANN (2014). Real-time radar–rain-gauge merging using spatio-temporal co-kriging with external drift in the alpine terrain of Switzerland. *Quarterly Journal of the Royal Meteorological Society* **140**: 1097–1111. DOI: 10.1002/qj.2188.
- SKAMAROCK, C., B. KLEMP, J. DUDHIA, O. GILL, Z. LIU, J. BERNER, W. WANG, G. POWERS, G. DUDA, D. BARKER, and X.-Y. HUANG (2019). A Description of the Advanced Research WRF Model Version 4. DOI: 10.5065/1dfh-6p97.
- SODERHOLM, B., B. RONALDS, and D. J. KIRSHBAUM (2014). The Evolution of Convective Storms Initiated by an Isolated Mountain Ridge. *Monthly Weather Review* **142**: 1430–1451. DOI: 10.1175/MWR-D-13-00280.1.
- SPIRIDONOV, V., Z. DIMITROVSKI, and M. CURIC (2010). *A Three-Dimensional Simulation of Supercell Convective Storm*. Advances in Meteorology. DOI: 10.1155/2010/234731. URL: <https://www.hindawi.com/journals/amete/2010/234731/abs/>.
- STURMARCHIV, S. (2021). *20140724 01 Flood Bumbach BE*. URL: [https://www.sturmarchiv.ch/index.php?title=20140724\\_01\\_Flood\\_Bumbach\\_BE](https://www.sturmarchiv.ch/index.php?title=20140724_01_Flood_Bumbach_BE) (visited on 01/29/2021).
- TREFALT, S., A. MARTYNOV, H. BARRAS, N. BESIC, A. M. HERING, S. LENGGENHAGER, P. NOTI, M. RÖTHLISBERGER, S. SCHEMM, U. GERMANN, and O. MARTIUS (2018). A severe hail storm in complex topography in Switzerland - Observations and processes. *Atmospheric Research* **209**: 76–94. DOI: 10.1016/j.atmosres.2018.03.007.

- TUTTLE, J. D., R. E. CARBONE, and P. A. ARKIN (2008). Comparison of Ground-Based Radar and Geosynchronous Satellite Climatologies of Warm-Season Precipitation over the United States. *Journal of Applied Meteorology and Climatology* **47**: 3264–3270. DOI: 10.1175/2008JAMC2000.1.
- UTSAV, B., S. M. DESHPANDE, S. K. DAS, and G. PANDITHURAI (2017). Statistical Characteristics of Convective Clouds over the Western Ghats Derived from Weather Radar Observations. *Journal of Geophysical Research: Atmospheres* **122**: 10, 050–10, 076. DOI: 10.1002/2016JD026183.
- VILLARINI, G., P. V. MANDAPAKA, W. F. KRAJEWSKI, and R. J. MOORE (2008). Rainfall and sampling uncertainties: A rain gauge perspective. *Journal of Geophysical Research* **113**: ((D11)), D11102. DOI: 10.1029/2007JD009214.
- WAGNER, A., D. HEINZELLER, S. WAGNER, T. RUMMLER, and H. KUNSTMANN (2018). Explicit Convection and Scale-Aware Cumulus Parameterizations: High-Resolution Simulations over Areas of Different Topography in Germany. *Monthly Weather Review* **146**: Publisher: American Meteorological Society Section: Monthly Weather Review, 1925–1944. DOI: 10.1175/MWR-D-17-0238.1.
- WAPLER, K. (2013). High-resolution climatology of lightning characteristics within Central Europe. *Meteorology and Atmospheric Physics* **122**: 175–184. DOI: 10.1007/s00703-013-0285-1.
- WECKWERTH, T. M., J. W. WILSON, M. HAGEN, T. J. EMERSON, J. O. PINTO, D. L. RIFE, and L. GREBE (2011). Radar climatology of the COPS region. *Quarterly Journal of the Royal Meteorological Society* **137**: ((S1)), 31–41. DOI: 10.1002/qj.747.
- WEUSTHOFF, T. (2011). *Weather Type Classification at MeteoSwiss - Introduction of new automatic classification schemes*. 235, 46pp.
- WEUSTHOFF, T. and T. HAUF (2008). The life cycle of convective-shower cells under post-frontal conditions. *Quarterly Journal of the Royal Meteorological Society* **134**: 841–857. DOI: 10.1002/qj.260.
- WHEELER, S. and G. S. WATSON (1964). A Distribution-Free Two-Sample Test on a Circle. *Biometrika* **51**: Publisher: [Oxford University Press, Biometrika Trust], 256–257. DOI: 10.2307/2334214.
- WHITEMAN, C. D. (1990). “Observations of Thermally Developed Wind Systems in Mountainous Terrain”. *Atmospheric Processes over Complex Terrain*. Edited by R. M. BANTA, G. BERRI, W. BLUMEN, D. J. CARRUTHERS, G. A. DALU, D. R. DURRAN, J. EGGER, J. R. GARRATT, S. R. HANNA, J. C. R. HUNT, R. N. MERONEY, W. MILLER, W. D. NEFF, M. NICOLINI, J. PAEGLE, R. A. PIELKE, R. B. SMITH, D. G. STRIMAITIS, T. VUKICEVIC, C. D. WHITEMAN, and W. BLUMEN. Meteorological Monographs. Boston, MA: American Meteorological Society, pages 5–

42. ISBN: 978-1-935704-25-6. DOI: 10.1007/978-1-935704-25-6\_2. URL: [https://doi.org/10.1007/978-1-935704-25-6\\_2](https://doi.org/10.1007/978-1-935704-25-6_2).

WILKS, D. S. (2006). *Statistical methods in the atmospheric sciences*. 2nd ed. International geophysics series v. 91. Amsterdam ; Boston: Academic Press. 627 pages. ISBN: 978-0-12-751966-1.

YANG, L., J. A. SMITH, M. L. BAECK, E. BOU-ZEID, S. M. JESSUP, F. TIAN, and H. HU (2014). Impact of Urbanization on Heavy Convective Precipitation under Strong Large-Scale Forcing: A Case Study over the Milwaukee–Lake Michigan Region. *Journal of Hydrometeorology* **15**: Publisher: American Meteorological Society Section: Journal of Hydrometeorology, 261–278. DOI: 10.1175/JHM-D-13-020.1.

## **Acknowledgements**

There are many people who helped me realise this master thesis to which I want to extend my gratitude. First of all, my thanks go to my supervisor Prof. Dr Olivia Romppainen-Martius, and my advisors Dr Yannick Barton and Dr Timothy Raupach, for supporting me in my research and providing many helpful discussions and remarks. Their help has substantially improved this thesis's quality, and without them, it would not have been possible. Further, I would like to acknowledge Dr Andrey Martinov for his support, especially with the running of the WRF model simulations and Pauline Rivoire for her help in all things concerning statistics.

I am very thankful for my family's support, which enabled me to pursue my masters degree, especially now during these extraordinary times due to the COVID-19 Pandemic. I would also like to thank Noah Mitchel for improving the quality of my writing and making this text more enjoyable to read.

Finally, I want to thank all the people who develop and share their software packages for R and Python with the scientific community. Their commitment to open-source software by providing their tools free of charge was key for making this thesis possible in its current form





## Declaration of consent

on the basis of Article 30 of the RSL Phil.-nat. 18

Name/First Name: Martin Pius Aregger

Registration Number: 15-125-701

Study program: M.Sc. in Climate Sciences

Bachelor ☐ Master ☒ Dissertation ☐

Title of the thesis: Stationary and slow-moving convection over Switzerland: A 14-year radar-based climatology

Supervisor: Prof. Dr. Olivia Romppainen-Martius

I declare herewith that this thesis is my own work and that I have not used any sources other than those stated. I have indicated the adoption of quotations as well as thoughts taken from other authors as such in the thesis. I am aware that the Senate pursuant to Article 36 paragraph 1 litera r of the University Act of 5 September, 1996 is authorized to revoke the title awarded on the basis of this thesis.

For the purposes of evaluation and verification of compliance with the declaration of originality and the regulations governing plagiarism, I hereby grant the University of Bern the right to process my personal data and to perform the acts of use this requires, in particular, to reproduce the written thesis and to store it permanently in a database, and to use said database, or to make said database available, to enable comparison with future theses submitted by others.

Messen, January 31, 2021

Place/Date



Signature